

APPLICATION OF DYNAMIC MONTE CARLO TECHNIQUE IN PROTON BEAM
RADIOTHERAPY USING GEANT4 SIMULATION TOOLKIT

A Dissertation

by

FADA GUAN

Submitted to the Office of Graduate Studies of
Texas A&M University
in partial fulfillment of the requirements for the degree of

DOCTOR OF PHILOSOPHY

May 2012

Major Subject: Nuclear Engineering

UMI Number: 3572366

All rights reserved

INFORMATION TO ALL USERS

The quality of this reproduction is dependent upon the quality of the copy submitted.

In the unlikely event that the author did not send a complete manuscript and there are missing pages, these will be noted. Also, if material had to be removed, a note will indicate the deletion.



UMI 3572366

Published by ProQuest LLC (2013). Copyright in the Dissertation held by the Author.

Microform Edition © ProQuest LLC.

All rights reserved. This work is protected against unauthorized copying under Title 17, United States Code



ProQuest LLC.
789 East Eisenhower Parkway
P.O. Box 1346
Ann Arbor, MI 48106 - 1346

Application of Dynamic Monte Carlo Technique in Proton Beam Radiotherapy Using

Geant4 Simulation Toolkit

Copyright 2012 Fada Guan

APPLICATION OF DYNAMIC MONTE CARLO TECHNIQUE IN PROTON BEAM
RADIOTHERAPY USING GEANT4 SIMULATION TOOLKIT

A Dissertation

by

FADA GUAN

Submitted to the Office of Graduate Studies of
Texas A&M University
in partial fulfillment of the requirements for the degree of

DOCTOR OF PHILOSOPHY

Approved by:

Chair of Committee,	John W. Poston, Sr.
Committee Members,	Leslie A. Braby
	John R. Ford, Jr.
	Nancy D. Turner
Head of Department,	Yassin A. Hassan

May 2012

Major Subject: Nuclear Engineering

ABSTRACT

Application of Dynamic Monte Carlo Technique in Proton Beam Radiotherapy Using

Geant4 Simulation Toolkit. (May 2012)

Fada Guan, B.E., Tsinghua University;

M.S., Texas A&M University

Chair of Advisory Committee: Dr. John W. Poston, Sr.

Monte Carlo method has been successfully applied in simulating the particles transport problems. Most of the Monte Carlo simulation tools are static and they can only be used to perform the static simulations for the problems with fixed physics and geometry settings. Proton therapy is a dynamic treatment technique in the clinical application. In this research, we developed a method to perform the dynamic Monte Carlo simulation of proton therapy using Geant4 simulation toolkit. A passive-scattering treatment nozzle equipped with a rotating range modulation wheel was modeled in this research.

One important application of the Monte Carlo simulation is to predict the spatial dose distribution in the target geometry. For simplification, a mathematical model of a human body is usually used as the target, but only the average dose over the whole organ or tissue can be obtained rather than the accurate spatial dose distribution. In this research, we developed a method using MATLAB to convert the medical images of a patient from CT scanning into the patient voxel geometry. Hence, if the patient voxel

geometry is used as the target in the Monte Carlo simulation, the accurate spatial dose distribution in the target can be obtained.

A data analysis tool—root was used to score the simulation results during a Geant4 simulation and to analyze the data and plot results after simulation.

Finally, we successfully obtained the accurate spatial dose distribution in part of a human body after treating a patient with prostate cancer using proton therapy.

DEDICATION

I dedicate this dissertation to my parents. Without their love, care, education, and encouragement, I would not have the goals to strive and would not be the best to realize my dreams.

ACKNOWLEDGEMENTS

I would like to express my sincere gratitude to my committee chair, Dr. John W. Poston, Sr. for his patient guidance in my study and research and enthusiastic help in my life. He is not only my academic advisor but also a mentor in spirit. I also would like to thank my committee members Dr. Leslie A. Braby, Dr. John Ford and Dr. Nancy Turner for their guidance, support and help throughout my study and research. I also thank Dr. Stephen Guetersloh for his proofreading and corrections for this dissertation.

I want to thank Dr. Warren Reece and Dr. Latha Vasudevan for teaching me nuclear instrumentation. I thank Dr. Sunil Chirayath for teaching me Monte Carlo method. I thank Dr. Gamal Akabani for teaching me medical physics and providing research facilities. I thank Dr. Salih Yurttas for teaching me C++ programming language. I thank Dr. Ursula Mueller-Harknett for teaching me statistics. I thank Dr. Jim Ji for teaching me medical image processing methods. Thanks go to faculty and staff in the Department of Nuclear Engineering at Texas A&M University.

I want to thank the author of the NEU code, Dr. Bernard Gottschalk, and all the developers in Geant4 collaboration. I want to thank Drs. Makoto Asai, Sebastien Incerti, Tatsumi Koi, Joseph Perl, and Dennis Wright for teaching Geant4 at Texas A&M University. I want to thank Drs. Guy Barrand and Rene Brun for answering a lot of questions in data analysis. I thank Dr. Harald Paganetti from Massachusetts General Hospital and the researchers from M.D. Anderson Cancer Center for generously providing parameters to our design. I thank my classmate and friend Dr. Guoqing Zhang

for his direction in configuring an IDE for Geant4. Without their cooperation and information, this research could not have been completed.

I thank my friends Shaoyong Feng, Jingjie Zhou and Phuc Ton for discussing the usage of Geant4 and medical image processing. Thanks also go to my officemates Ngoc Nguyen, Adam Redwine, Ruoming Bi, Jesse Johns and Brad Appel for discussing problems with me during my research. Special thanks go to the Lau family, Dr. Shao, Zeyun, Jinkai, Chaqing, Jun, Amy, Lei, Di, Qing, Yunhuang, Youting, Gary, Matt, Jordan and Cherise for their help in my life.

I thank the South Texas Chapter of the Health Physics Society for awarding me the 2010–2011 Student Education Grant to support my study and research.

I also want to thank all my teachers, classmates, colleagues and friends.

Finally, thanks go to my wife and my family members for their endless love.

NOMENCLATURE

1D	One-dimensional
2D	Two-dimensional
3D	Three-dimensional
4D	Three-dimensional and Time
ASCII	American Standard Code for Information Interchange
CATANA	Centro di AdroTerapia e Applicazioni Nucleari Avanzate, Italy
CLHEP	Class Library for High Energy Physics
CSDA	Continuous Slowing-Down Approximation
CT	Computed Tomography
CTV	Clinical Target Volume
EGS	Electron and Gamma Shower
EM	ElectroMagnetic
FLUKA	FLUctuating KAscades
GEANT4	GEometry ANd Tracking, version 4
GTV	Gross Tumor Volume
IDE	Integrated Development Environment
I/O	Input/Output
IMRT	Intensity-Modulated Radiation Therapy
LANL	Los Alamos National Laboratory
LET	Linear Energy Transfer

MCNP(X)	Monte Carlo N-Particles (eXtended)
MRI	Magnetic Resonance Imaging
NEU	Nozzle with Everything Upstream
NIST	National Institute of Standards and Technology, Gaithersburg, MD
NPS	Number of Primary Source Particles
PET	Positron Emission Tomography
PHITS	Particle and Heavy Ion Transport code System
PTV	Planning Target Volume
RBE	Relative Biological Effectiveness
RCT	Random Controlled Trial
RMS	Root Mean Square (Standard Deviation)
SOBP	Spread-Out Bragg Peak
SPECT	Single-Photon Emission Computed Tomography
SSD	Source Surface Distance
UI	User Interface

TABLE OF CONTENTS

	Page
ABSTRACT	iii
DEDICATION	v
ACKNOWLEDGEMENTS	vi
NOMENCLATURE	viii
TABLE OF CONTENTS.....	x
LIST OF FIGURES	xii
LIST OF TABLES.....	xviii
1. INTRODUCTION	1
1.1 Overview.....	1
1.2 Scope of This Dissertation	2
2. OVERVIEW OF PROTON BEAM RADIOTHERAPY.....	3
2.1 History of Proton Beam Radiotherapy	3
2.2 Principles.....	3
2.3 Proton Therapy Facility	9
2.4 Radiobiological Properties	11
2.5 Clinical Application.....	14
3. MATERIAL AND METHODS.....	21
3.1 NEU Codes Package.....	21
3.2 Monte Carlo Method	21
3.3 Geant4 Simulation Toolkit.....	23
3.4 Data Analysis Tool Root.....	40
3.5 DICOM Images	42
3.6 Method to Convert DICOM CT Slices into a Voxel Geometry.....	47

	Page
4. SETTINGS FOR SIMULATION	57
4.1 Verification of Pristine Bragg Peak and Projected Range	57
4.2 Geometry Settings of Nozzle and Dose Scoring Volume.....	61
4.3 Primary Proton Source Settings	77
4.4 Physics Settings.....	78
4.5 Data Analysis Using Root.....	80
5. SIMULATION RESULTS.....	83
5.1 Effect of Multiple Scattering of Protons.....	84
5.2 EM Physics and Hadronic Physics	85
5.3 Primary Source Distributions	86
5.4 Results for Geometry Case No. 1	91
5.5 Results for Geometry Case No. 2.....	95
5.6 Results for Geometry Case No. 3.....	106
5.7 Results for Geometry Case No. 4.....	111
5.8 Results for Geometry Case No. 5.....	116
5.9 Results for Geometry Case No. 5 from Two Irradiations.....	120
5.10 Results for Geometry Case No. 6 in Treating Prostate Cancer.....	125
6. SUMMARY AND EXTENSION OF CURRENT RESEARCH.....	132
6.1 Summary	132
6.2 Extension of Current Research.....	133
REFERENCES	134
APPENDIX A	138
APPENDIX B.....	141
APPENDIX C.....	143
APPENDIX D	144
VITA.....	150

LIST OF FIGURES

	Page
Figure 2-1. Depth-Dose Distribution of a Broad Proton Beam in Water	5
Figure 2-2. The Formation of a Spread-Out Bragg Peak.....	5
Figure 2-3. A Comparison of Depth-Dose Distributions between Photons and Protons.....	6
Figure 2-4. Mass Stopping Power of Protons in Water, Liquid.....	8
Figure 2-5. A Gantry System at Massachusetts General Hospital	10
Figure 2-6. RBE, LET and Relative Dose vs. Depth in Water	13
Figure 2-7. MRI Image of the Uveal Melanoma Showing in the Left Eye	16
Figure 2-8. Dose Distribution in the Axial (a), Sagittal (b) and Coronal (c) Planes	17
Figure 2-9. Comparison of Dose Distribution between IMRT and Proton Therapy.....	18
Figure 2-10. Total Dose Distribution for the Whole Treatment	19
Figure 2-11. Comparison of Dose Distribution between Proton Therapy and Photon Therapy for Medulloblastoma.....	19
Figure 3-1. CT Numbers vs. Relative Electron Density for All Tissue-Equivalent Inserts	46
Figure 3-2. Calibration Curve of CT Number and Material Density	47
Figure 3-3. CT Number Map of an Original CT Slice.....	54
Figure 3-4. Density Map and New Density Map of Original and Compressed CT Slices.....	55
Figure 3-5. Material ID Map and New Material ID Map of Original and Compressed CT Slices.....	56
Figure 3-6. A Patient Voxel Geometry.....	56

	Page
Figure 4-1. Percent Depth Dose Distribution from Broad Proton Beam.....	59
Figure 4-2. Passive-Scattering Nozzle and Water Phantom	64
Figure 4-3. S1 Component in Stair Style	65
Figure 4-4. The Symmetric Structure of S1	66
Figure 4-5. Multi-Track S1 and Propeller S1.....	67
Figure 4-6. S1 with Three Symmetric Sections	67
Figure 4-7. Gaussian Shaped Bi-Material Second Scatterer.....	70
Figure 4-8. The Relative Relation of Center Positions of S1 and S2	71
Figure 4-9. Patient-Specific Range Compensator	72
Figure 4-10. A Varian Multi-Leaf Collimator	73
Figure 4-11. Coronal View of CT, PET and PET-CT Fusion Images of the Patient.....	74
Figure 4-12. Axial View of CT Image of the Patient (slice 60/120).....	76
Figure 4-13. Saggital View of CT Image of the Patient (slice 257/512).....	76
Figure 4-14. Coronal View of CT Image of the Patient (slice 232/512).....	77
Figure 5-1. Comparison of Proton Trajectories with and without Multiple Scattering	85
Figure 5-2. Trajectories Produced from Ten Primary Protons Interacting with Water	86
Figure 5-3. The Distribution of the x-Coordinate of the Primary Proton Source.....	88
Figure 5-4. The Distribution of the y-Coordinate of the Primary Proton Source.....	88
Figure 5-5. The Distribution of the z-Coordinate of the Primary Proton Source.....	89

	Page
Figure 5-6. The Distribution of the Kinetic Energy of the Primary Proton Source.....	89
Figure 5-7. The Distribution of the Polar Angle of the Primary Proton Source.....	90
Figure 5-8. The Distribution of the Azimuthal Angle of the Primary Proton Source.....	90
Figure 5-9. Primary Proton Position Distribution on the Plane $z = -300$ cm.....	91
Figure 5-10. Geometry and Trajectories for Case No. 1	92
Figure 5-11. Energy Deposition along z-Axis on a Linear-Scale	93
Figure 5-12. Energy Deposition along z-Axis on a Log-Scale	93
Figure 5-13. Energy Deposition Distribution on the Plane $y = 0$ cm.....	94
Figure 5-14. Energy Deposition Distribution on the z-Plane with the Bragg Peak.....	94
Figure 5-15. Geometry and Trajectories for Case No. 2	95
Figure 5-16. Kinetic Energy Distribution of the Primary Protons on the Plane $z = -280.05$ cm.....	96
Figure 5-17. Kinetic Energy Distribution of the Primary Protons on the Plane $z = -230.05$ cm.....	97
Figure 5-18. Kinetic Energy Distribution of the Primary Protons on the Plane $z = -1.05$ cm.....	97
Figure 5-19. Polar Angle Distribution of the Primary Protons on the Plane $z = -280.05$ cm.....	98
Figure 5-20. Polar Angle Distribution of the Primary Protons on the Plane $z = -230.05$ cm.....	99
Figure 5-21. Polar Angle Distribution of the Primary Protons on the Plane $z = -1.05$ cm.....	99
Figure 5-22. Particle Current Distribution of the Primary Protons on the Plane $z = -280.05$ cm.....	100

	Page
Figure 5-23. Particle Current Distribution of the Primary Protons on the Plane $z = -230.05$ cm.....	101
Figure 5-24. Particle Current Distribution of the Primary Protons on the Plane $z = -1.05$ cm.....	101
Figure 5-25. Particle Current Distribution of the Primary Protons on the Plane $z = -1.05$ cm in Color Contour	102
Figure 5-26. Energy Deposition along the z-Axis.....	103
Figure 5-27. Depth Energy Deposition Distribution with Error Bar.....	104
Figure 5-28. x-y Planar Energy Deposition Distribution, All z	104
Figure 5-29. z-x Planar Energy Deposition Distribution, All y	105
Figure 5-30. x-y Planar Energy Deposition Distribution, $z:31.2\sim31.6$ cm.....	105
Figure 5-31. z-x Planar Energy Deposition Distribution, $y = 0$ cm	106
Figure 5-32. Particle Current Distribution of the Primary Protons on the Plane $z = -1.05$ cm.....	107
Figure 5-33. Polar Angle Distribution of the Primary Protons on the Plane $z = -1.05$ cm.....	108
Figure 5-34. Kinetic Energy Distribution of the Primary Protons on the Plane $z = -1.05$ cm.....	108
Figure 5-35. x-y Planar Energy Deposition Distribution, All z	109
Figure 5-36. z-x Planar Energy Deposition Distribution, All y	109
Figure 5-37. z-x Planar Energy Deposition Distribution, $y = 0$ cm	110
Figure 5-38. x-y Planar Energy Deposition Distribution, $z:26.4\sim26.8$ cm.....	110
Figure 5-39. SOBP Curve along the z-Axis on a Linear-Scale.....	112
Figure 5-40. SOBP Curve along the z-Axis on a Log-Scale	113
Figure 5-41. z-x Planar Energy Deposition Distribution, All y	113

	Page
Figure 5-42. x-y Planar Energy Deposition Distribution, All z	114
Figure 5-43. z-x Planar Energy Deposition Distribution on the Plane $y = 0$ cm ...	114
Figure 5-44. x-y Planar Energy Deposition Distribution on the Plane with Bragg Peak	115
Figure 5-45. x-y Planar Energy Deposition Distribution, z: 19.6~20.4 cm.....	115
Figure 5-46. Geometry and Trajectories in Case No. 5	117
Figure 5-47. z-x Planar Energy Deposition Distribution, All y	118
Figure 5-48. x-y Planar Energy Deposition Distribution, All z	118
Figure 5-49. Energy Deposition Distribution on the Plane $y = 0$ cm	119
Figure 5-50. Energy Deposition Distribution on the Plane with the Bragg Peak.....	119
Figure 5-51. Nozzle with a 180-Degree Rotation Angle around the Water Phantom.....	120
Figure 5-52. Energy Deposition Distribution along the z-Axis, All x and All y ...	122
Figure 5-53. z-x Planar Energy Deposition Distribution, All y	122
Figure 5-54. x-y Planar Energy Deposition Distribution, All z	123
Figure 5-55. Energy Deposition Distribution on the Plane $y = 0$ cm	123
Figure 5-56. Energy Deposition Distribution on the Plane with the Bragg Peak.....	124
Figure 5-57. 3D Energy Deposition Distribution Plotted Using SimpleGeo.....	124
Figure 5-58. Cut-View of 3D Energy Deposition Distribution Plotted Using Root.....	125
Figure 5-59. The Voxel Geometry of the Patient with Prostate Cancer	126
Figure 5-60. 3D Reconstruction of the Patient Geometry	127
Figure 5-61. The Bone Structure of the Patient	127

	Page
Figure 5-62. Plate Shifter, Wedge Shifter and the Patient Voxel Geometry	128
Figure 5-63. Isodose Lines Superimposed on Axial CT Image	129
Figure 5-64. Isodose Lines Superimposed on Sagittal CT Image	130
Figure 5-65. Isodose Lines Superimposed on Coronal CT Image	130
Figure 5-66. 3D Absolute Dose Distribution in Patient Voxel Geometry.....	131

LIST OF TABLES

	Page
Table 3-1. Material Density and Material ID.....	51
Table 3-2. New Material Density and New Material ID	52
Table 4-1. The Bragg Peak Positions and Ranges in Water Phantom	60
Table 4-2. Composition of Materials and CSDA Ranges of 250 MeV Protons.....	62
Table 4-3. Parameters of S1 from NEU.....	65
Table 4-4. Parameters of S2 from NEU.....	70
Table 5-1. Component Settings for Different Simulation Cases.....	84
Table C-1. Parameters of S1 from NEU for Case No. 6	143
Table C-2. Parameters of S2 from NEU for Case No. 6	143

1. INTRODUCTION

1.1 Overview

Radiotherapy is one of the three main cancer therapy methods including surgery, chemotherapy and radiotherapy (Bayle and Levin 2008). The basic principle of radiotherapy is to utilize the interaction of ionizing radiation (internal or/and external) with matter to deposit energy in the target region, i.e., a tumor to kill the cancer cells. In this dissertation, we will focus on one emerging cancer treatment method—proton beam radiotherapy. In our previous research, we designed a passive-scattering treatment head and simulated the tracking processes of protons in matter using a Monte Carlo code MCNPX and calculated the spatial dose distributions in a water phantom with several different nozzle settings. Our previous research results have been published (Guan et al. 2011). However, the simulation cannot reveal the essence of the reality because our simulation was static but the real clinical proton therapy process is dynamic. Besides, no accurate dose distributions in a human body were obtained in our previous research. In current research, we completed the tasks left previously. At first, we adopted a dynamic Monte Carlo simulation toolkit Geant4 to simulate the real dynamic process in proton therapy. In addition, we also developed a method to convert the medical images of a patient from the CT scanning to the target geometry of the therapeutic proton beam in Geant4 Monte Carlo simulation, and the accurate spatial dose distribution in the patient body were obtained.

This dissertation follows the style of *Health Physics*.

1.2 Scope of This Dissertation

In this dissertation we will summarize our current research, describe our methods and provide our simulation results.

Section 2 will provide an overview of proton beam therapy, including the history, basic principles, facilities, radiation biology features of protons and clinical applications.

Section 3 will introduce the design and simulation codes and data analysis tools used in this research.

Section 4 will provide the settings for simulation in the current research.

Section 5 will provide the detailed Monte Carlo simulation results. The geometry, particle trajectories, and simulation results will be shown graphically.

Section 6 will summarize this research and discuss the extension of current research.

2. OVERVIEW OF PROTON BEAM RADIOTHERAPY

2.1 History of Proton Beam Radiotherapy

In 1946, Robert R. Wilson (Wilson 1946) first proposed the use of protons for radiation therapy at the Harvard Cyclotron Laboratory. In 1954, the first patient was treated at Lawrence Berkeley Laboratory. By December, 2007, thirty-three proton therapy centers had been established worldwide, and twenty-six of them are still active. Seven future proton therapy facilities are currently under construction or are fully funded. From 1954 to 2007, 53,439 patients had received proton therapy (ICRU 2007).

2.2 Principles

2.2.1 Physical Rationale

A proton is a charged particle. Due to its ionizing ability, a proton can impart energy to the matter it passes through. From the view of radiation biology, this imparted energy can damage the DNA of the biological cells. The lethal DNA lesions can be base and sugar modifications, single-strand breaks, and double-strand breaks, etc. (Shukla and Leszczynski 2008).

Why can a proton beam be chosen as a therapeutic beam for the treatment of cancer? The main reason is protons have a well-defined penetration range. Before protons come to rest, the proton beam can lose maximum energy in a short distance along its path. In the depth-dose curve of a monoenergetic proton beam, a very sharp dose peak occurs before the beam reaches its penetration range, shown in Figure 2-1 (Paganetti and Bortfeld 2005). This dose peak is called Bragg peak, which was

discovered by a British scientist William Henry Bragg in 1903. The dose peak occurs because the proton interaction cross section with matter increases as energy decreases. The locations of dose peaks are different for proton beams with different energies. One monoenergetic proton beam is not sufficient to treat the tumor with a large volume because the single Bragg peak is not wide enough to cover the whole tumor volume. In the clinical applications, proton beam modulation techniques are adopted to modify the proton beam characteristics (energy and spatial distributions) to make the proton beam deliver a flat high-dose region called the spread-out Bragg peak (SOBP) in the target tumor volume. One commonly-used method to form an SOBP dose curve is to insert a range modulation wheel composed of several steps with different material thicknesses in the beam line (Chu et al. 1993). During the treatment, the wheel spins around its central axis at a constant speed and the initial proton beam passes through each step sequentially. Each step plays the role of a stopper in lowering the beam energy to form a new dose curve corresponding to the thickness and relative width of the step. The sum of all the single dose curves is the SOBP dose curve. An SOBP curve and all the constituted single dose curves are shown in Figure 2-2 (ICRU 2007).

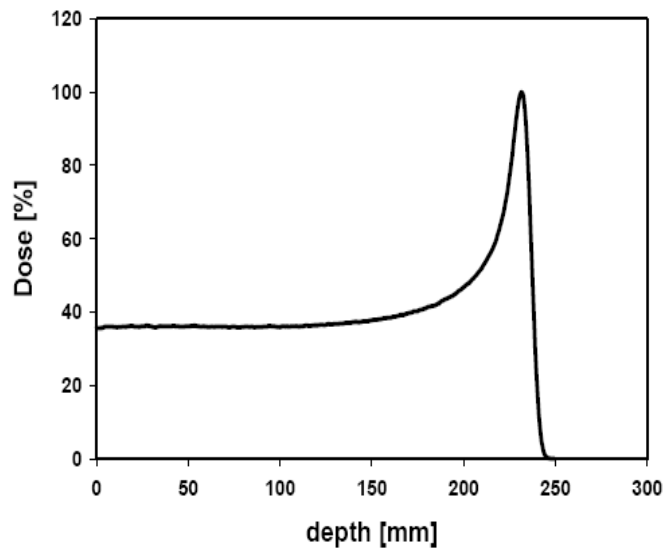


Figure 2-1. Depth-Dose Distribution of a Broad Proton Beam in Water (Paganetti and Bortfeld 2005)

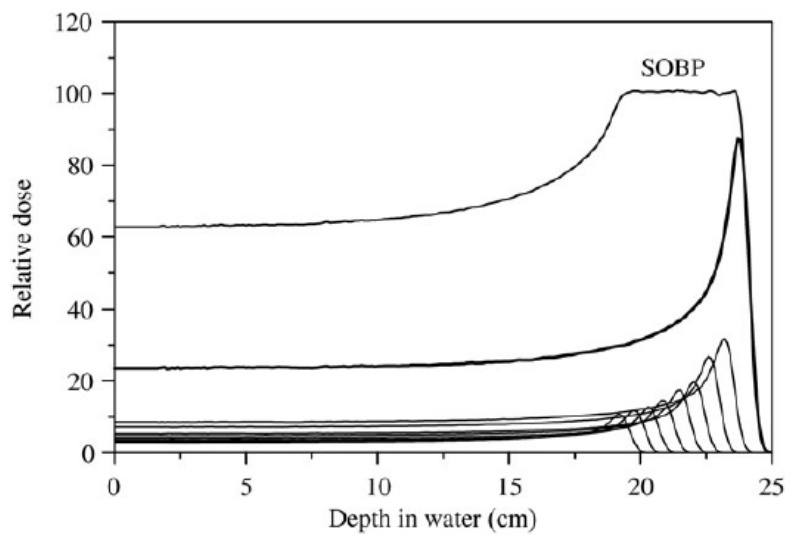


Figure 2-2. The Formation of a Spread-Out Bragg Peak (ICRU 2007)

2.2.2 Clinical Rationale

The feasibility of delivering a higher uniform dose to the tumor makes proton therapy of interest because of an increased tumor control probability (Paganetti and Bortfeld 2005). The physician can choose the energy and intensity of proton beam according to the position and profile of the tumor. Compared with traditional photon therapy, proton therapy has many advantages, e.g., good high-dose conformity to tumor and lower dose to healthy tissue, lower tumor reoccurrence rate, and fewer adverse side effects (Olsen et al. 2007). Proton therapy is a preferred treatment method for pediatric cancers because it will not influence the growth of the young patients. A comparison of dose distributions between photons and protons is shown in Figure 2-3 (Weber 2006).

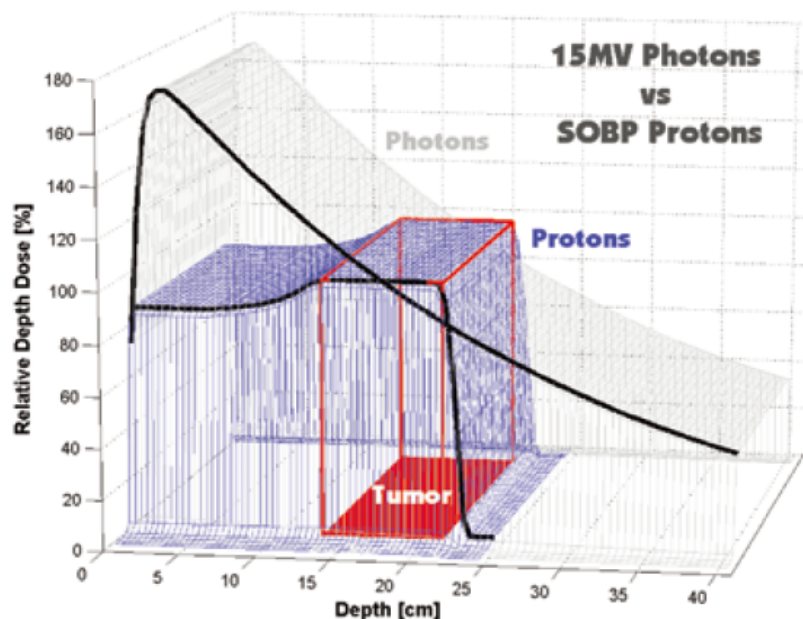


Figure 2-3. A Comparison of Depth-Dose Distributions between Photons and Protons (Weber 2006)

2.2.3 Interactions of Protons with Matter

When protons pass through matter, they will slow down by interacting with the matter by electromagnetic interactions and nuclear interactions (Paganetti and Bortfeld 2005). Protons lose their energy primarily by electromagnetic interactions with atomic electrons. The mass stopping power of protons in water (Berger et al. 2005) is shown in Figure 2-4. The electronic stopping power is due to the interactions with atomic electrons resulting in ionization or excitation. The nuclear stopping power is due to elastic Coulomb interactions in which recoil energy is imparted to atoms. The term “nuclear” stopping power is misleading because it does not pertain to nuclear interactions (ICRU 2011). Here both electronic and nuclear stopping powers are in the category of electromagnetic interactions. High-energy secondary gammas or delta rays (secondary electrons that have enough energy to leave their production sites and form their own trajectories) can be produced from electromagnetic interactions.

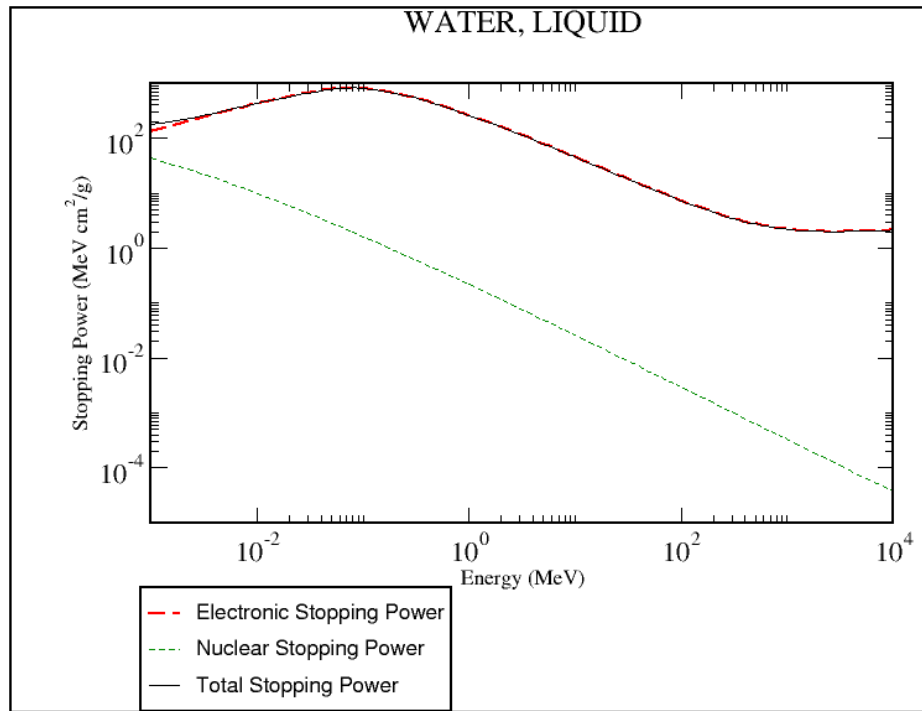


Figure 2-4. Mass Stopping Power of Protons in Water, Liquid (Berger et al. 2005)

Nuclear interactions become more important as proton energy increases. Though the proportion of nuclear interactions is smaller than electromagnetic interactions in the therapeutic energy range, they cannot be neglected because of the production of secondary neutrons. From the view of radiation biology, secondary neutrons are important because they have higher RBE (relative biological effectiveness) values (ICRP 2003). From the view of radiation shielding, neutrons are important because they have higher radiation weighting factors (ICRP 2003). Besides secondary neutrons, some charged particle fragments can also be produced from nuclear interactions of protons

with matter. For example, if an O-16 nucleus is hit by a proton, the possible products can include an O-15 nucleus, a neutron and some gammas. Secondary neutrons can interact with matter and produce their own secondary particles, i.e., heavy charged particles like protons, carbon ions, nitrogen ions and oxygen ions (depending on the atomic composition of the medium). These secondary charged particles usually have low energy and cannot form their own trajectories in matter, so their energy deposition events can be treated to occur locally at their production sites. The secondary neutrons and gammas can penetrate the treatment facility and the patient's body, so shielding is necessary for proton therapy. Shielding can be used to reduce the effect of neutrons produced in the treatment facility, but nothing can be done to avoid the production of neutrons in the patient's body (Paganetti and Bortfeld 2005).

To make the simulation process as close as to the real treatment, both electromagnetic and nuclear interactions should be considered. The physics settings in the simulation will be discussed in section 4.4.

2.3 Proton Therapy Facility

A typical proton-therapy facility includes three main components: an accelerator with an energy selection system, a beam transport system, and a beam delivery system.

At present, only cyclotrons and synchrotrons are used in dedicated hospital-based, proton-therapy facilities. The typical energy of the treatment proton beam ranges from 70 MeV (some are 60 MeV) to 230 MeV (in some facilities, the maximum energy can be 270 MeV), corresponding to treating superficial tumors (ocular tumors) and tumors deep in the human body (ICRU 2007). The acceptable dose rate is about 2 Gy min^{-1} .

A beam delivery system can comprise several subsystems and may include some or all of the following: a gantry, a beam delivery nozzle (equipped with a snout), a volume-tracking and beam-gating device, and a patient-positioning and immobilization system. The beam delivery system is enclosed in a treatment room to be separated from the accelerator and beam line (ICRU 2007).

The beam delivery systems are categorized into two types: a gantry system or a stationary beam delivery system. A fixed horizontal beam (stationary beam) can only be used to treat patients in a seated or near-seated position, e.g., a patient with an ocular tumor. A gantry, shown in Figure 2-5 (Paganetti and Bortfeld 2005), equipped with a treatment head can rotate around the patient lying on a movable table. The nozzle delivers the beam to the patient at the desired angle.



Figure 2-5. A Gantry System at Massachusetts General Hospital (Paganetti and Bortfeld 2005)

To spread out the beam laterally, the beam-delivery techniques are categorized into two types: active (dynamic) scanning and passive scattering (ICRU 2007). The dynamic scanning technique is a time-dependent method to deliver the desired dose to the target tumor in a scanning mode, in which, the direction of pencil beam is controlled by magnets, and the beam scans the tumor from one site to next site and from one layer to the next layer. In a passive-scattering nozzle, a narrow beam is scattered by a scattering system to form a broad beam laterally; then the broad beam is confined by collimators into a profile identical to the lateral profile of the tumor and compensated by a patient-specific compensator to the longitudinal profile of the tumor. The dynamic scanning technique provides a more precise dose delivery, while passive scattering technique is still used more widely. The scanning technique is gradually becoming routine.

2.4 Radiobiological Properties

2.4.1 Linear Energy Transfer

The variation of the shape of the depth-dose distribution curve is due to the change of linear energy transfer (LET) of the proton beam along the path. The LET values of protons at a fixed energy can be simply derived from the mass stopping power of protons in a certain material. The dose-averaged LET is usually used in calculating the depth-LET distribution. Chu provided a definition of it (Chu 2006). Our modified definition of dose-averaged LET (in keV μm^{-1}) at a depth z in a medium is:

$$L_D(z) = \int LD(L,z)dL / \int D(L,z)dL, \quad (1)$$

where z (in cm) is depth in medium, L (in keV μm^{-1}) is LET and $D(L, z)$ (in Gy) is the dose contributed by particles of a given L at the depth of z . The dose is calculated by:

$$D(L, z) = 1.6 \times 10^{-9} \phi(L, z) L / \rho, \quad (2)$$

where $\phi(L, z)$ (in particles cm^{-2}) is the fluence of particles with a given L at the depth of z , and ρ (in g cm^{-3}) is the material density.

2.4.2 Relative Biological Effectiveness

The RBE of protons is defined as the ratio of the absorbed dose from the reference radiation (photons) and the absorbed dose from protons producing the same biological effect. There are no proton RBE values based on human tissue response data, and there are no experimental data from *in vivo* systems supporting the specific RBE. Clinically, a generic RBE value of 1.1 is applied to all tissues in the direct proton beam path (ICRU 2007). RBE-weighted absorbed dose is recommended in ICRU Report No. 78 (ICRU 2007), which is used for a clinical proton beam to replace the term equivalent dose. The unit Gy (RBE) is used to replace the old units Gy(E), GyE and CGE (cobalt gray equivalent). If 1.1 is used as the generic RBE value, the RBE-weighted absorbed dose for clinical protons is:

$$D_{RBE} = 1.1 \times D, \quad (3)$$

where D represents the physical absorbed dose in units of Gy. The unit for RBE-weighted absorbed dose is Gy (RBE).

Generally, the RBE value increases as the LET increases (Paganetti and Bortfeld 2005). One example of RBE and dose-averaged LET along the beam path in water is

shown in Figure 2-6 (Wouters et al. 1996). The incident beam energy is 70 MeV. The SOBP extends from the depth of 8 mm to 30 mm in water.

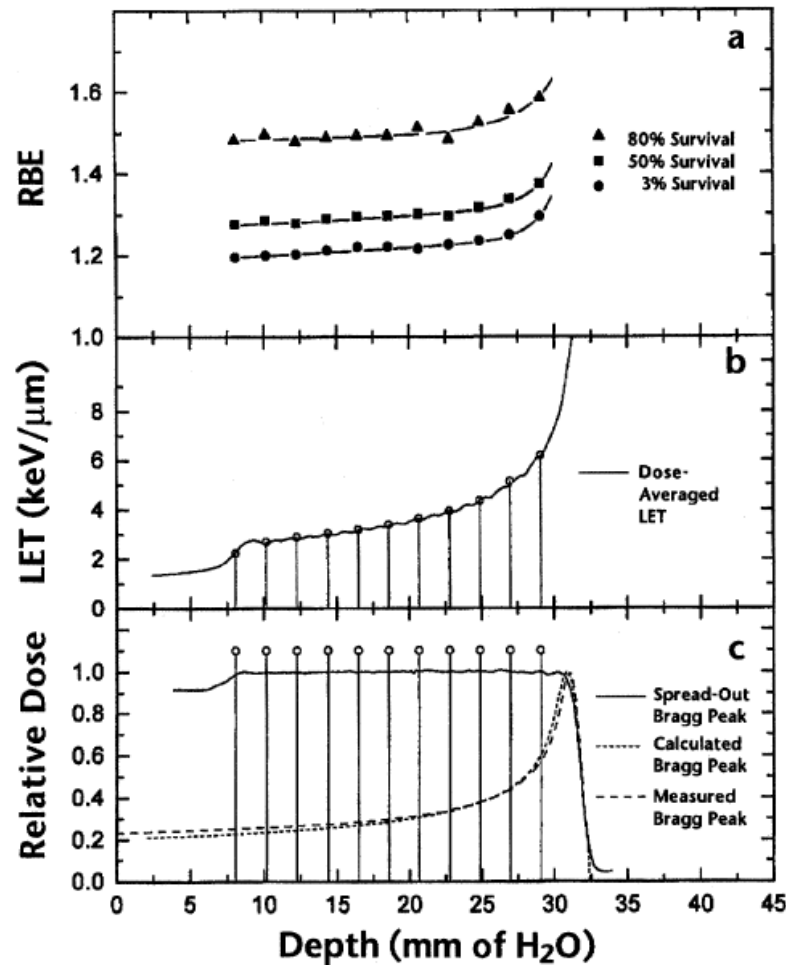


Figure 2-6. RBE, LET and Relative Dose vs. Depth in Water

2.5 Clinical Application

2.5.1 Cancer Types

Not all cancer types are suitable to be treated by proton therapy. Only solid tumors with defined borders can obtain benefits from proton therapy. Proton therapy has been applied in several different types of tumors, such as central nervous system (CNS) tumors, prostate cancer, ocular tumors, lung cancer, and liver cancer. In addition, proton therapy also shows its advantages in the treatment of pediatric tumors (Olsen et al. 2007).

2.5.2 Side Effects

During the treatment of proton therapy, the patients do not feel any pain or discomfort. Even after the treatment, rare side effects can occur. One advantage of proton therapy is that it produces fewer side effects than conventional photon therapy. The probable early side effects include skin reaction, fatigue and temporary hair loss, all of which will disappear in several weeks. The side effects strongly depend on the location of the treated tumor. For example, for children CNS tumors, the early side effects also include erythema and headache (Noel et al. 2003). Occurrence of late side effects is very rare for proton therapy.

2.5.3 Ocular Tumors

Proton therapy has emerged as an alternative to enucleation or ocular brachytherapy in the treatment of ocular tumors (Olsen et al. 2007). Olsen et al. summarized 32 publications that addressed clinical outcomes after proton therapy for patients with ocular tumors. In a random controlled trial (RCT) including 186 patients with choroidal or ciliary body melanoma, the clinical dose was reduced from 70 to 50

CGE (replaced by Gy (RBE)). For the study of uveal melanoma, the five-year overall survival was 81% in the proton therapy group while it is 68% in the enucleation group. For patients with choroidal melanoma, proton therapy produced a higher mortality rate than brachytherapy.

One clinical case of uveal melanoma is shown in Figure 2-7, in which, the left image is an MRI image showing the tumor in the left eye; the right image contains the tumor volume profiles and isodose contours. Gross tumor volume (GTV), clinical target volume (CTV) and planning target volume (PTV) are indicated by red lines. The definitions of these three concepts can be found in ICRU Report No. 78 (ICRU 2007). The GTV is the gross palpable, visible, or clinically demonstrable location and extent of the malignant growth (ICRU 2007). The CTV is a tissue volume that contains the GTV(s) and/or sub-clinical malignant disease at a certain probability level. This volume has to be treated adequately (ICRU 2007). Like the GTV, the CTV is a clinical-anatomical concept. The PTV is a geometrical concept, introduced for treatment planning. It surrounds the CTV with additional margins to compensate for different variations and uncertainties of beams relative to the CTV (ICRU 2007).

The beam energy is 70 MeV with an SOBP width of 2 cm. The prescribed dose at Mid-SOBP is 70 Gy (RBE). The fractionation strategy is five fractions over seven days.

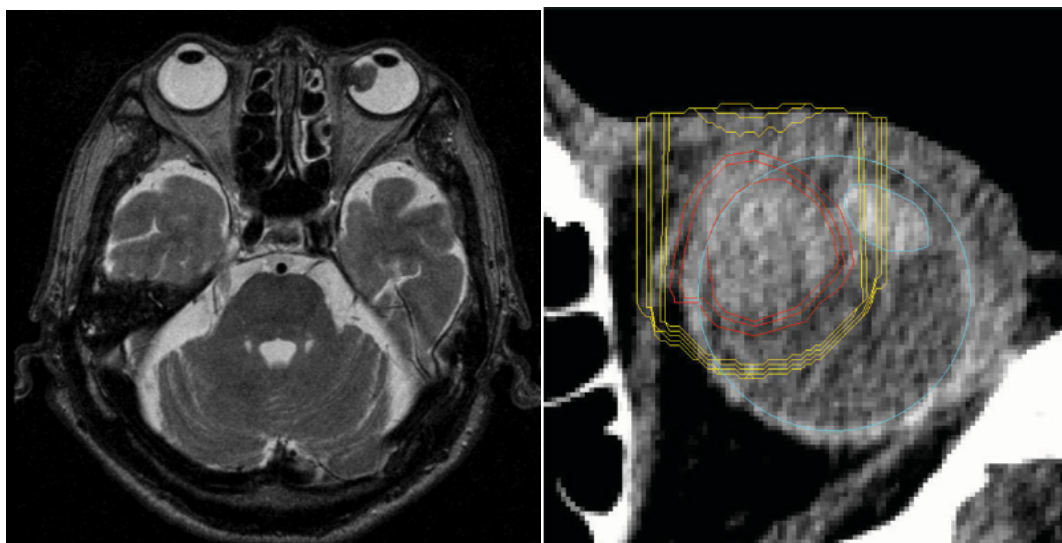


Figure 2-7. MRI Image of the Uveal Melanoma Showing in the Left Eye. The GTV, CTV and PTV are indicated by red lines. The yellow lines from outside to inside stands for 10%, 30%, 50%, 90% and 95% of the prescribed dose 70 Gy (RBE).

2.5.4 Prostate Cancer

In North America, prostate cancer is the most common cancer for men (especially for men older than 50 years old), and the mortality is second to lung cancer in men (Bayle and Levin 2008). The specific causes of prostate cancer are still unknown (Hsing and Chokkalingam 2006). The most common method for diagnosing the prostate cancer is prostate-specific antigen (PSA) screening. Besides, imaging technique is also used to aid the diagnostics of prostate cancer (Schoder and Larson 2004).

The conventional radiotherapy for prostate cancer at doses associated with acceptable adverse effects may not provide sufficient cancer control (Olsen et al. 2007). Proton therapy may offer an option both for dose escalation and for better confinement of the treatment. One clinical case of adenocarcinoma of prostate (ICRU 2007) is shown

in Figure 2-8. The energy of incident beam is 250 MeV. The fractionation strategy is 35 fractions over seven weeks. 98% of the CTV can obtain a dose of higher than 74 Gy from the whole treatment.

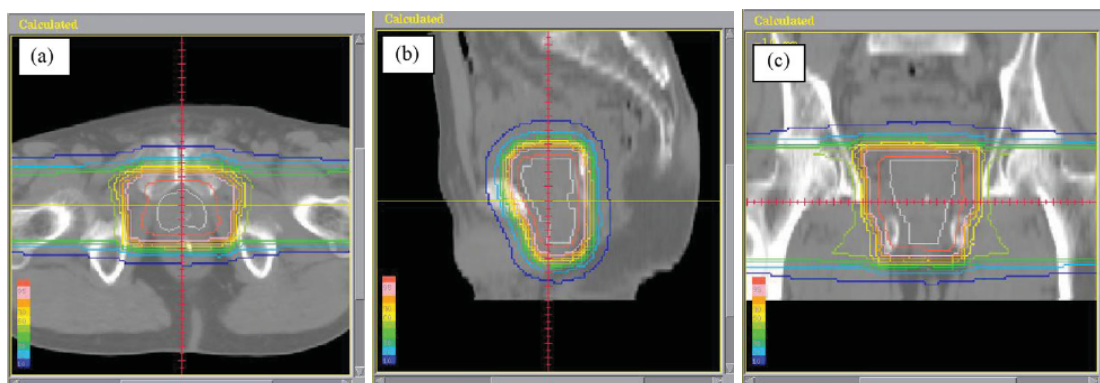


Figure 2-8. Dose Distribution in the Axial (a), Sagittal (b) and Coronal (c) Planes. The white line encompasses the CTV. The red contour represents 95% of the prescribed dose, and that in blue represents 1% of the prescribed dose. The remaining contours represent the 10–80% isodoses in 10 percent steps.

At present, IMRT (Intensity-Modulated Radiation Therapy) is the most widely used form of external radiation for prostate cancer in the US (Coen and Zietman 2009). Considering the cost in treatment, IMRT is more cost-effective than proton therapy. One example of IMRT and passive-scattering proton therapy is shown in Figure 2-9. The IMRT high-dose region is more conformal to the target tumor, but proton therapy will influence fewer healthy tissues than IMRT. Hence, proton therapy can result in a lower radiation risk to the patient.

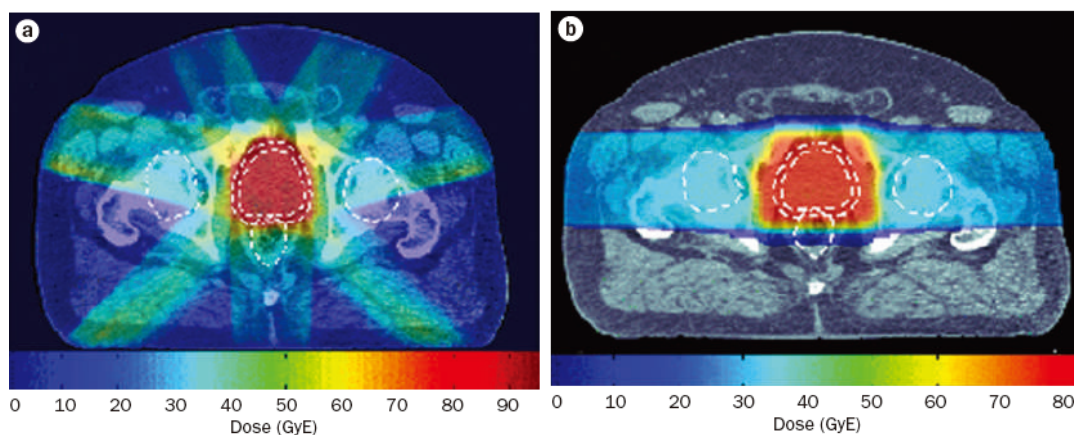


Figure 2-9. Comparison of Dose Distribution between IMRT and Proton Therapy

2.5.5 Pediatric Tumors

With a reduction of the integral dose, proton therapy is much more beneficial to the pediatric patients (Paganetti and Bortfeld 2005). One clinical example shown here is medulloblastoma (Paganetti and Bortfeld 2005; ICRU 2007), which is a kind of malignant pediatric brain tumor. The treatment strategy should consider delivering dose to the whole CNS. Hence, the treatment is divided into two segments; one to the whole CNS, including whole brain and spine, and the other only to the tumor. The energy of the incident beam is 230 MeV. The total effect for the whole treatment is shown in Figure 2-10. The total dose to posterior fossa is 54.0 Gy (RBE) in 30 fractions in 6 weeks.

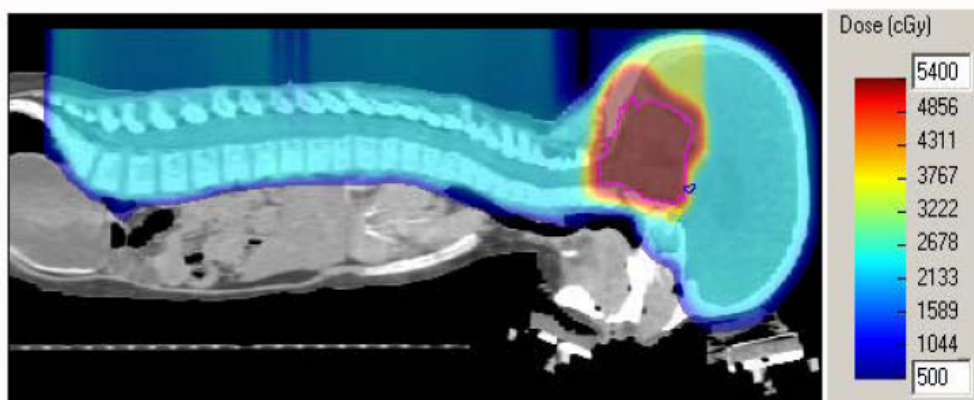


Figure 2-10. Total Dose Distribution for the Whole Treatment

A comparison of dose distribution between proton therapy and photon therapy is shown in Figure 2-11 (Kirsch and Tarbell 2004). The cochlea is located in the high-dose region in photon therapy, which can result in deafness in 50% of the patients in this age group (ICRU 2007).

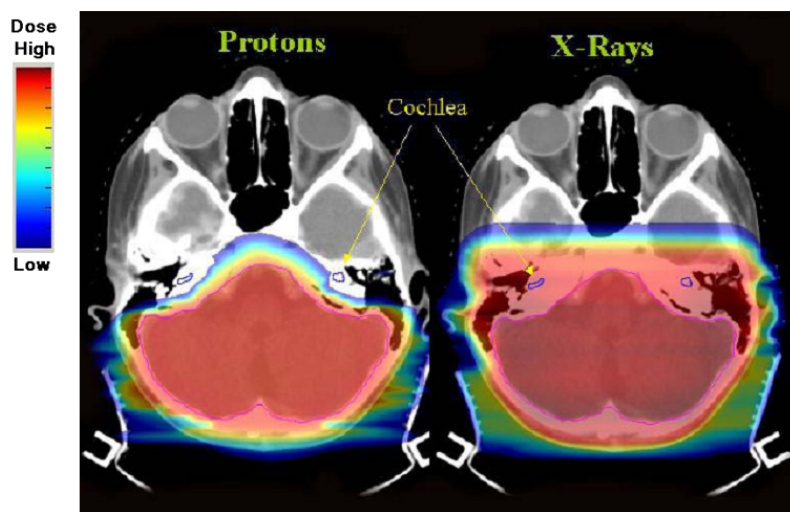


Figure 2-11. Comparison of Dose Distribution between Proton Therapy and Photon Therapy for Medulloblastoma

2.5.6 Summary of Clinical Application of Proton Therapy

Lodge et al. analyzed the comparison of treatment results between photon and proton therapies. Their results show that for ocular tumor and skull-base tumors, proton therapy is superior; for CNS and prostate tumors, the effects are similar; and for other tumors, there are no firm conclusions (Lodge et al. 2007).

3. MATERIAL AND METHODS

In this Section, we will briefly introduce the design and simulation tools for a passive-scattering treatment nozzle in proton therapy. We will give a detailed description of the performance of a dynamic Monte Carlo simulation. We will also provide a method to convert the medical image sequence from CT scanning into the patient voxel geometry used for the Monte Carlo simulation.

3.1 NEU Codes Package

The NEU codes package is a specialized toolkit including several subroutines for designing the double-scattering system in a passive-scattering nozzle. NEU means “Nozzle with Everything Upstream.” NEU was written by Bernard Gottschalk in FORTRAN (FORmula TRANslator) language in the late 1980s (Gottschalk 2006).

In our previous research, we have successfully applied NEU codes package in designing the double-scattering system to meet different therapeutic requirements. We will not repeat introducing the usage of NEU in this dissertation. More details can be found in our previous research (Guan 2009). The parameters of several different scattering systems used in this research were still calculated using the NEU codes package.

3.2 Monte Carlo Method

The Monte Carlo method was first used in the 1940s by physicists working on nuclear weapon projects at the Los Alamos National Laboratory (LANL). It is a random sampling computational algorithm (Kalos and Whitelock 2008). The application of this

algorithm is not limited by the dimensions of problems. In one Monte Carlo application, the histories of a large number of individual events are tracked and some aspects are recorded according to their individual or average behavior. The Monte Carlo method has been applied in many fields, such as high-energy physics, radiation detection, space radiation, medical physics, health physics, and economics. With the computerization spreading, lots of Monte Carlo codes have been developed. In the particle transport field, the popular Monte Carlo codes include MCNP(X), EGS, Geant4, Fluka, and PHITS.

Monte Carlo dose calculations are known to be more accurate in dosimetry than commercial treatment planning systems that are based on fast but approximating semi-empirical algorithms (Mohan and Nahum 1997). Except for EGS, any of the other Monte Carlo codes mentioned above can be used to simulate the transport of protons.

We used MCNPX as a simulation tool in our previous research and the design method to obtain SOBP dose distribution has been published (Guan et al. 2011). In our previous research we combined a series of static results into one equivalent result assuming it is produced from the real dynamic behavior. However, that method was not a real dynamic method, and it does not reveal the essence of the dynamic problem. In this research, we used Geant4 as our simulation tool. In one Geant4 application, the position of geometry in space or other geometry properties, such as material or size can be changed during the simulation. So, Geant4 can be used to perform a real dynamic simulation in which the condition is close to the condition in reality.

3.3 Geant4 Simulation Toolkit

Geant4 is a toolkit for the simulation of the passage of particles through matter (Agostinelli et al. 2003). Geant4 stands for GEometry ANd Tracking with main version number 4 (Carrier et al. 2004). The first stable version was released to the public in 1998. Up to the completion of current research, the latest stable version was Geant4.9.5 released on December 2, 2011, which was used in current research.

Geant4 is an achievement of a worldwide collaboration. Several different international organizations have been working on the development, maintenance and distribution of the code. The main contributing organizations include CERN (European Organization for Nuclear Research), KEK (High Energy Accelerator Research Organization, Japan), IN2P3 (Institut National de Physique Nucléaire et Physique des Particules, France) and SLAC (SLAC National Lab, USA). This software is written in object-oriented C++ programming language and it is free to download, use and distribute. Due to the open-source attribute of this software, the users can provide feedback to the developers on the official user forum, which is beneficial to the development and update of the code. The bugs of the source codes can be reported via the official bug reporting system. We also provided several suggestions and corrections to the source codes and examples of Geant4 during our research.

The use of Geant4 is completely different from the use of MCNP(X). In an MCNP(X) simulation, the user provides an input deck containing different parameter cards to specify the geometry, particle source, physics, and tally. In execution, MCNP(X) reads in the input file. After the execution, the simulation results will be stored in output

files. Geant4 is a toolkit, but not a concrete application, so it cannot be executed directly like invoking MCNP(X). Before using Geant4 to perform a simulation, the user must install it from source codes to construct a Geant4 development environment. The installation process is a compiling process. A C++ compiler is used to compile the source codes to produce different module libraries which can be invoked in the user's application later. Before the release of Geant4.9.5, the user was required to install CLHEP (Class Library for High Energy Physics) package and set corresponding environmental variables before installing Geant4. In Geant4.9.5, CLHEP has been integrated into Geant4 and the user does not need to install it any longer. Only after successful compilation of the source codes and setting of the environmental variables can the users begin to build one Geant4 project. Please note that there is not a concrete executable file for Geant4 like MCNP(X) for users to invoke. What the users should do is to create one Geant4 simulation project and edit some necessary C++ source codes including Geant4-defined and/or user-defined classes, and compile the source codes to produce an application, viz., an executable file which can be invoked to begin the simulation process.

One of the advantages in the Geant4 simulation is its application is very flexible. The users can easily modify the source codes for one application to fulfill their specific requirements. In addition, the users can modify the source codes of Geant4 and recompile them to update the Geant4 libraries. Utilizing this flexibility in programming, the users can develop a lot of applications with different features and functions. For example, the "time" concept can be introduced into one Geant4 application. The

principle is to convert the successive simulation events or running series into a continuing time series, viz., assign a “time” attribute to each simulation event or run. This method is called dynamic or a 4D (time with three-dimensional space coordinates) Monte Carlo technique (Paganetti 2004).

Another advantage is that a lot of available external application interfaces (not only for Geant4) can be invoked in a Geant4 simulation to extend the code capability. For example, some data analysis packages can be invoked in a Geant4 application to help store the simulation results in some histograms. The data analysis package can also help pop up a canvas to show the real-time simulation results during the running process of an application.

However, although Geant4 is free to use and some easy and complex examples are provided with the release of Geant4, the number of users is still very limited. One important reason is that the users have to write very complex and long C++ codes even for a very simple application. Another reason is Geant4 is not easy to learn and master in a short time for beginners. The users should be familiar with C++ programming and have sufficient knowledge in particle physics. If the users are not familiar with C++ programming, it will be very difficult for them to understand the meaning of the source codes. If the physics processes are not chosen correctly, the tracking process will be incorrect, which can result in the wrong simulation results.

Another problem in Geant4 simulation is it does not provide the simulation results output by default. If the user does not provide related methods in the source codes to allow the application to produce required information, there will not be any output

files containing simulation results stored on disk after simulation. However, this setting without default output information is also an advantage because it provides flexibility for the users. For example, the users can select any important information to output, such as primary particle information, tracking steps, energy deposition and particle current. The user can also print out the data in a desired format either in binary or in ASCII (American Standard Code for Information Interchange). The data alignment can also be specified by the users.

Geant4 can be compiled and run on different platforms, such as Linux, Mac, and Windows (a compiling environment is needed). We chose a Linux operating system (Ubuntu10.10) as our simulation platform because more Geant4-related visualization drivers and data analysis tools are available.

One Geant4 project is comprised of several C++ source files, so they can be edited by any ASCII file editor, and then the users can compile them using a C++ compiler. It means the users have to separate the editing and compiling processes, which is not convenient in practice. An IDE (Integrated Development Environment) tool can be used to develop a Geant4 application. The introduction of an IDE facilitates the development of a Geant4 application because the editing and compiling are integrated together. Besides, if the user specifies the source directory of Geant4 in the IDE, the IDE can help remind the user in writing codes, so there is no need for the user to remember all Geant4-defined and user-defined functions or variables. The available IDEs for Geant4 include Code::Blocks, CodeLite and Qt Creator. Because none of them are designed specifically for the Geant4 development, the user is required to configure the

settings of these IDEs to make them capable of being used to develop a Geant4 application. We built a Geant4 application template in this research using Code::Blocks following the instruction by Zhang (Zhang G's Blog 2010). We also made some other settings so that data analysis functions were integrated into the development process of a Geant4 application using Code::Blocks.

One Geant4 application structure should at least include one main function and three mandatory derived classes to define the primary particle source, geometry and physics. Some other source files can also be included, if needed. Usually one complex application can include a lot of source files to implement different functions. Below we will introduce some basic concepts of Geant4 toolkit to assist readers to better understand our research. Most of the statements below are concluded from the user manual for application developers (Geant4 collaboration 2011a), the physics reference manual (Geant4 collaboration 2011b), Geant4 tutorials and our experience in this research.

3.3.1 Primary Particle Source

The user must define a derived class from `G4VUserPrimaryGeneratorAction` class to define the primary particles for an application. In the `GeneratePrimaries()` method of the user-derived class, the user can define the primary particle initial information, such as type (name) of particles, energy, starting position, flying direction (momentum direction), etc., each of which can be either a constant or described with a distribution function. Finally, the user should invoke the `GeneratePrimaryVertex()` method to generate a vertex of this primary particle for the current event (the concept of

event will be explained later). One more convenient way to define primary particle is using UI (user interface) commands to avoid writing the long C++ code to define the primary particle source. In this research, we used G4GenearlParticleSource class's UI commands to define primary particles. The macro file to define primary particle source is listed in Appendix A.

3.3.2 Geometry

It is mandatory for the user to derive a class from G4VUserDetectorConstruction to define geometry for the application. The name of this base class can be misleading because it contains a "Detector." Some beginners may think this class is used to construct a detector to detect the radiation by mistake. Actually, this class is used to set the geometry-related information for one application. In the method Construct(), the user should instantiate all necessary materials and volumes of geometry.

Geometry has three conceptual layers: solid volume, logical volume and physical volume. One solid volume determines the shape and size. One logical volume determines material, sensitivity (if the volume can be used as a radiation detector), visibility (color, opacity, visible or invisible, and wireframe or solid) and user limits (set the upper limit for a tracking step, etc.). The user can instantiate sensitive detectors and set them to the corresponding logical volumes, and then add one or more scorers to the detector, so that the selected logical volumes become detectors and can be used to score quantities of interest. One physical volume determines the position and rotation of a volume in space.

Some advanced topics of geometry including Boolean operation of solid volumes, reflected physical volumes (mirrored geometry), replication of daughter volumes in mother volume, and voxel geometry, etc. were also used in this research.

3.3.3 Physics List

By default, no particles and physics processes are defined. The user should derive a class from G4VUserPhysicsList base class, and define all necessary particles and all necessary physics processes, and set cuts for particles. The construction of particles is very flexible and there are several different construction methods. For example, the user can construct particles only by name, like proton, electron, and gamma. The user can also construct particles by category, like bosons, leptons, ions, mesons and baryons. Transportation process is assigned to all particles by invoking AddTransportation() method, which only controls the transport of particles without interaction with matter. Electromagnetic (EM) physics processes can be assigned to corresponding particles. For example, photoelectric effect, Compton scattering, and gamma conversion (mainly electron-positron pair production) can be assigned to gamma radiation. Multiple scattering, bremsstrahlung, and ionization can be assigned to electrons. For protons, the possible EM physics processes are multiple scattering, ionization and bremsstrahlung. Hadronic physics processes can also be invoked. For example, the elastic and inelastic scattering processes of protons and neutrons belong to the category of hadronic physics. Hence, to consider the production of secondary neutrons in proton therapy, hadronic physics processes should be added for protons and

neutrons. Decay process can also be specified for some particles like muons, pions, and leptonic taus.

The traditional “cut” in some Monte Carlo codes like MCNP(X) refers to energy threshold below which the particle tracking process is terminated and the remaining kinetic energy is deposited locally. This method sometimes is a good estimation and can save simulation time. However, this energy cut will bring error in determining the exact ending point of a particle trajectory, and further the energy deposition point is not accurate. In Geant4, a new method is adopted. The concept of “cut” in Geant4 refers to the production threshold of range (in the unit of length) in a medium. When a particle does not have enough energy to produce a secondary particle which can travel at least the distance of the “cut” value, this original particle will lose energy continuously until it stops in the medium with zero kinetic energy or pass through current medium, which means no secondary particles tracks will be produced along the rest path of this original particle trajectory. This method can guarantee the particle energy deposition point is correct in the matter. Not all particles are needed to be assigned a range cut value because the concept of “cut” in Geant4 is the production threshold of secondary particles. Hence, only gamma, electron, positron and proton are assigned cut values, for that they are the possible secondary particles from the interactions of particles with matter. The default cut value is 1 mm for these four particles in any matter. The user can set new cut values for different particles, and can set different cut values in different geometrical regions. Actually, in Geant4 the production threshold range values will be converted into corresponding energy values in different materials according to the compositions and

densities. This conversion process is only a simple estimation but not an exact calculation.

Besides the commonly-used standard EM physics list, some other EM physics lists are also provided in Geant4, such as optical physics, low-energy EM physics and high-energy EM physics, etc. The energy ranges are different in these physics lists and the user should choose a proper physics list according to the application. For example, if the user wants to simulate a microdosimetry problem, it is best to choose the low-energy physics list.

Some pre-packaged physics lists are provided in Geant4. If the user uses a pre-packaged physics list, one does not need to repeat deriving a physics list from G4VUserPhysicsList base class. We preferred using a pre-packaged physics list containing basic EM physics and hadronic physics to avoid missing some necessary physics processes for proton therapy. In addition, the user can add new processes to the selected pre-packaged physics list. Jarlskog and Paganetti have compared the differences between experimental results and simulation results from different physics settings for proton therapy, and their measurements showed that standard EM physics and binary cascade models for hadrons produced more accurate results (Jarlskog and Paganetti 2008). This setting refers to the QGSP_BIC (QGSP means quark gluon string precompound model, and BIC means binary cascade model) physics list, which is recommended for use below 200 MeV. However, the maximum proton energy used in our research was 250 MeV, so we chose QGSP_BERT (BERT means Bertini cascade model) package as our physics list, in which the energy in the Bertini cascade model

could be up to 10 GeV. The QGSP_BERT is the most recommended physics list for high-energy physics by the Geant4 collaboration.

The different selections of physics processes and settings of production thresholds will result in differences in the simulation results. For an application, it is best to validate the simulation with measurement. For our research, due to the lack of measurements, it was not necessary for us to validate all available physics lists, and one fixed physics list was adequate.

More topics about physics processes can be found in the Geant4 physics reference manual and Geant4 official tutorials.

3.3.4 Visualization and User Interface

Lots of visualization drivers and user interfaces (UIs) have been applied in the Geant4 simulation. These visualization drivers include OpenGL, DAWN, VRML, HepRep, RayTracer, OpenInventor, gMocren and ASCII tree. These visualization drivers implement the functions to directly or indirectly show the geometry models, particle trajectories and, moreover, the interaction points of particles with matter and the simulation results. More details about the visualization drivers can be found in the Geant4 user manual and Geant4 official tutorials.

It must be mentioned that not all these drivers are compatible with each other in the same compilation platform. Sometimes, one incompatible visualization driver can result in a lot of compilation errors. The only solution is deleting the incompatible one. Our preferred drivers are OpenGL and HepRep (High Energy Physics REPresentables) because more options were available for OpenGL and several standalone software

packages were available for opening HepRep files, such as HepRApp and JAS3 with the WIRED (World-Wide Web Interactive Remote Event Display) plugin.

The function of one UI is to provide an interactive interface for users. When executing an application, the users can type some Geant4-defined or user-defined commands in the input box of a UI to control the visualization of geometry and trajectories, and/or the execution process of the application.

An OpenGL visualization driver with Qt control (Qt is a cross-platform application and UI framework) is a new and advanced user interface, which facilitates the use of the Geant4 applications. The users can execute the UI commands conveniently and the problem geometry and particle trajectories can be shown in an integrated window, so that the users can have a direct impression for the problem and it is useful to help check the errors of particle source, geometry and physics.

3.3.5 Event and Run

An “event” is the basic unit of a simulation in Geant4, in which all the primary and secondary particles are tracked one by one. The concept of “run” in the Geant4 simulation stands for a collection of events which share the same geometry and physics settings, and it is a loop of specified number of events. The geometry and physics settings cannot be changed in a run, but they can be changed between runs in one execution of the application. This feature makes it possible to simulate dynamic geometries in an application. This was a key reason we chose Geant4 as our simulation tool for proton therapy because the treatment process is dynamic either for the passive-scattering technique or the active-scanning technique. For the passive-scattering

technique, the rotation angle of the range modulation wheel can be changed by a fixed degree in the same rotation direction between any two successive runs. If the number of runs is large enough, the effect is that the wheel is spinning at a constant speed in the whole simulation.

A class derived from `G4EventAction` can be used for setting some actions before and/or after processing one event. Similarly, a class derived from `G4RunAction` can be used for setting some actions before or after processing one run. Usually, the simulation results from one event can be extracted in the `EndOfEventAction()` method, and results from one run can be extracted in the `EndOfRunAction()` method.

The processing of one event is managed by `G4EventManager` class, and the processing of one run is managed by `G4RunManager` class.

3.3.6 Track and Step

`G4Track` class defines the track in Geant4. Note that the concept of a track is not the concept of a particle trajectory. A track object is a snapshot of a particle that is being tracked in matter. During the tracking process, a track always keeps the current information of the particle being tracked, for example, particle name, current charge, current energy, current position in space and current momentum direction. At the end of one event, there will not be any track objects retained. So, if the user wants to record all information during the tracking process of a track, the trajectory class should be used. `G4TrackingManager` is used to manage the tracking process. `G4UserTrackingAction` is the optional action class for the tracking process.

G4Step class defines the step in Geant4. A step keeps the “delta” information of a track. A track is not a collection of steps but is updated by steps. One step owns two step points; one is called preStepPoint and the other is called postStepPoint. The step keeps the information including step length, total energy deposition in this step, the remaining energy, and the physics process defined at this step, etc. Each step point knows the volume in which it is located and the corresponding material of the volume. If a step is limited by a volume boundary, the step point physically stands on the boundary, and it logically belongs to the next volume. G4SteppingManager class is used to manage the stepping process and the G4UserSteppingAction is the optional action class for the stepping process.

3.3.7 Sensitive Detector and Scorer

If a problem geometry, primary particle source and physics list have been successfully constructed, the particles will be tracked in the problem geometry “silently,” which means there will not any useful information scored and printed out by default. It is the user’s responsibility to provide the corresponding codes to extract the required information from the tracking process. The most common method is registering a sensitive detector to a logical volume, and optionally adding some scorers to this detector. G4VSensitiveDetector is the virtual base class for a sensitive detector object, and its daughter class G4MutiFunctionalDetector is the most commonly-used class to define a multiple-functional detector, which can own several different primitive-scorer objects, each of which is used to score one physical quantity in the registered volume. Several primitive-scorer classes have been provided in Geant4 to score the commonly-

used physical quantities like energy deposition, dose, particle current and number of secondary particles. The user can also define the detector class or primitive-scorer class to meet any special requirement. Actually, the ProcessHits() method used in a scorer class is the most important function in which the quantities of interest are obtained from each step object in the tracking process. In Geant4, “hit” is a concept standing for the physical quantity of interest in the sensitive volume. A hit defined by G4Hit class can keep the interaction information of one track or the accumulated information of all tracks in the sensitive volume. For example, if the user is interested in the energy deposition of each step, a hit can be defined to keep the energy deposition in one step. If the user is interested in the energy deposition from all possible tracks in the whole event, a hit object can be defined to keep the energy deposition from all steps from all tracks passing through the sensitive volume. Further, the user can also accumulate the hits for all events in the whole run. This flexible hit concept makes it possible to obtain tracking information either from a step or from all possible steps in one event or the whole run or all runs. The information kept by hits is stored in a hits map which can be extracted into an ASCII file or a binary file. A particle filter can be set for a primitive scorer, so that only the specified type of particles will produce a hit. If it is necessary to know the number of neutron steps in a volume, we can set “neutron” as the parameter of a particle filter and assign this filter to the scorer.

More expanded and advanced topics in obtaining the information of the tracking process can be found in the Geant4 user manual and Geant4 official tutorials.

3.3.8 Scripts for Simulation

The Geant4 toolkit has provided a lot of useful UI commands to implement different functions. The users can also define their own UI commands in a derived class from G4UImessenger. When executing one application, it is not practical to type the UI commands one by one in the input box or command line. The common method is putting all necessary UI commands in a script, called a macro file in Geant4. This macro file can be invoked by the application directly and the UI commands in it will be executed one by one. One macro file can also invoke another macro file. It is very useful to define a running loop in a macro file. For example, it is possible to set the rotation angle of the range modulation wheel as a variable, and invoke a loop for many runs in each of which the rotation angle is increased by a constant degree to simulate the spinning process of a range modulation wheel.

3.3.9 Data Analysis Interface

The data analysis function is not provided in Geant4, which means the users cannot obtain the simulation results with statistical information, such as expected value and standard deviation or relative error directly from a Geant4 simulation unless the user provides the corresponding formulas in calculating the statistical quantities. Due to the flexibility of Geant4, the user can invoke some analysis tools based on the AIDA (Abstract Interfaces for Data Analysis) interface in their applications to perform the data analysis with statistical information directly and/or indirectly from the simulation. The user should set an environmental variable called “G4ANALYSIS_USE” to “1” to use the data analysis function. The corresponding header files of AIDA should be included

in the Geant4 application source codes. One recommended method is creating some histogram objects to store the required simulation results and saving these histograms into one binary file with a suffix “.aida,” which can be opened using JAS3 or OpenScientist. The filling process of the histograms is usually invoked in the action method at the end of an event or a run. The results in the histograms can be plotted directly and the statistical information can be shown optionally.

In addition, another data analysis package called root can be used together with a Geant4 application, and the information of interest can be stored in one binary file with a suffix “.root,” the data in which can be analyzed by root package. Some basic concepts of root will be discussed below, so that the simulation results from the current research will be understood more clearly. Note that root has no relation with AIDA, even though there are some similar concepts, like histograms.

The class G4AnalysisManager is used to manage the data analysis in an application, but it was not used in our research and another method was defined to manage the data analysis to meet our special requirements to store the simulation results from a series of runs in one root file.

3.3.10 Dynamic Geometry

Each time, when the executable file of a Geant4 application is invoked, this process is called an execution. In one execution, there can be a series of runs. In each run, there can be a number of events. In each event, one and more particle tracks can be tracked. Each track is updated by steps. Understanding this logical order is very important. In one run, the primary source, geometry and physics settings are fixed and

cannot be changed during the whole run. But these settings can be changed between two runs in one execution. This provides a solution for us to perform a dynamic simulation. We mainly discuss the dynamic geometry problems in this section.

Between two runs, the number of volumes can be changed; the size and material of one volume can be changed; the location and rotation angle of one volume can be changed.

Each time, when the geometry has been changed, the user must invoke the `G4RunManager::GeometryHasBeenModified()` method to notify the Geant4 kernel to guarantee that before next run, the kernel can reset the navigator and the new geometry settings can become effective in the next run.

To obtain an SOBP dose curve, a range modulation wheel was used in our research. We first defined a rotation matrix pointer for the mother volume of the wheel, and then we defined one function to reset the rotation angle of this rotation matrix. We connected a user-defined command “/modulator/deltaAngle” with this angle-resetting function. We put this UI command in a running loop for one execution. In each run, the increment of the rotation angle was a constant to guarantee that the wheel was spinning at a fixed speed. In this research, we set this angle increment to 0.25 degree, and set a fixed number of events in each run to ensure the simulation was as close as to a real clinical treatment process.

3.4 Data Analysis Tool Root

Root was the data analysis tool used in this research. Due to its important role in recording and analyzing our simulation, it is necessary for us to discuss the basic concepts of root in a separate section.

Root is an object-oriented data analysis framework aiming at solving the data analysis challenges of high-energy physics (The ROOT team 2009). Its original co-authors were Rene Brun and Fons Rademakers. In the mid-1990s, they found the twenty-year-old libraries based on the FORTRAN language had reached their limits, and these tools could not scale up to the challenges from the Large Hadron Collider, where the data were a few orders of magnitude larger than anything seen before. Brun and Rademakers decided to apply object-oriented design in developing a data analysis package. Meanwhile, a C++ language interpreter called CINT had been developed by Masa Goto in Japan. Finally, CINT was adopted in root as the interpreter for the command line and script processor. The first edition of root was released to public in 1995 and up to the date we finished our project, the stable version was 5.32/00 released on December 2, 2011, the same day as the release of Geant4.9.5.

Root has a framework structure. The advantage of root is that the basic utilities and services, such as input/output and graphics are already provided in this framework. In addition, histograms and data fitting are provided. The user can use them directly. The drawback of a framework is that the application is constrained by this framework, which means the user must follow its styles and requirements.

The most useful concepts of root for our research include histograms, files and trees.

A histogram object can be in the form of 1D, 2D or 3D. For a 1D histogram, the x-axis with a fixed range is divided into several channels, each of which is called a bin in root. The filling process of a histogram is putting data in the corresponding bins, very similar to shooting a number of bullets at a target and counting the number of bullets in each ring. Assuming a bin has a lower boundary and an upper boundary, if x coordinate of a sample falls in this bin, the counts in this bin will be increased by one. In practice, each sample can also have a weight, and in that case, the filling process of a histogram is not adding one to that bin, but adding the weight to that bin. Similarly, in the 2D and 3D cases, one bin has two coordinate boundaries and three coordinate boundaries. A very useful application for our research was using a 1D histogram to store the depth dose distribution. In addition, we used a 2D histogram to store a planar dose distribution and used a 3D histogram to store a three dimensional spatial dose distribution.

The concept of a root file with the suffix of “.root” can be understood as a container, and the user can store data of interest in this container.

The concept of a tree can be understood as a folder or a directory in a root file. Like a real tree in reality, the tree object can have several branches, and one data object can be put in one branch. The data object can be a random variable, or a histogram object. For our research, if we defined a step in the tracking process as the sample, a lot of useful information could be extracted from this sample. We defined a random variable for each piece of information. The variables on different branches of a tree could include

the x coordinate, y coordinate, z coordinate, kinetic energy, polar angle of momentum direction, azimuthal angle, the particle name and energy deposition in this step. Invoking the filling process of the tree means filling data for all the branches on it. Invoking the writing method of a file means the tree objects and other objects will be stored in this file and then the file will be saved on the hard disk.

3.5 DICOM Images

DICOM (Digital Imaging and Communications in Medicine) is a standard for medical imaging (DICOM introduction and free software 2012). Usually one DICOM medical image has a suffix of “.dcm.” We can simply think a DICOM medical image has two layers of data: one is file meta information and the other is data set. The DICOM images can be produced from different imaging modalities like MRI (Magnetic Resonance Imaging), CT (Computed Tomography), PET (Positron Emission Tomography), SPECT (Single-Photon Emission Computed Tomography), PEC-CT, SPECT-CT and ultrasound. The principles for these imaging techniques and the processing of medical images will not be discussed in this dissertation, and they can be found elsewhere (Dougherty 2009; Gonzalez and Woods 2008).

The file meta information contains the header information of a DICOM file. The first element indicates whether the file is in a DICOM format or not. Different unique tags in meta information are used to indicate different attributes of the file, such as file name, width and height of the image, the modality of obtaining this image, the private information of the patient, number of rows and columns in this image slice, space between two slices, location of this slice, and color type of this slice, etc.

The data set in a DICOM image can be treated as a matrix (two-dimensional array). The value in each pixel (picture element) stands for the intensity in that pixel. For an image from CT scanning, the intensity stored in a pixel actually is the CT number in Hounsfield unit (HU), which was named after Godfrey Newbold Hounsfield, one of the 1979 Nobel Prize awardees for physiology and medicine.

The definition of CT number in HU is:

$$HU = \left(\frac{\mu_m}{\mu_{water}} - 1 \right) \times 1000 \quad (4)$$

where μ_m is the linear attenuation coefficient of the CT x ray in a voxel filled with a material marked as m, and μ_{water} is the linear attenuation coefficient of the CT x ray in a water medium. According to this definition, the CT number for water is 0. For air, it is close to -1000 because the attenuation coefficient of x ray in air is much smaller than the one in water. The CT numbers for lung, soft tissues and fat are negative, and the CT numbers for muscle and bone are positive. The nominal energy of the x ray to the CT number has been averaged over the energy spectrum of the CT x ray. It is assumed that the attenuation has been corrected for the beam hardening effect (Zhou 2011), so that the x-ray energy spectrum is treated to be fixed in all voxels.

For a compound or mixture, the total linear attenuation coefficient is given by:

$$\bar{\mu} = \rho N_A \sum_{i=1}^n \left(\frac{w_i}{A_i} \bar{\sigma}_i \right) \quad (5)$$

where ρ is the mass density of the material, N_A is the Avogadro constant, w_i is the elemental weight of element i , A_i is the mass number of element i , and $\bar{\sigma}_i$ is the total

photon interaction cross section of element i averaged over the x-ray energy spectrum (Zhou 2011). For the CT x-ray energy range, 50 to 200 keV, Compton effect is the dominant interaction process, so $\bar{\sigma}_i$ can be replaced by the Compton scattering cross section (Zhou 2011). It is approximated by:

$$\bar{\sigma}_i \approx \bar{\sigma}_{i,Compton} = Z_i \bar{\sigma}_{KN} \quad (6)$$

where $\bar{\sigma}_{i,Compton}$ is the average cross section of Compton scattering, Z_i is the atomic number of element i , and $\bar{\sigma}_{KN}$ is the average Klein-Nishina cross section (Attix 2004), a constant for a fixed energy spectrum. The total linear attenuation coefficient can be expressed by:

$$\bar{\mu} \approx \bar{\sigma}_{KN} \rho N_A \sum_{i=1}^n \left(\frac{w_i}{A_i} Z_i \right) \quad (7)$$

Analyzing the formula, $\rho N_A \sum_{i=1}^n \left(\frac{w_i}{A_i} Z_i \right)$ is the electron density of this material in the unit of cm^{-2} .

Based on above discussion, we conclude that the CT number has a relation with the electron density of the material in the voxel. Hence, different materials will have different CT number ranges.

Parker et al. suggested a linear relationship between CT number and electron density (Parker et al. 1979). In practice, it is recommended that the CT scanner be calibrated with an electron density phantom to accurately measure the relationship between CT number and electron density. A calibration curve can be plotted according

to the measurements. Later, using the calibration curve, a CT scan of a real patient, filling with CT numbers, can be converted into an electron density matrix. Further, if we have a material table containing the material name and electron density range, we can convert the electron density matrix into a material name matrix or material ID matrix. Zhou's calibration results for CT number and electron density are shown in Figure 3-1 (Zhou 2011). We adopted a different conversion method. Our method was to convert the DICOM image into a material density matrix and a material ID matrix using the calibration curve of CT number and material density (not electron density), shown in Figure 3-2, which was plotted by us using the calibration data provided in the DICOM example (Archambault et al. 2011) released with Geant4. Our conversion method was also different from the one used in the Geant4 DICOM example, because their conversion method could result in wrong density values for some materials, which has been reported via the Geant4 bug reporting system.

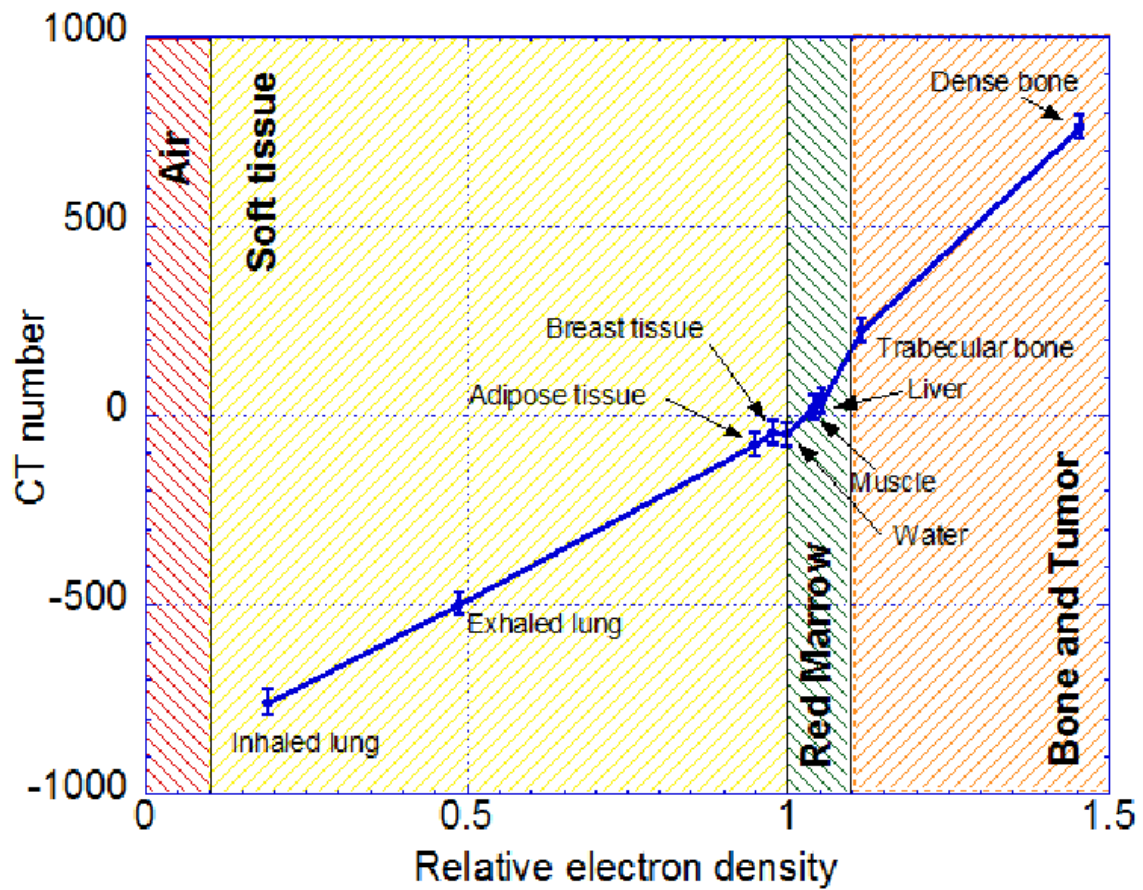


Figure 3-1. CT Numbers vs. Relative Electron Density for All Tissue-Equivalent Inserts
Material groups are shown with corresponding relative electron density range.
(Zhou 2011)

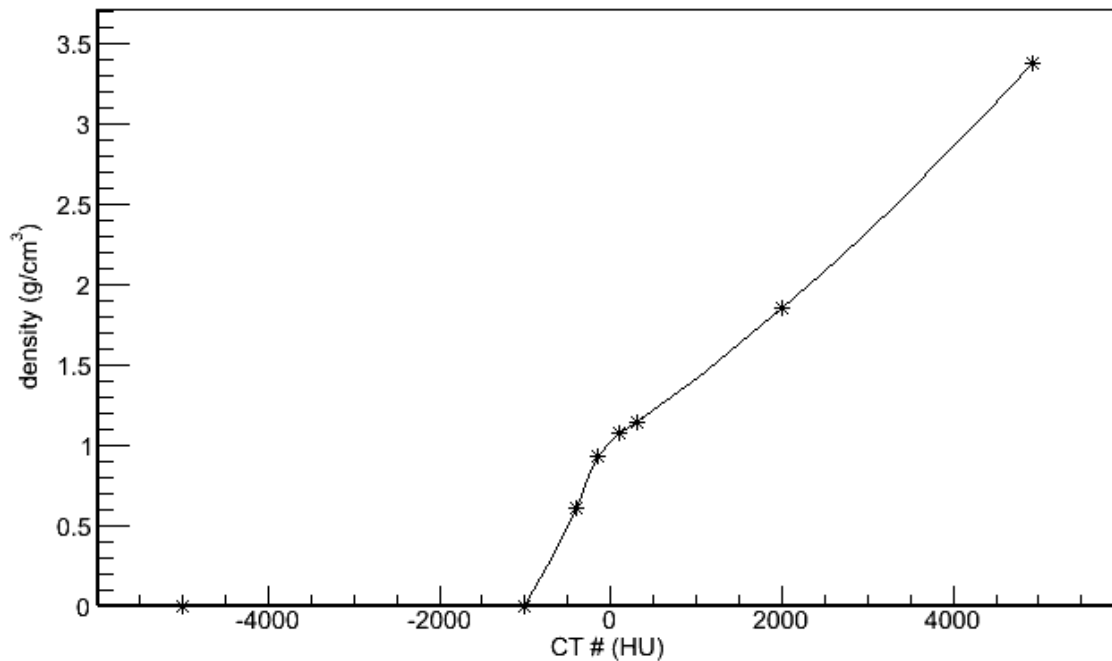


Figure 3-2. Calibration Curve of CT Number and Material Density

3.6 Method to Convert DICOM CT Slices into a Voxel Geometry

The conversion of DICOM CT slices to voxel geometry in the Geant4 DICOM example is accomplished by their defined class called DicomHandler. Actually, the conversion method in that example is a pure C++ operation, but not related to the Geant4 built-in functions. Some C++ I/O operation functions are invoked to read in the meta file information of each CT slice and output the geometry and material information to an ASCII file. The ASCII files are then used as input parameters to build a voxel geometry using the Geant4 built-in classes.

This example had some deficiencies. The first one was that the z coordinates of CT slices were incorrect (actually they were reversed in the CT header information), so

the patient geometry constructed from their conversion was completely reversed from the true patient body. Second, there were some wrong parameters for defining elements for materials, which we reported to Geant4 bug tracking system. Third, their density conversion method was not correct. For example, the density of lung-exhale material should be larger than lung-inhale. However, after conversion in that application, the lung-exhale material density was decreased to the same density of a lung-inhale material.

The most valuable part in this example was the construction method of the patient phantom. A derived class from G4PhantomParameterisation was used as a parameter to construct the voxel geometry of the patient phantom, and G4RegularNavigation class was used to navigate the particle tracking process in regular voxel geometry, which was the fastest simulation way without any extra memory requirement.

Due to the inflexibility of this DICOM example, we did not use their class to deal with medical images in our research, but we adopted their patient phantom construction method and their CT number and material density calibration data.

One DICOM medical image or a series of images can be opened using a lot of software, such as ImageJ (Abramoff et al. 2004), ITK-snap (Yushkevich et al. 2006) and InVesalius (InVesalius 2012), etc. It also can be analyzed using MATLAB (MATLAB 7.12.0, The MathWorks Inc., Natick, MA, 2011). The dicominfo() function in MATLAB can be used to read in a DICOM image, and the return type is a structure which contains the file meta information. The dicomread() function can return a 2D matrix containing the intensity values in all pixels. The intensity directly obtained in MATLAB is not the

CT number, but we can use the slope and intercept stored in file meta information to convert the intensity to CT number linearly. We defined some functions to convert the CT number matrix into the material density matrix according to the calibration curve in Figure 3-2 using linear interpolation method, and further into material ID matrix. We checked the file meta information and the images carefully to ensure the spatial order of output matrices was correct. We specified a coordinate system for the patient voxel geometry. The bottom slice (feet) was at the lower z-position and the top slice (head) was at the higher z-position. Left hand was at the higher x-position, and right hand was at the lower x-position. Front was at the lower-y position and back was at the higher y-position. The patient geometry should be rotated and positioned to a correct position and alignment in space coordinates in the treatment simulation according to the tumor position and the treatment strategy.

When we discuss the planar image, a pixel is the basic unit storing image intensity information or CT number. Each CT slice has a center location and a thickness, so its lower extension boundary is equal to its center location minus a half-thickness and the upper extension boundary is equal to its center plus a half-thickness. Hence, this planar image can be converted to a three-dimensional geometry with only one layer. One pixel in planar image will be converted to a voxel in volume.

Using MATLAB, we can check the information of one CT slice intuitively and find the errors in it. Essentially, the conversion process performs some mathematical operation on the image matrix. The whole processes are listed below and part of the source codes are listed in Appendix B.

3.6.1 Obtain the Slice Information

The CT slice information can be obtained using the `dicominfo()` function, and the return value is a “struct” type variable. The detailed information of the CT slice can be listed. The required information include position of image, number of rows, number of columns, extensions of the image, length and width of each pixel, and slice thickness.

3.6.2 Convert Intensity to CT Number

As mentioned above, the value stored in a pixel is intensity (16-bit unsigned integer type), but not the CT number (16-bit signed integer). We can use the `RescaleSlope` and `RescaleIntercept` values in the slice meta file information to convert the intensity to CT number. The conversion formula is:

$$\text{CT number} = \text{RescaleSlope} \times \text{intensity} + \text{RescaleIntercept}. \quad (8)$$

Usually the value of `RescaleSlope` is 1 and the value of `RescaleIntercept` is -1024.

After conversion, the original image matrix with intensity is converted to a matrix filled with a CT number in each pixel.

3.6.3 Convert CT Number to Material Density

The conversion process from CT number to material density is based on the calibration curve in Figure 3-2 using linear interpolation method.

After conversion, the CT number matrix is converted to a material density matrix.

3.6.4 Convert Material Density to Material ID

There is a conversion table for converting material density to material ID listed in Table 3-1. The values are from the Geant4 DICOM example.

Table 3-1. Material Density and Material ID

Density Range (g cm ⁻³)		Material	
Lower boundary (≥)	Upper boundary (<)	Name	ID
0.0	0.207	Air	0
0.207	0.481	Lung inhale	1
0.481	0.919	Lung exhale	2
0.919	0.979	Adipose	3
0.979	1.004	Breast	4
1.004	1.043	Phantom	5
1.043	1.109	Liver	6
1.109	1.113	Muscle	7
1.113	1.496	Trabecular bone	8
1.496	1.654	Dense bone	9

For example, if the material density in one pixel is equal to or greater than 0.207 g cm⁻³ and less than 0.481 g cm⁻³, this material name is lung inhale and ID is 1.

3.6.5 Create a New Material Density and Material ID Table

From Table 3-1, we can see there is a density range, but not a fixed density value for a specified material. But in Geant4, the user has to assign a fixed density value for a specified material name. The density range in Table 3-1 is relatively wide, so it is not reasonable to use the middle point of the density range as the fixed density for each material. We can divide each density group into several sub-groups, and use the middle point of each sub-group as the fixed density for each sub-group. The density interval of each sub-group was set to 0.1 g cm⁻³, but if the upper edge of the mother group was close to the upper edge of that sub-group, the upper edge of the mother group was used instead. The new material sub-group and new material ID are listed in Table 3-2.

Table 3-2. New Material Density and New Material ID

Upper boundary (g cm ⁻³) (<)	New density (g cm ⁻³)	Old Material ID	New Material ID
0.100	0.0012 (Air)	0	0
0.207	0.1535	0	1
0.300	0.2535	1	2
0.400	0.350	1	3
0.481	0.4405	1	4
0.600	0.5405	2	5
0.700	0.65	2	6
0.800	0.75	2	7
0.919	0.8595	2	8
0.979	0.949	3	9
1.004	0.9915	4	10
1.043	1.0235	5	11
1.109	1.076	6	12
1.113	1.111	7	13
1.200	1.1565	8	14
1.300	1.25	8	15
1.400	1.35	8	16
1.496	1.448	8	17
1.600	1.548	9	18
1.654	1.627	9	19

If the density of material is less than 0.1 g cm⁻³, the density of air (0.0012 g cm⁻³) is used for the new material. If the density of material is greater than 1.654 g cm⁻³ (very seldom except for urinary stones and mandible, etc.) (ICRU 1992), 1.627 g cm⁻³ (average of 1.600 and 1.654) is used as the new density.

In Geant4, if two kinds of materials with the same elemental composition have different mass densities, they would be treated as two different materials, and they should be constructed separately. Hence, even if we have defined the ten materials in

Table 3-1, we have to redefine twenty new materials with new densities in Table 3-2 and new material names.

3.6.6 Transfer the Original Material Density to a New Material Density

Using the first two columns of data in Table 3-2, we can convert the original material density matrix to a matrix filled with new material densities.

3.6.7 Transfer the Original Material ID to a New Material ID

Using the data in Table 3-2, we can convert the original material ID matrix to a new material ID matrix. The new material density and new material ID will be used in Geant4 to construct new materials. The material ID is a parameter used when constructing the patient voxel geometry.

3.6.8 Compress the Original Density Matrix and Create a New Material ID Matrix

Usually, the image from CT scanning has a relative high spatial resolution. For example, a CT slice with dimensions of 40 cm \times 40 cm usually has 512 \times 512 pixels. The geometry construction time will increase if the number of pixels is large. Besides, a small voxel size will also increase the statistical error in dose scoring. It is necessary for us to compress the number of pixels in an original CT slice to a reasonable and acceptable value. We set the compression factor k to 8, the number of pixels in the new matrix will be 64 \times 64, and the dimension of each pixel will be about 7 mm \times 7 mm, which is an acceptable size for a Monte Carlo simulation to meet the statistical requirement. The original material density in a pixel in the compressed matrix is the average density of $k \times k$ contiguous voxels obtained from the original CT slice. The new material density and ID for the compressed matrices are still obtained using the data in

Table 3-2. The CT number matrix for one original CT slice (1.dcm) provided in the Geant4 DICOM example is shown in Figure 3-3. The density map and new density map for the original slice and the compressed CT slice are shown in Figure 3-4. The Material ID map and new material ID map for original and compressed CT slice are shown in Figure 3-5. Finally, the new compressed density map and new compressed material ID map are used as input parameters to construct patient voxel geometry in our Geant4 application. The directions of the patient body alignment are marked in Figure 3-3. The voxel geometry with directions including three CT slices from the Geant4 DICOM example is shown in Figure 3-6, which was constructed using Geant4 with the Qt-based OpenGL visualization driver. This is only used for the purpose of illustration in this section, not for a simulation in this research.

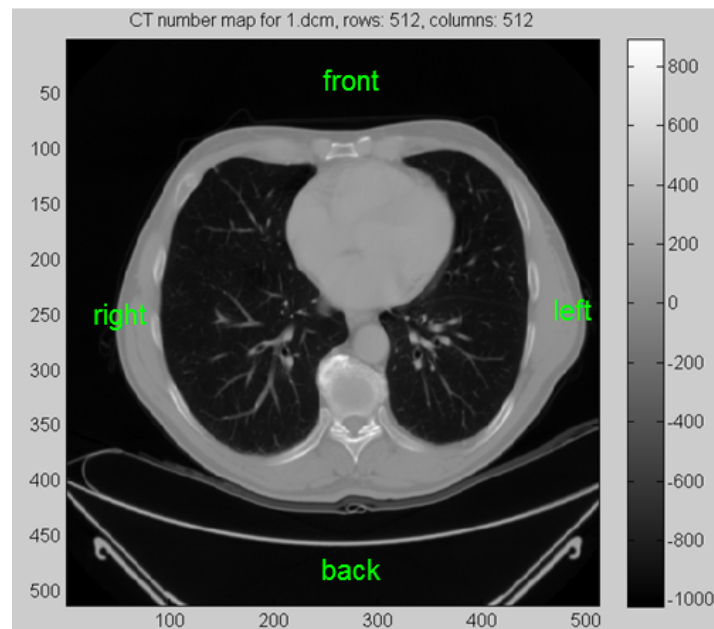


Figure 3-3. CT Number Map of an Original CT Slice

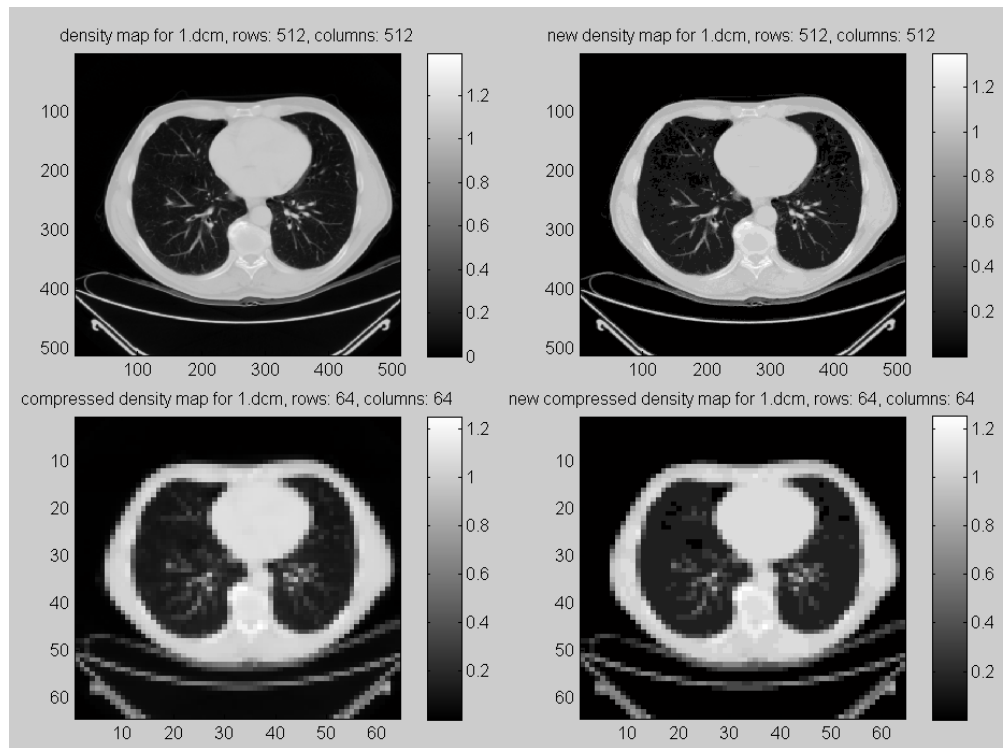


Figure 3-4. Density Map and New Density Map of Original and Compressed CT Slices

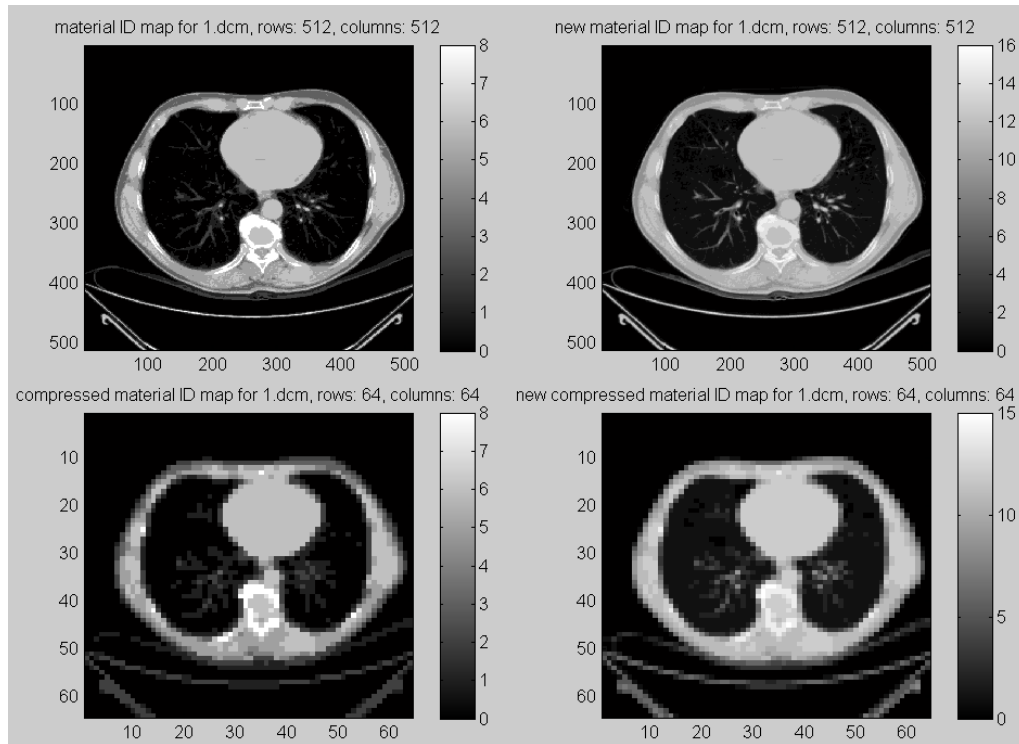


Figure 3-5. Material ID Map and New Material ID Map of Original and Compressed CT Slices

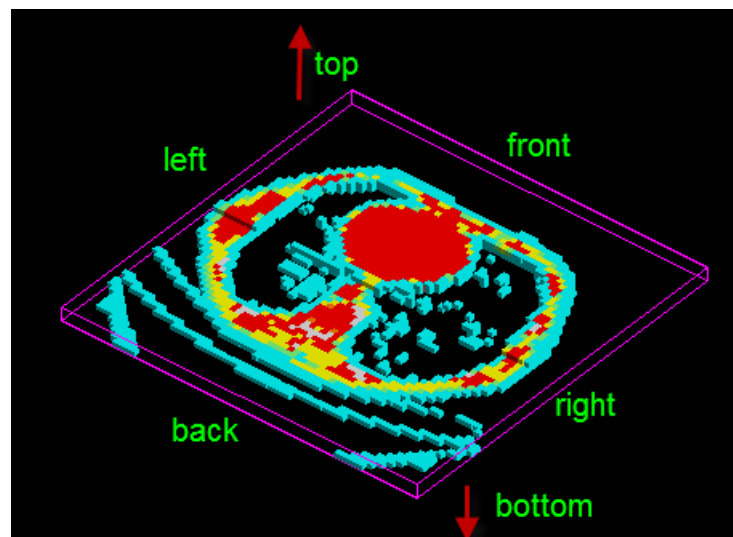


Figure 3-6. A Patient Voxel Geometry

4. SETTINGS FOR SIMULATION

In this section, we will introduce the whole programming procedure for modeling the treatment head in the Geant4 environment. Then we will provide the settings in our design and simulation.

Although Geant4 is well known for its application in proton therapy, we still need to verify it. The easiest way is using the code to obtain the depth-dose curve and comparing the position of Bragg peak and range with other Monte Carlo simulation result and datum from NIST (National Institute of Standards and Technology).

4.1 Verification of Pristine Bragg Peak and Projected Range

The synchrotron at M.D. Anderson Cancer Center can provide proton energies between 100 MeV and 250 MeV. The available eight energy intervals include 100, 120, 140, 160, 180, 200, 225 and 250 MeV (Zheng et al. 2008).

We developed a simple application using Geant4 to obtain depth-dose curves in a water phantom. The proton beams with initial energies listed above were selected to be simulated.

The source protons were limited to a disc with a radius of 3 cm on the $z = -10$ cm plane and were assumed to be transported along the z -axis. The front surface of the water phantom was on the $z = 0$ cm plane. The NIST data show that the projected range of 250 MeV protons in water is 37.9 cm (Berger et al. 2005), so a water box with a 40-cm depth is deep enough to stop the protons with the energies listed above. The size of water phantom was set to $40 \text{ cm} \times 40 \text{ cm} \times 40 \text{ cm}$. The size of each energy deposition

scoring cell was set to 40 cm × 40 cm × 0.2 cm, so there were 200 scoring cells along the z-axis. The number of primary source particles (NPS) was set to one million. The QGSP_BERT reference package was selected as the physics list including standard electromagnetic physics and hadronic physics. A root 1D histogram was used to score the dose along z-axis, and then the data stored in histogram were extracted into an ASCII file so that they could be plotted together using Excel.

The middle point of the depth bin filled with maximum dose was selected as the Bragg peak position. The lower boundary of the depth bin with zero dose (or the dose falling edge) was selected as the projected range from the simulation.

Each depth dose curve was normalized by the dose at the Bragg-peak position. The percent depth dose distribution curves from the eight groups of energies are compared in Figure 4-1.

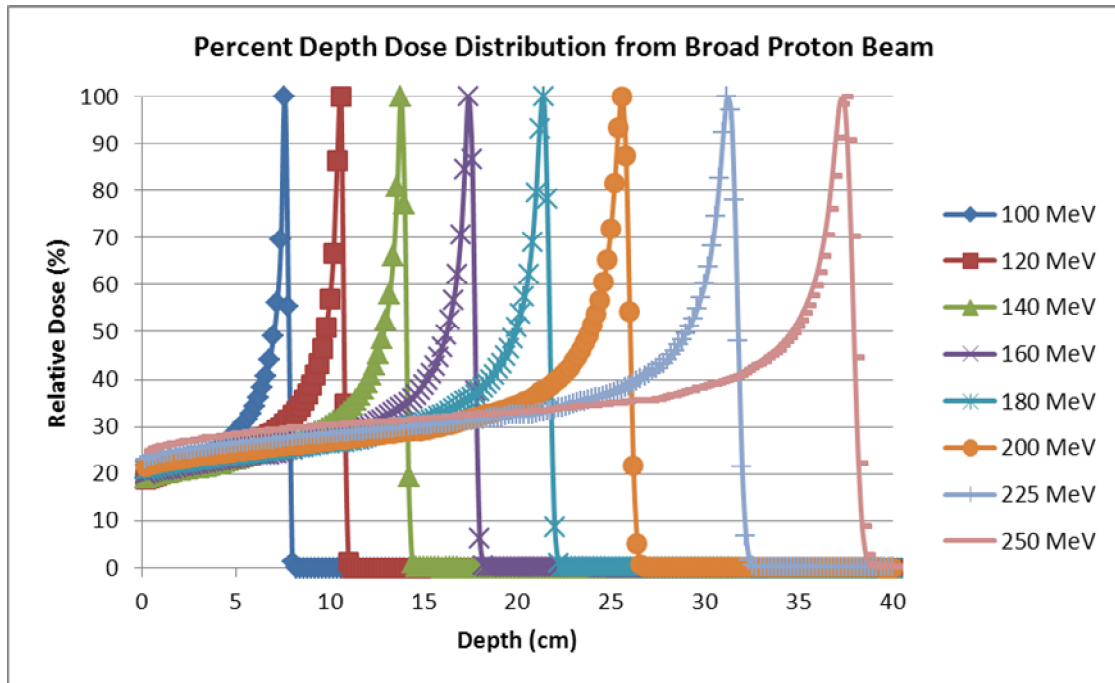


Figure 4-1. Percent Depth Dose Distribution from Broad Proton Beam

The Bragg peak positions from the Geant4 simulation results were compared with MCNPX simulation results. The projected ranges from the Geant4 simulation were compared with our previous MCNPX simulation results (Guan 2009) and projected ranges from the NIST data (Berger et al. 2005). The comparisons are listed in Table 4-1. The relative dispersion of each Monte Carlo simulated range with NIST range is also provided.

Table 4-1. The Bragg Peak Positions and Ranges in Water Phantom

Energy (MeV)	Bragg Peak (cm)		Projected Range (cm)				
	MCNPX	Geant4	NIST	MCNPX	dispersion	Geant4	dispersion
100	7.4	7.5	7.707	7.9	2.50%	8.0	3.80%
120	10.3	10.5	10.65	10.9	2.35%	11.0	3.29%
140	13.6	13.7	13.96	14.3	2.44%	14.4	3.15%
160	17.2	17.3	17.63	18.2	3.23%	18.2	3.23%
180	21.1	21.3	21.63	22.3	3.10%	22.4	3.56%
200	25.4	25.5	25.93	26.9	3.74%	27.0	4.13%
225	31.2	31.1	31.71	33.1	4.38%	33.2	4.70%
250	37.3	37.3	37.90	39.6	4.49%	39.8	5.01%

We treated the depth with zero energy deposition as the range of protons but actually the secondary neutrons and gammas have strong penetration ability and they can also lose energy in water after the final stopping locations of the protons. This explains why the range obtained from Monte Carlo simulation is greater than the value from NIST.

Both Monte Carlo simulation results have a small dispersion from NIST data. The Geant4 simulation result is a little greater than the MCNPX (only EM physics used) simulation result. One possible reason is that secondary neutrons are produced due to the hadronic physics processes used in Geant4 simulation. We think the Geant4 simulation results are reasonable and Geant4 can be used in our research. Below we will provide the settings for building the passive-scattering nozzle and the dose scoring volume using Geant4.

4.2 Geometry Settings of Nozzle and Dose Scoring Volume

The common components in a passive-scattering nozzle include the first scatterer (broadening the beam profile), the range modulation wheel (forming the SOBP dose curve), the second scatterer (flattening the beam profile), the range shifter (shifting the range backward), some collimators (limiting the beam lateral profile), the snout (housing final components), the final aperture (confining the beam profile to the lateral profile of the tumor), the patient-specific range compensator (shifting the range of the beam to the longitudinal tumor profile), and some ion chambers (monitoring the proton beam). In addition, a shielding shell is needed. The dose scoring volume can be a water phantom or a patient voxel geometry in this research.

In practice, the first scatterer and range modulation part are mounted together for each pristine Bragg peak curve, and then for all pristine Bragg peak curves, all parts are mounted together on a wheel, which is called the S1 component in this research following the tradition in the NEU codes package. The second scatter is called S2 similarly. S2 is also a two-part structure. The first part is a range compensation part and the second part is beam-profile flattener. Only S1 and S2 are complex structures, and the other components are only simple rings, half spheres, boxes or wedges.

There are not too many materials used in designing the nozzle. Both of S1 and S2 are bi-material components. Lead is used for scattering part and Lexan (plastic) is used for range compensation part. The collimators, shielding shell, snout and final aperture are made of brass. The range compensator is made of ABS resin. Other space is filled with air. The compositions and densities of the materials are listed in Table 4-2. The

CSDA (Continuous Slowing-Down Approximation) ranges of 250 MeV protons in each material are also provided (Berger et al. 2005). The elemental components for materials in the patient phantom will be provided in section 4.6.

Table 4-2. Composition of Materials and CSDA Ranges of 250 MeV Protons

Material	Composition (weight fraction by percent or atomic fraction by number)	Density (g cm ⁻³)	CSDA Range of 250 MeV Protons (g cm ⁻²)	CSDA Range of 250 MeV Protons (cm)
Lead	Pb (100%)	11.35	76.69	6.76
Lexan	H (5.5%): C (75.6%): O (18.9%)	1.2	38.98(Lucite)	32.5
ABS resin	(C ₃ H ₃ N) ₂ :(C ₄ H ₆) ₃ :(C ₈ H ₈) ₅	1.04	37.94(H ₂ O)	36.5
Brass	Cu (67%): Zn (33%)	8.07	56.62(Cu)	6.78
Air	N (75.6%): O (23.1%): Ar (1.3%)	1.205×10 ⁻³	42.90	3.50×10 ⁴
Water	H ₂ O	1.0	37.94	37.94

In our previous research, we had three energy-SOBP pairs, including 100 MeV for 2 cm SOBPs, 180 MeV for 8 cm SOBPs and 250 MeV for 10 cm SOBPs. For each pair, there are three beam-field size requirements: small size for 7.05 cm radius, medium size for 12.75 cm radius and large size for 17.7 cm radius. Field size refers to the radius of broadened proton beam incident on the front surface of the water phantom.

In this research, the S1 and S2 settings calculated previously for 250 MeV, large beam field and 10 cm SOBPs were used for the cases with the water phantom. For the

patient voxel geometry, SOBP was 6 cm, and the geometry parameters were recalculated using NEU in this research.

The geometry parameters used for this research were based on the recommendations in ICRU Publication 78 (2007) and the primary particle source settings. A recommended value of source surface distance (SSD) in ICRU Publication 78 is 300 cm. We also adopted 300 cm as the SSD in this research. We assumed the proton beam were produced on the $z = -300$ cm plane and traveling along z-axis. The front surface of the dose scoring volume was at the $z = 0$ cm plane. Because the nozzle could rotate around the patient, it was necessary to leave a gap between the nozzle and the dose scoring volume. The length of the nozzle was set to 260 cm, so the gap between the nozzle ending surface (range compensator ending surface) and front surface of the dose scoring volume was 40 cm. The geometry of the nozzle and water phantom used in this research is shown in Figure 4-2, which was produced using Qt-based OpenGL visualization driver in Geant4. The geometry shown is not exactly same as any clinical nozzles. This simplified nozzle was only used in the Geant4 Monte Carlo simulation for this research.

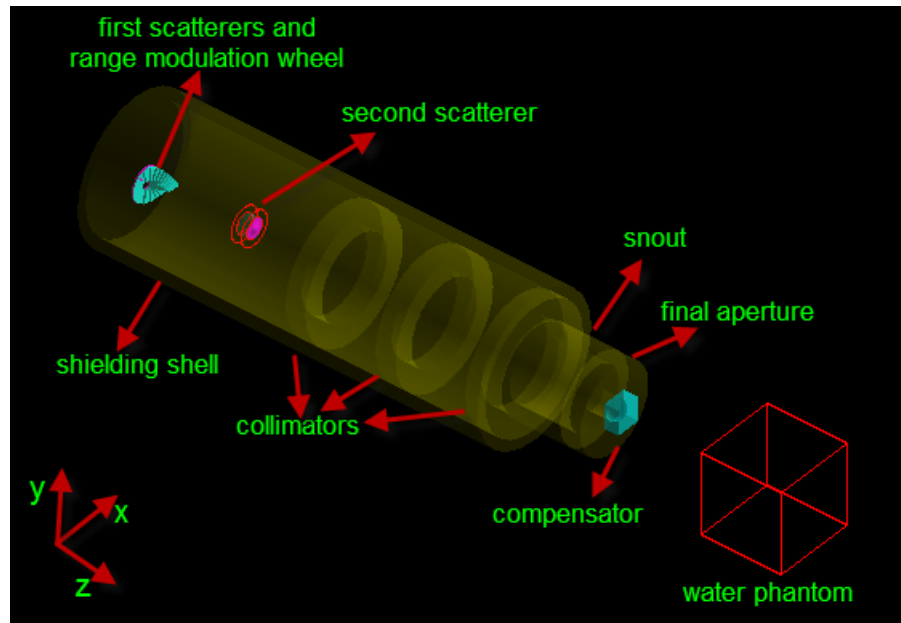


Figure 4-2. Passive-Scattering Nozzle and Water Phantom

4.2.1 Construction of First Scatterers and Range Modulation Wheel

A spinning range modulation wheel can be used to modify the energy spectrum to make the proton beam form an SOBP depth-dose distribution in the water box or the patient geometry.

The reference plane of S1 is also the mating surfaces of the two types of materials. In S1, on the left of the mating surface ($z = -290$ cm plane) is the scatterer made of high-Z material, e.g., lead, and on the right is the range modulation wheel made of low-Z material, e.g., Lexan. The parameters of S1 (250 MeV, large field, 10 cm SOBP) produced from NEU codes package are listed in Table 4-3. The weight refers to the relative width portion of each step.

Table 4-3. Parameters of S1 from NEU

Step No.	Weight	Thickness (cm)	
		Lead	Lexan
1	0.4006	0.8829	0
2	0.1378	0.8679	0.9377
3	0.0965	0.8515	1.8827
4	0.0739	0.8344	2.8317
5	0.0608	0.8166	3.7842
6	0.0513	0.7982	4.7402
7	0.0437	0.7791	5.6996
8	0.0379	0.7593	6.6627
9	0.0343	0.7388	7.6294
10	0.0287	0.7176	8.6003
11	0.0344	0.6956	9.5754

The traditional construction method of S1 is to provide the geometric parameters of each step (also called a leaf) on the wheel and then mount all the steps on one wheel. The first step has the smallest thickness and the final step has the biggest thickness. The S1 structure looks like a set of stairs, shown in Figure 4-3 (visualized using HepRApp). There are eleven steps for this S1.

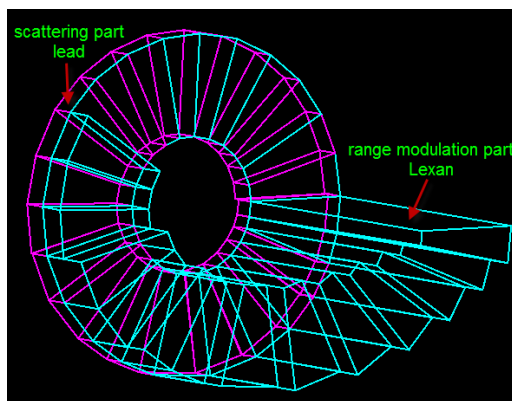


Figure 4-3. S1 Component in Stair Style

While the wheel is spinning, there is not a smooth transition between the final step and the first step, and the initial beam will suddenly fall down from the thickest part to the thinnest part. The slit between the steps may influence the final spectrum of the beam. To eliminate the influence, we can use reflected or mirrored structure to build the S1 component, so that two parts will be symmetric to each other. The S1 with symmetric structure is shown in Figure 4-4.

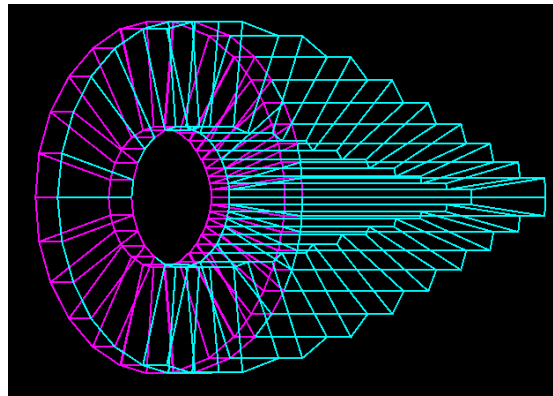


Figure 4-4. The Symmetric Structure of S1

Some range modulation wheels in other shapes are also used in some clinical nozzles. The S1 at the Massachusetts General Hospital is a multi-track structure which can be switched in different treatments to form different SOBPs widths (Paganetti and Bortfeld 2005). The S1 used in a horizontal beam delivery device at Centro di AdroTerapia e Applicazioni Nucleari Avanzate (CATANA), Italy looks like a propeller or a fan, which has more symmetric sections on the wheel. They are shown in Figure 4-5.

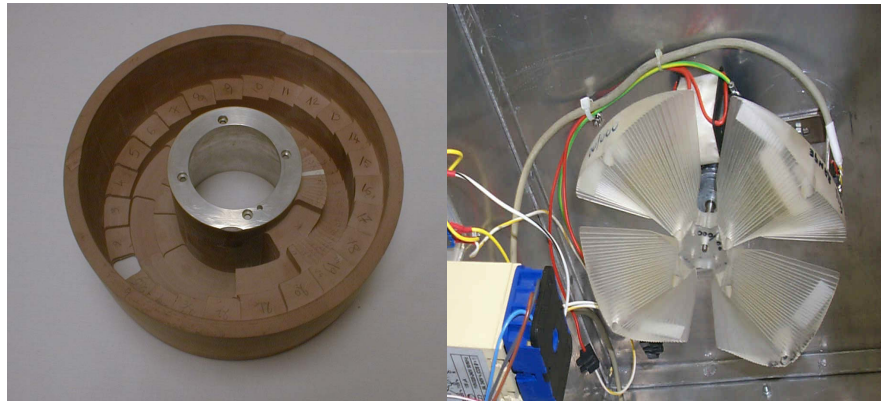


Figure 4-5. Multi-Track S1 and Propeller S1

We can also build a multi-track or a multi-section wheel. A three-section wheel is shown in Figure 4-6. Actually, we think the structure in Figure 4-4 is good enough in a simulation to obtain a smooth SOBP and it was adopted in this research. However, the structure in Figure 4-4 is not practical in reality because it is not good for balance when spinning. The multi-section structure in Figure 4-6 is good for balance when spinning.

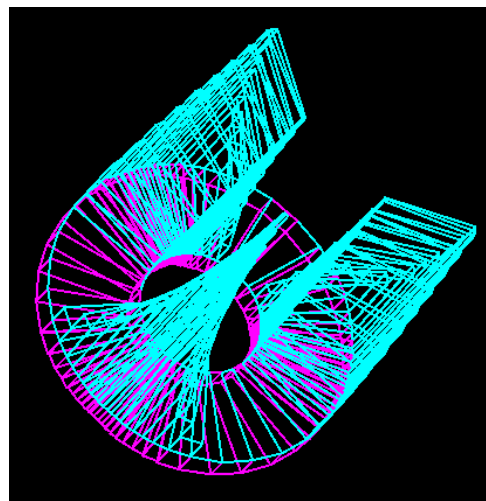


Figure 4-6. S1 with Three Symmetric Sections

Taking the multi-section propeller S1 as an example, a common method in constructing S1 using Geant4 is constructing all sections and all leaves on the wheel one by one (Cirrone et al. 2011). For example, if there are four sections and there are twenty leaves on each section, eighty leaves would be constructed one by one. It would be time-consuming to calculate the rotation angle and center position for each leaf. We developed a method in which we used two loops to construct the wheel. The outer loop was used for sections, and the inner loop was used for leaves on the current section. If symmetric geometry is required, we would divide one section into two symmetric halves. We only construct the leaves on one half section, and then we used `G4ReflectionFactory::Place()` method to construct the other mirrored or reflected half section. An alternative method in constructing the multi-section wheel is using the `G4ReflectionFactory::Replicate()` method, in which several replicas are created from the original section. However, the particle tracks will get stuck in these replicas during the tracking process, and the reason is not clear so far. We abandoned this replicate method finally but used the construction loop method instead.

We defined a UI command to control the number of sections and another UI command to set the indicator to build the symmetric half section or not. These two commands are invoked after the application has been compiled and linked, so it is very convenient for users even though the user does not have our source codes.

The geometry parameters including the number of leaves, the relative weight and thickness for each leaf designed using NEU were stored in an ASCII file, and we used file reading functions in C++ to read in the contents in this ASCII file as geometry

construction parameters. It is also very convenient for users because for different SOBPs settings, there is no need for users to edit the source code again and what they need to do is to provide another ASCII file containing geometry parameters for a new wheel to form another SOBPs curve.

The inner radius was set to 2 cm and the outer radius is set to 8 cm, so the width of the ring was 6 cm, which was wide enough to ensure all primary protons could hit it.

4.2.2 Construction of Second Scatterer

In S2, on the left of mating surface ($z = -240$ cm plane) is the inner-contoured compensation part made of low-Z material, e.g., Lexan, and on the right is the contoured scatterer made of high-Z material, e.g., lead. We also put a brass collimator outside the compensation part to limit the beam lateral profile.

The range compensation part is an inner-Gaussian curve structure and the scattering part is an outer-Gaussian curve structure. Both of these can be constructed using the `G4Polycone()` method in Geant4. We still put the geometry parameters in an ASCII file and they are read in only when the application is running. It is also very convenient for users because if they want to construct a new S2 component, what they need to do is only provide a new ASCII file containing new parameters without modifying any source codes of the application.

The parameters of S2 (250 MeV, large field, 10 cm SOBPs) produced from NEU are listed in Table 4-4. The second scatter is shown in Figure 4-7.

Table 4-4. Parameters of S2 from NEU

Radius (cm)	Thickness (cm)	
	Lexan	Lead
0	0.1002	0.8731
0.5331	0.4135	0.811
1.0662	1.2238	0.6505
1.5993	2.2867	0.4397
2.1324	3.3258	0.2334
2.6655	4.071	0.0853
3.1986	4.4633	0.0073
3.7317	4.5001	0
4.2648	4.5001	0
4.7979	4.5001	0

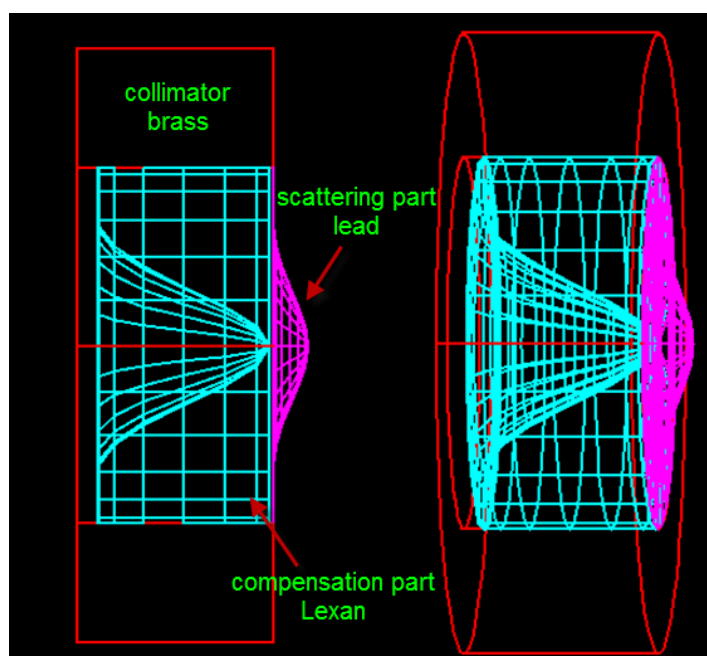


Figure 4-7. Gaussian Shaped Bi-Material Second Scatterer

The center coordinates of S1 are (-5 cm, 0 cm, -290 cm). The center coordinates of S2 are (0 cm, 0 cm, -240 cm). The relative relation of center positions of S1 and S2 are shown in Figure 4-8. After the primary beam passes through the S1, it will hit S2.

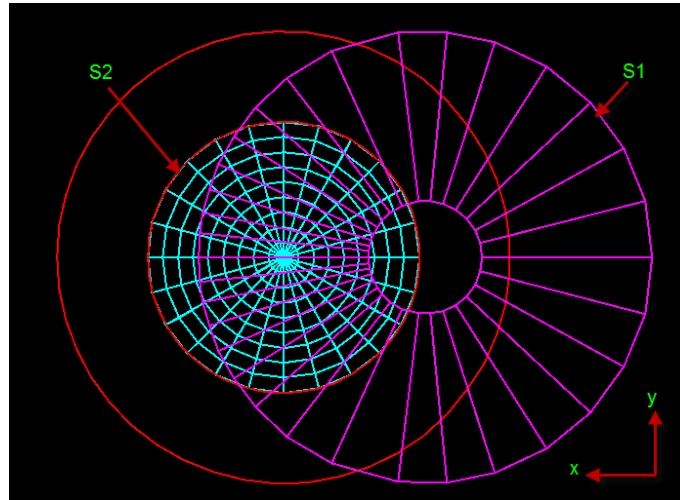


Figure 4-8. The Relative Relation of Center Positions of S1 and S2

4.2.3 Construction of Range Compensator

The structure of the nozzle closest to the dose scoring volume is the range compensator. It is a patient-specific structure, because its shape and thickness depend on the tumor location, size and profile. If we assume the tumor is a sphere, the inner structure of compensator would be a half sphere. A compensator used in this research is shown in Figure 4-9, which was built using a Boolean operation of a box and a half sphere. Actually, a range shifter (usually a plastic plate) in the nozzle is also required in a nozzle, which is used to shift the SOBP location in the dose scoring volume. If only a

spherical tumor is assumed, we can also adjust the thickness of the compensator to shift the location of SOBP into the dose scoring volume instead of using the range shifter. But in some cases, a plate or a wedge shifter is needed.

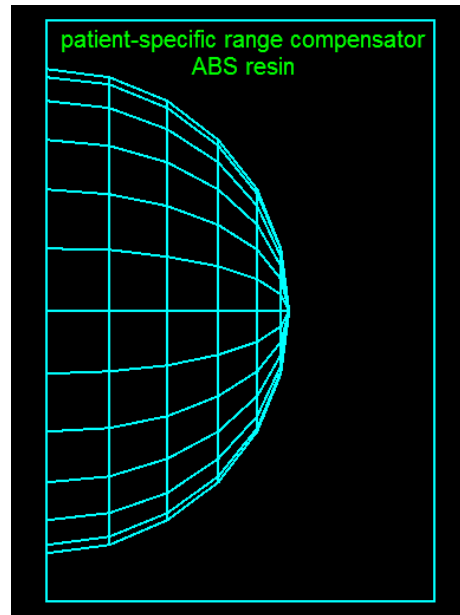


Figure 4-9. Patient-Specific Range Compensator

4.2.4 Construction of Other Components

The shielding shell, collimators and snout are ring structures. A ring can be built using G4Tubs class. The inner profile of the final aperture should be same as (or larger than) the transversal profile of the tumor. Because a spherical tumor is assumed, the inner profile of the final aperture is a circle. The final aperture is also a ring in this research. A multi-leaf collimator is usually used in clinical treatment as the final aperture. A multi-leaf collimator is shown in Figure 4-10.

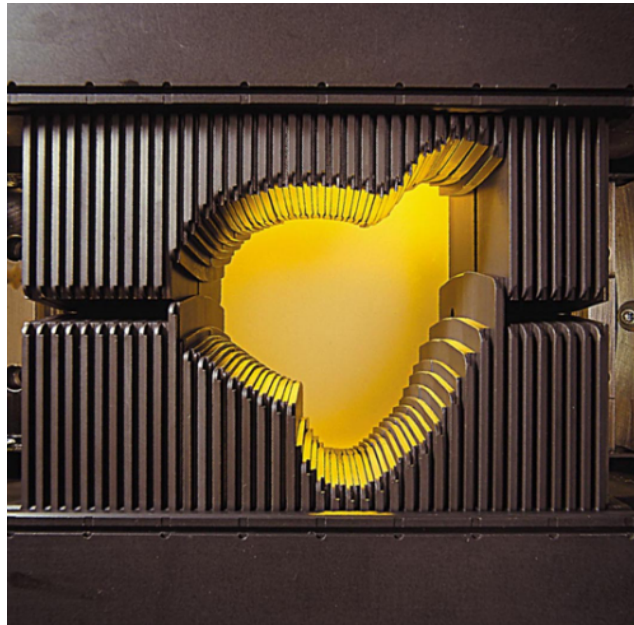


Figure 4-10. A Varian Multi-Leaf Collimator (Varian Medical Systems Newsroom 2012)

4.2.5 Construction of a Patient Phantom

As mentioned above, a series of DICOM images from CT scanning were used to construct a patient phantom in this research. Not all the CT slices were needed, and only the slices containing the whole tumor region and several extended slices were used to construct the patient.

A set of DICOM images from a patient with prostate cancer were obtained freely from <http://pubimage.hcuge.ch:8080/>. The whole-body CT images, PET images and PET-CT fusion images are included in the dataset.

The coronal view of CT, PET and PET-CT fusion images of the patient are shown in Figure 4-11, on which only the slices containing the bladder and prostate and neighbors are plotted. The CT slices were used to construct the patient geometry in a

Geant4 application. The profile of the prostate cancer cannot be seen clearly in the CT slices due to the lack of soft-tissue contrast resolution (Schoder and Larson 2004). PET images can be used to find the profile of the prostate cancer, but the resolution of PET images is relative low to make it hard to exactly delineate the profiles of tumor and its surrounding tissues. The PET-CT fusion images can overcome these difficulties. They are used to localize the profile of the tumor and differentiate it with its surrounding tissues. On the CT image, the color stands for the value of CT number. On the PET image, the color stands for the concentration of radioactive nuclides in each pixel. The PET-CT fusion image is the co-registration of the CT image and the PET image, so strictly speaking, the color does not stand for CT number or the concentration of the radioactive nuclides, but we can roughly think the red color stands for the maximum intensity and the yellow is second because the color bar was specified by us. We can see strong intensities in the bladder and the reason will be explained below.

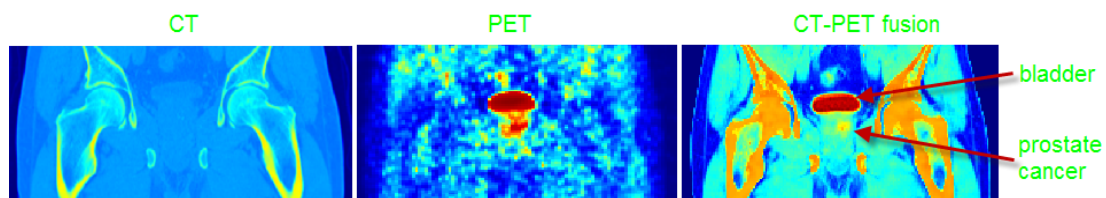


Figure 4-11. Coronal View of CT, PET and PET-CT Fusion Images of the Patient

The patient was injected with F18-fluorocholine (fluoromethyl-dimethyl-2-hydroxyethylammonium, abbreviated as FCH) as radio-tracers before PET imaging. Choline is a necessary matter for the synthesis of the phospholipids in the cell

membranes (Schoder and Larson 2004). One main metabolism process of choline is phosphorylation which is catalyzed by choline kinase (Roivainen et al. 2000). The metabolism and synthesis processes are more active in cancer cells, so there will be an increased uptake of choline in them. F18-labeled choline has a similar metabolism pathway as the normal choline, so this fluorocholine also will be accumulated in cancer cells. F18 will decay to O18 via β^+ decay or EC (electron capture) with a half-life of 109 minutes. The released positron will annihilate later with an electron and the two newly-produced 511 keV gammas have chances to be detected coincidentally on the ring detector around the patient. The location of the annihilation event will be recorded so that the profile of the organs or tissues which accumulate high-concentration radiotracers will be imaged. Due to the high-concentration of the radio-tracers in the tumor cells, the intensity in them will be large in the PET image (Schoder and Larson 2004) to make them be found easily. FCH will be rapidly cleared from the blood after injection to vein. The tracers will be accumulated in salivary glands, lung, liver, kidneys, and adrenal glands, so these organs will be shown clearly in FCH PET images. FCH will also appear in the bladder in 3 to 5 minutes after injection because it will be excreted via urine (Schoder and Larson 2004). This explains why we can see a clear profile of bladder in the FCH PET images. The distribution of the radio-tracers will be heterogeneous over the two lobes of the prostate for prostate cancer, but for benign prostate hyperplasia, the radioactivity is lower and distributed uniformly (Hara 2001). The bladder and the prostate tumor are marked in the PET-CT fusion image in Figure 4-11. The whole prostate gland and base of the bladder were selected as the gross tumor volume (GTV)

based on the PET images. To make the GTV fully covered by the high-dose region, the CTV should be larger than GTV. To simplify the problem, we assumed the CTV was a sphere with a radius of 3 cm. The axial, sagittal and coronal views of CT images are shown in Figure 4-12, Figure 4-13 and Figure 4-14. The spherical CTV is marked on these images with an estimated radius of 3 cm.

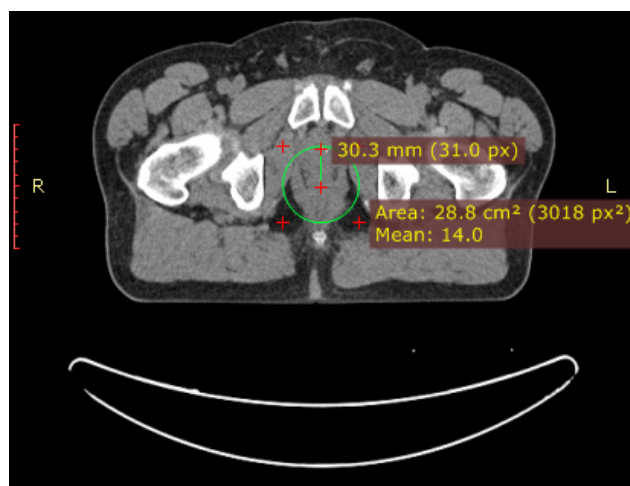


Figure 4-12. Axial View of CT Image of the Patient (slice 60/120)

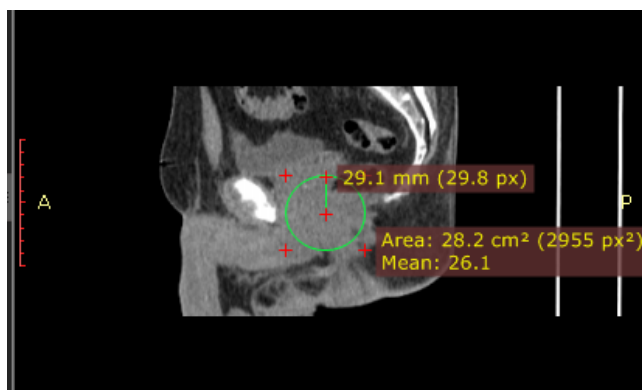


Figure 4-13. Saggital View of CT Image of the Patient (slice 257/512)

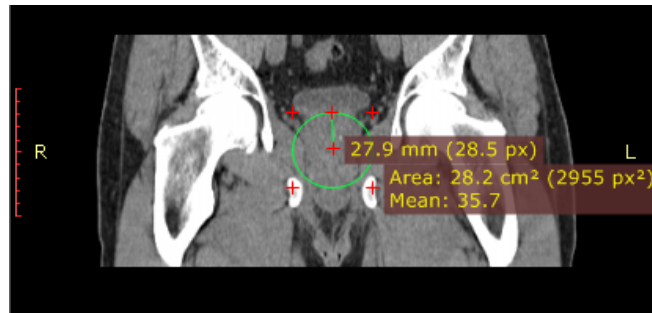


Figure 4-14. Coronal View of CT Image of the Patient (slice 232/512)

When the size and the location of the CTV were determined from the PET-CT fusion images, we could use the CT images from the same patient to construct voxel geometry in Geant4. The conversion process has been introduced in section 3.6.

Not all the CT slices for this patient were used to build the voxel geometry in this case, and only 120 slices containing the bladder and prostate cancer were used. Each slice has a dimension of 50 cm \times 50 cm (512 \times 512 pixels), and a thickness of 1.5 mm. Each slice was compressed to 64 \times 64 pixels by a factor of 8 and four consecutive slices were merged into one layer. The final number of voxels is 64 \times 64 \times 30 and each voxel has a size of 7.8125 mm \times 7.8125 mm \times 6 mm.

4.3 Primary Proton Source Settings

The proton beam source was set using the UI commands of the G4GeneralParticleSource class. We put all the source definition commands in a macro file, which would be invoked when the application was executed. The parameters were recommended by Paganetti (Paganetti et al. 2004). The proton beam energy was sampled from a Gaussian distribution with mean energy of 250 MeV and standard deviation of

2.5 MeV. The proton beam spatial position was sampled on a z-plane (initially, $z = -300$ cm) with both of x and y standard deviation of 0.65 cm. As to the beam momentum direction (flying direction), we should consider both the polar angle and azimuthal angle. The azimuthal angle (the angle between the projection vector of beam momentum direction on x-y plane and x-axis) was uniformly sampled from 0 degrees to 360 degrees. The polar angle (the angle between the beam momentum direction and z-axis) was sampled from a half Gaussian distribution with a center angle of 0 degree (along the positive direction of z-axis) and a dispersion of 0.183 degrees (the standard deviation on a whole Gaussian distribution).

When the nozzle rotated to a new angle with the patient voxel geometry, the source sampling plane was the nozzle geometry coordinate z-plane and initial beam direction was the positive direction of the nozzle geometry z-axis.

The primary source position, direction and energy distribution curves will be shown in section 5.2.

4.4 Physics Settings

As mentioned above, the recommended physics settings for proton beam therapy include standard electromagnetic physics and hadronic physics.

The EM physics processes registered for protons include multiple scattering (small-angle elastic deflection of charged particles due to the Coulomb force with nuclei of the medium), ionization, bremsstrahlung and pair production (electron and positron pair). For photons, the EM processes include photoelectric effect, Compton scattering and gamma conversion (pair production mainly). For electrons, the EM processes

include multiple scattering, ionization and bremsstrahlung. For positrons, besides the same EM processes for electrons, the annihilation process is also included. For ions, the EM processes include ionization and multiple scattering. The registered EM processes for this application can be listed by invoking UI command “/process/list Electromagnetic.”

The physics processes of neutron belong to the category of hadronic physics. The hadronic physics processed for neutrons include elastic scattering, inelastic scattering, fission and neutron capture. For protons, the hadronic physics processes include elastic scattering and inelastic scattering.

As mentioned above, we used the QGSP_BERT package as our physics list. More physics processes for other particles are also included in this package, but they will not be discussed here.

We also defined a new process (not a real physics process but is treated as a physics process without interaction) from G4StepLimiter class for charged particles like protons, electrons and positrons. The purpose was to limit the step length when tracking charged particles. To make this process effective in a logical volume, we must invoke the SetUserLimits() method for the specified logical volume and register this physics constructor to the concrete object of QGSP_BERT package by invoking the RegisterPhysics() method.

The range cut is set to 0.7 mm for protons, electrons, positrons and gamma rays in the QGSP_BERT package.

4.5 Data Analysis Using Root

We defined one energy deposition scorer class derived from G4PSEnergyDeposit class to score the energy deposition in water phantom or patient voxel geometry. A root file containing a tree with several branches was used to score the information of energy deposition points in the water phantom or patient voxel geometry.

The information for each energy deposition point included the x, y and z coordinates, total energy deposition in one step, the particle name and particle ID.

Based on the physics settings discussed above, we know the particles contributing to the energy deposition in the scoring volume including primary protons, secondary neutrons, secondary protons, electrons, positrons, gammas and recoil nuclei. For the clinical proton beam with a high-energy such as 250 MeV, secondary neutrons play an important role because of the biological effects of neutrons.

We divided the source for the total energy deposition into three categories, which are primary protons, secondary neutrons and secondary particles of secondary neutrons, and other particles.

Protons from the particle source were treated as primary protons with a particle ID equal to 1.

Energy deposition (or dose) from neutrons is due essentially to the energy from neutron secondary particles, such as recoil protons, carbon ions and oxygen ions. In this research, we defined a name for neutrons and neutron secondary particles called “neutron_relatives” with a particle ID equal to 2. The energy deposition from any neutron_relatives was considered to be the energy deposition from a neutron.

All the other particles were treated as “others” with a particle ID equal to 3.

In some Geant4 examples, the developers simply used a particle name filter to obtain the energy deposition contribution from the corresponding particle. However, this approach is not correct. For photons or neutrons, most (not all) of the energy depositions in a medium are from their secondary particles. If this particle name filter is used, the energy deposition obtained from photons and neutrons is close to zero.

We should assign a common attribute to all neutron relatives, not limited to one particle track name. We defined a class derived from G4VUserTrackInformation and another class derived from G4UserTrackingAction. In the tracking action class PreUserTrackingAction() method, we assigned a neutron track with user track information, and in the PostUserTrackingAction() method, this neutron secondary particles are assigned the same user track information. By setting these, all the neutron relatives have the same user track information as their common attribute. When we score energy deposition using our defined scorer, if the track owns this common attribute, its energy deposition is counted to the neutron relatives.

A track object in Geant4 has a member called parent track ID which stands for the “mother track” ID of this track. For a primary particle track, its parent ID is 0. This can be an indicator for judging if a track is a primary particle track or not.

Excluding the primary protons and neutron relatives, energy from any other particles are counted to “others.”

A common energy deposition scoring method is to divide the scoring volume such as a big water box, into a number of regular small cells and score energy deposition

in each small cell. This method increases the geometry construction time and the simulation time. Our method was only building a big water box but not dividing it into small cells. Because there was no geometry boundary limiting the step length of a track in the scoring volume, the precision of determining the energy deposition point might be not good enough to obtain a smooth energy deposition curve. We set a small step limit for this scoring volume to limit the step length of each track (actually only for protons, electrons and positrons as mentioned above, because they have continuous-energy loss during tracking), so the determination of energy deposition point position would be accurate. We tried several different limit values and finally we found 4 mm was a reasonable and acceptable value to obtain a smooth energy deposition curve with a good precision.

We defined a class called plane scorer derived from G4PSFlatSurfaceCurrent class to monitor the particle beam information after the first scatterer, after the second scatter and on the front surface of dose scoring volume. The monitored beam information included the particle type, particle energy spectrum and lateral beam profile.

5. SIMULATION RESULTS

In this section, we will provide the visualization of geometry and trajectories, and plots of simulation results from different physics or geometry settings. Our whole simulation procedure was in the order from easy to complex settings. The scoring volume was simply a water box for most cases. Finally, a patient voxel geometry containing a prostate cancer was used as the dose scoring volume.

If the dose scoring volume is a uniform water phantom, the shape of spatial dose distribution curves will be same as the shape of the energy deposition distribution curve. Below we only provide the energy deposition distribution if the dose scoring volume is water phantom. If the scoring volume is the patient voxel geometry, we will provide dose result in each voxel.

At first, we will provide some simple simulation results to show the effects from different physics settings. Then, we will provide the distribution plots of the primary source protons.

Most of the results were analyzed and plotted using root. Several other results were plotted using other software such as SimpleGeo (Theis et al. 2006). If not specified, the value in all the plots about energy deposition distribution is in the unit of MeV.

The component settings for different cases are listed in Table 5-1.

Table 5-1. Component Settings for Different Simulation Cases

Component	Material	Geometry case No.					
		1	2	3	4	5	6
Scatterer disc	Lead		Yes	Yes			
S1	Lead, Lexan				Yes	Yes	Yes
S2	Lead, Lexan			Yes	Yes	Yes	Yes
Long shielding shell	Brass				Yes		
Short shielding shell	Brass					Yes	Yes
Collimators	Brass					Yes	Yes
Snout	Brass					Yes	Yes
Final aperture	Brass					Yes	Yes
Inner spherical compensator	ABS resin					Yes	
Plate range shifter	ABS resin						Yes
Wedge compensator	ABS resin						Yes
1 st plane scorer, z = -280.05 cm	Air		Yes	Yes			
2 nd plane scorer, z = -230.05 cm	Air		Yes	Yes			
3 rd plane scorer, z = -1.05 cm	Air	Yes	Yes	Yes	Yes	Yes	Yes
Dose scoring volume	Water	Yes	Yes	Yes	Yes	Yes	
Patient voxel geometry	Patient						Yes

5.1 Effect of Multiple Scattering of Protons

The proton beam can be broadened laterally due to the multiple scattering physics process of proton elastic Coulomb scattering with the nuclei of the medium. Hence, this effect can influence the profile of the spatial energy deposition.

We can use the UI command “/process/inactivate msc all” to close the multiple scattering process for all particles. To simplify the problem, only electromagnetic physics processes were included in this example. The comparison of ten primary proton trajectories in the water phantom with and without the multiple scattering process is shown in Figure 5-1. The primary source was point source moving along z-axis. Only proton trajectories are shown by setting proton in the particle name filter to show

trajectories. The effect of multiple scattering is very obvious in Figure 5-1. The ending profile of the beam is broadened from the beginning profile.

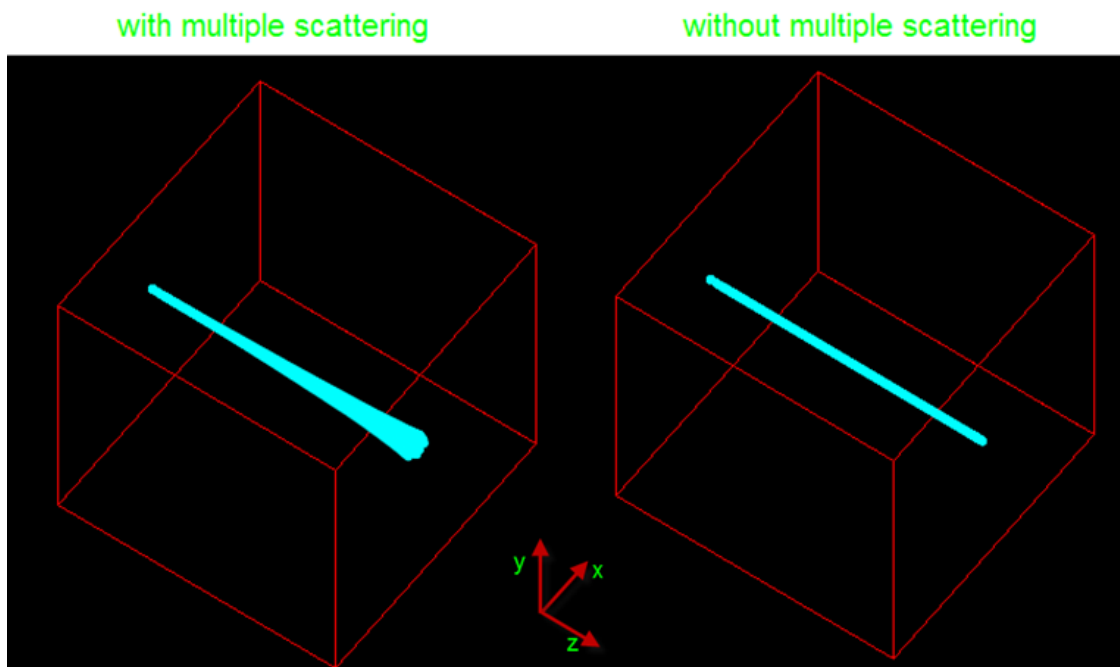


Figure 5-1. Comparison of Proton Trajectories with and without Multiple Scattering

5.2 EM Physics and Hadronic Physics

As mentioned above, the EM physics for protons can only produce secondary particles such as gamma rays and electrons. Hadronic physics can produce neutrons and other recoil nuclei (gamma rays can also be produced from hadronic physics processes). The comparison of trajectories produced from ten primary protons interacting with water between the settings of EM physics and EM plus hadronic physics is shown in Figure 5-2. Electron trajectories are plotted in red; gamma ray trajectories are plotted in green;

proton trajectories are plotted in blue; neutron trajectories are plotted in yellow; positron trajectories are plotted in white; others are plotted in gray. If not specified explicitly, this trajectory showing strategy is applied in all cases. In Figure 5-2, only protons, gamma rays and electrons exist if only EM physics is used, and neutrons can be produced if hadronic physics is added.

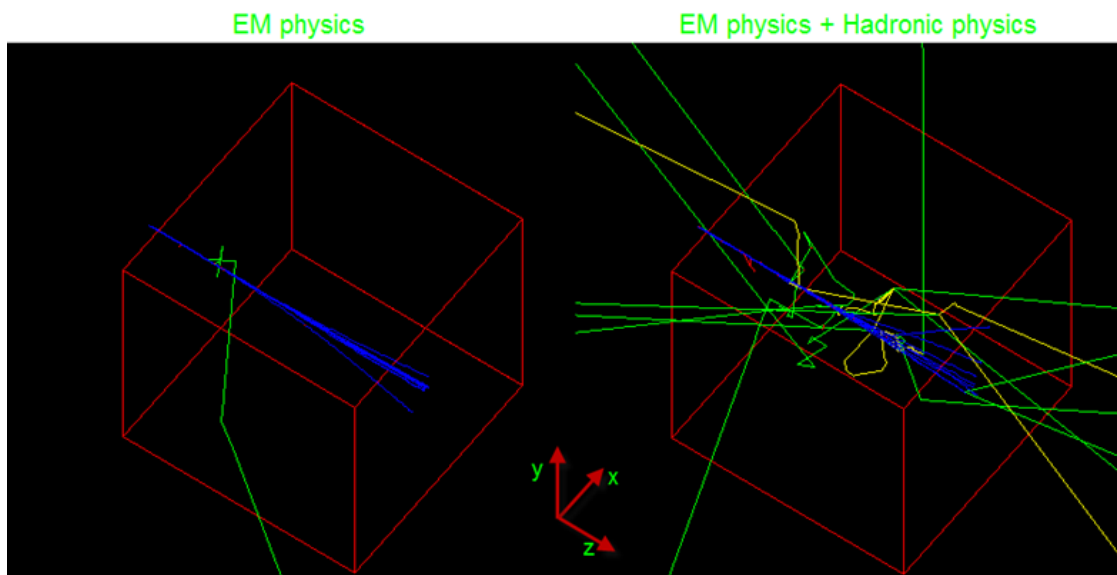


Figure 5-2. Trajectories Produced from Ten Primary Protons Interacting with Water

5.3 Primary Source Distributions

The primary proton source was sampled from the plane at $z = -300$ cm. Both x and y had center 0 and standard deviation equal to 0.65 cm. We used root to record one million primary source protons and the sample distributions are shown from Figure 5-3 to Figure 5-9. The value in each figure stands for the number of primary protons. Entries

stands for the total number of counts in each histogram. Mean stands for the expected value for each histogram. RMS (root mean square) stands for the standard deviation for each histogram. Figure 5-3, Figure 5-4 and Figure 5-5 show the sampled spatial distribution of primary source protons. The parameters in these plots show that they obey our specified distribution in section 4.3. Figure 5-6 shows the kinetic energy of primary protons obeys the Gaussian distribution with mean of 250 MeV and standard deviation of 2.5 MeV. Figure 5-7 shows the momentum direction polar angle distribution which is a half-Gaussian distribution with the maximum dispersion of 0.65 degree far away from z-axis. So, the beam can be treated as a very “straight” beam. Figure 5-8 shows the momentum azimuthal angle distribution which is a uniform distribution from 0 to 360 degrees. The extension of particle position on x-axis or y-axis is less than 6 cm in Figure 5-9, so the 6-cm radial width of the S1 set in section 4.2.1 is wide enough to guarantee that all primary particles can hit S1.

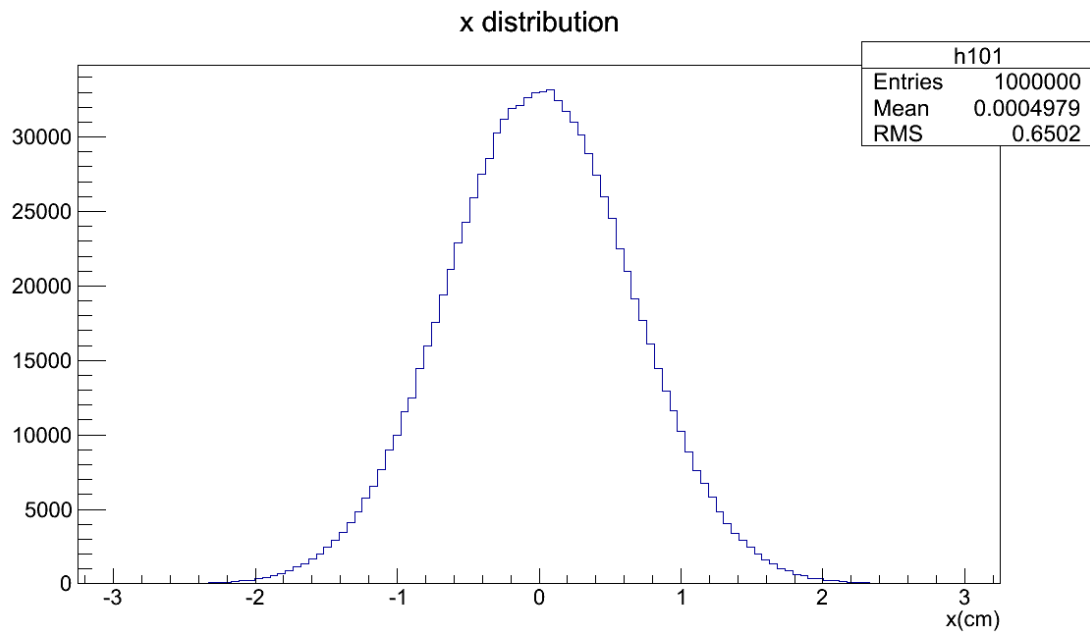


Figure 5-3. The Distribution of the x-Coordinate of the Primary Proton Source

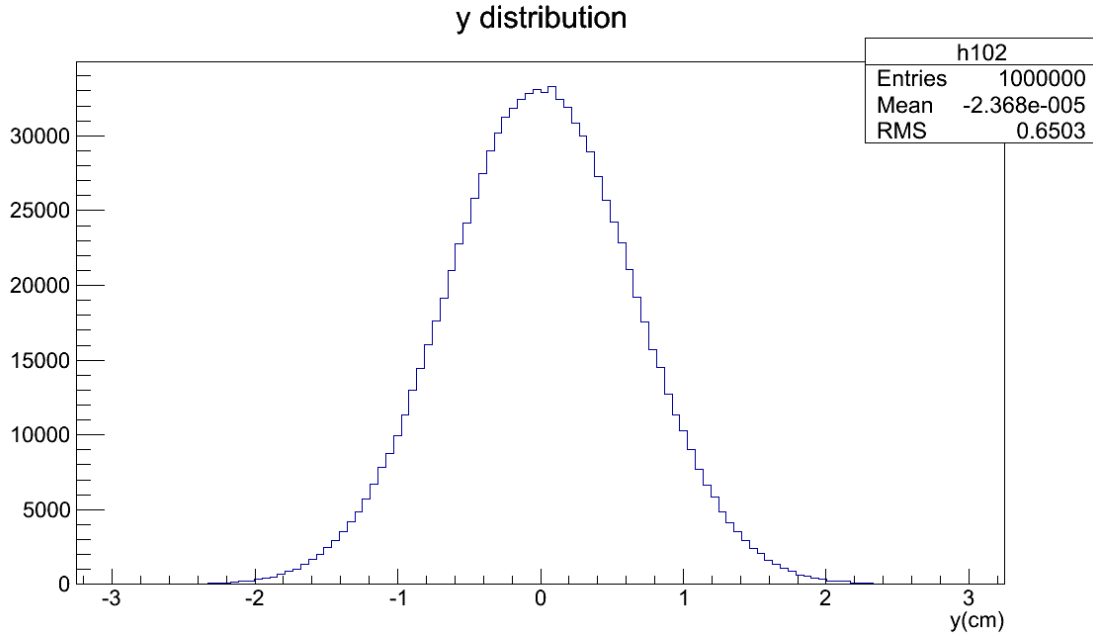


Figure 5-4. The Distribution of the y-Coordinate of the Primary Proton Source

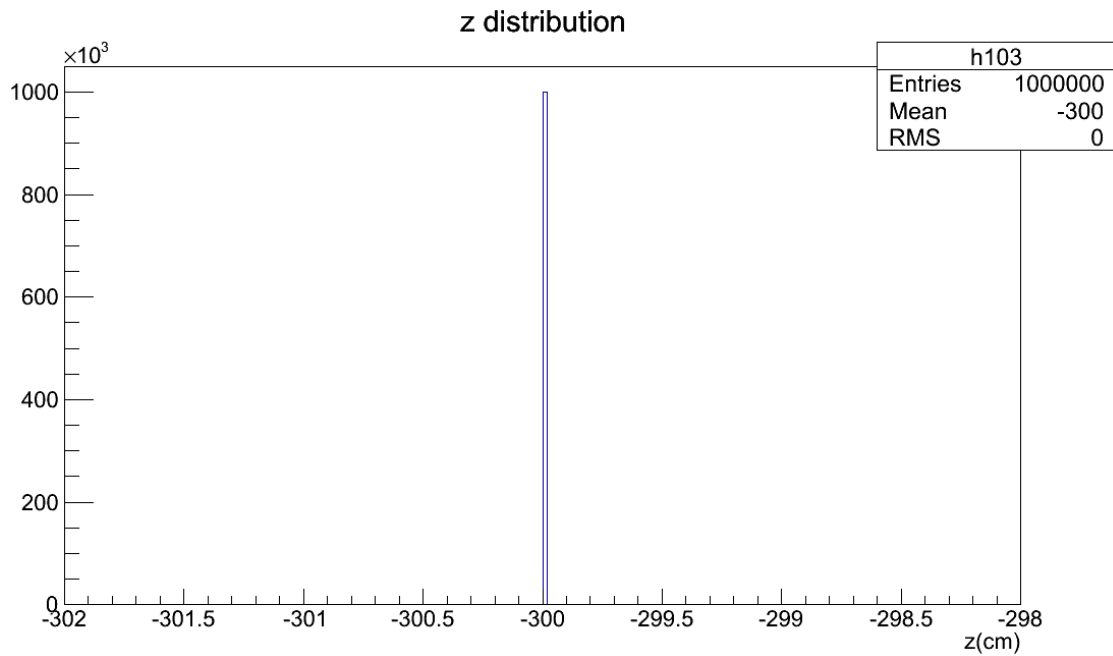


Figure 5-5. The Distribution of the z-Coordinate of the Primary Proton Source

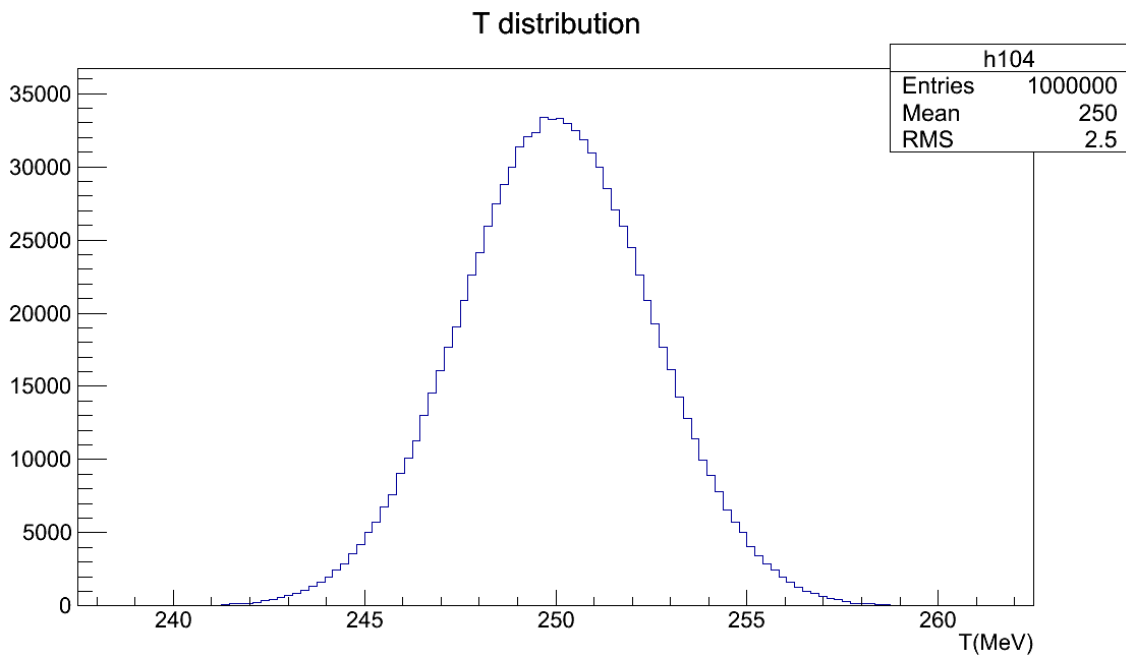


Figure 5-6. The Distribution of the Kinetic Energy of the Primary Proton Source

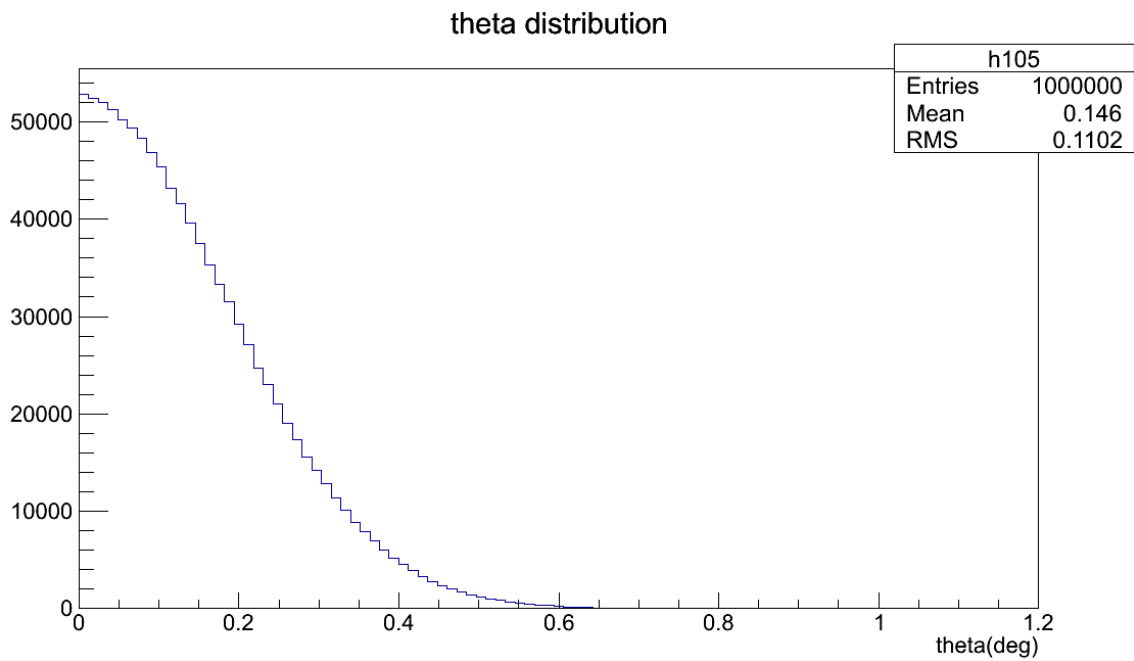


Figure 5-7. The Distribution of the Polar Angle of the Primary Proton Source

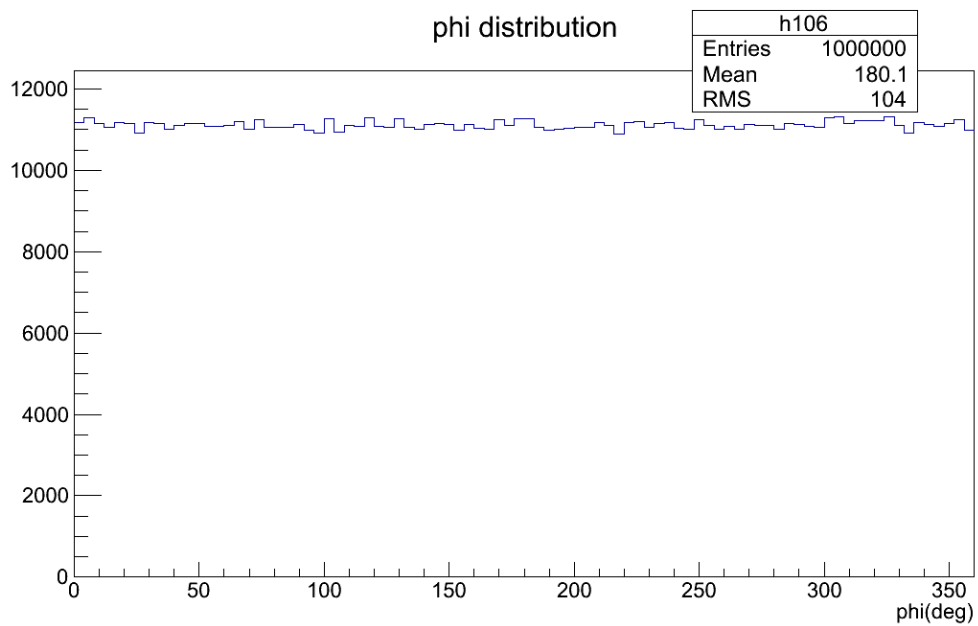


Figure 5-8. The Distribution of the Azimuthal Angle of the Primary Proton Source

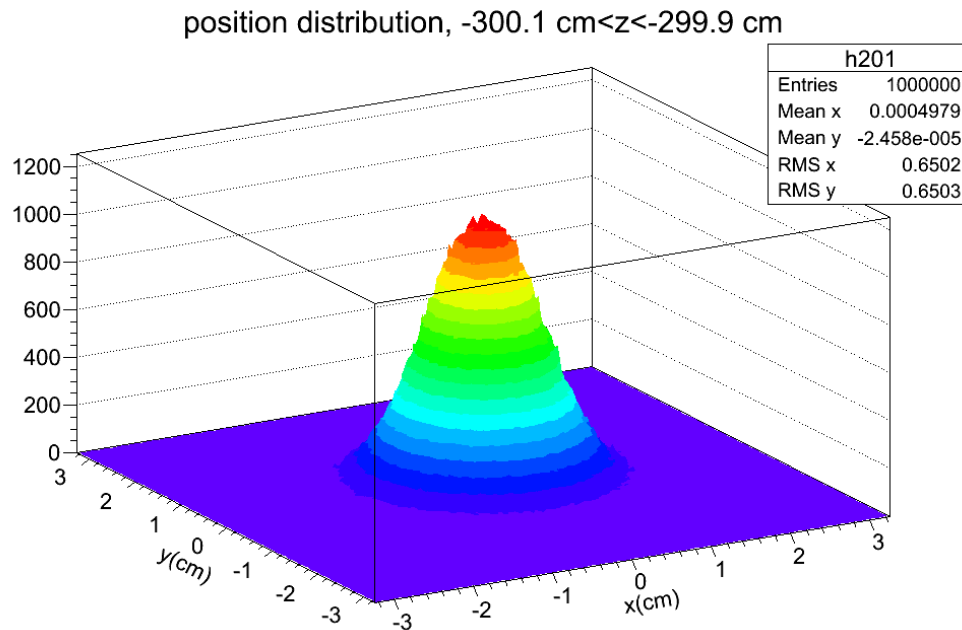


Figure 5-9. Primary Proton Position Distribution on the Plane $z = -300$ cm

5.4 Results for Geometry Case No. 1

The primary proton source was distributed on the plane $z = -10$ cm. Other parameters were the same as in section 5.2. NPS was set to one million. The geometry and all particle trajectories (ten primary protons and their secondary particles) are shown in Figure 5-10.

The energy deposition along the z-axis in the water phantom is shown in Figure 5-11. There are 100 bins from $z = 0$ cm to $z = 40$ cm, so each bin width is 4 mm. The total kinetic energy of one million primary protons is $250 \text{ MeV} \times 1 \times 10^6$ equal to 2.5×10^8 MeV, so the total energy deposition in the water box should be less than this total kinetic energy.

The total energy deposition is mainly due to primary protons. The contribution from neutron relatives is too low to see on the linear-scale plot. The plot on a log-scale is shown in Figure 5-12. The integral is the energy deposition for each histogram. The total energy deposition is 2.221×10^8 MeV (less than the total kinetic energy). The energy deposition from primary protons is 1.927×10^8 MeV, contributing 86.76% to the total energy deposition. The energy deposition from neutron relatives is 1.05×10^6 MeV, contributing 0.47% to the total energy deposition. The energy deposition from other particles is 2.837×10^7 MeV, contributing 12.77% to the total energy deposition.

The planar energy deposition distribution on the plane $y = 0$ cm is shown in Figure 5-13. The energy deposition on the plane with the Bragg peak is shown in Figure 5-14. The Bragg peak position is in the bin between 36.8 and 37.2 cm. The lateral spreading of the energy deposition profile can be seen in these two figures due to the effect of multiple scattering.

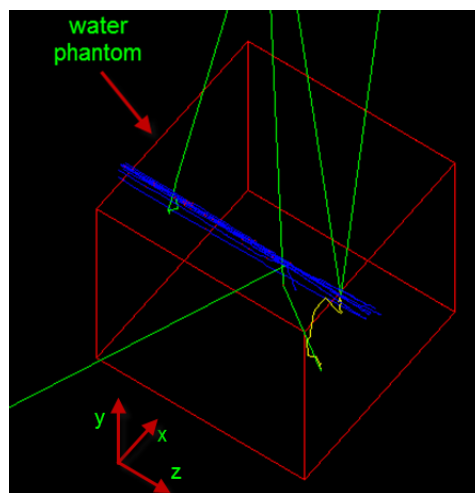


Figure 5-10. Geometry and Trajectories for Case No. 1

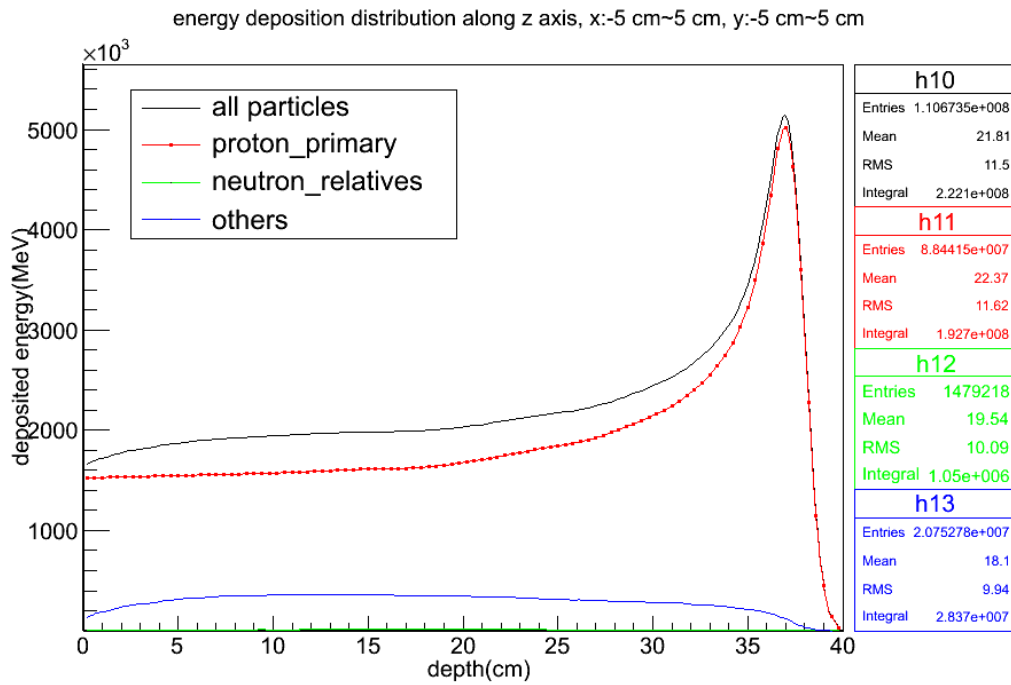


Figure 5-11. Energy Deposition along z-Axis on a Linear-Scale

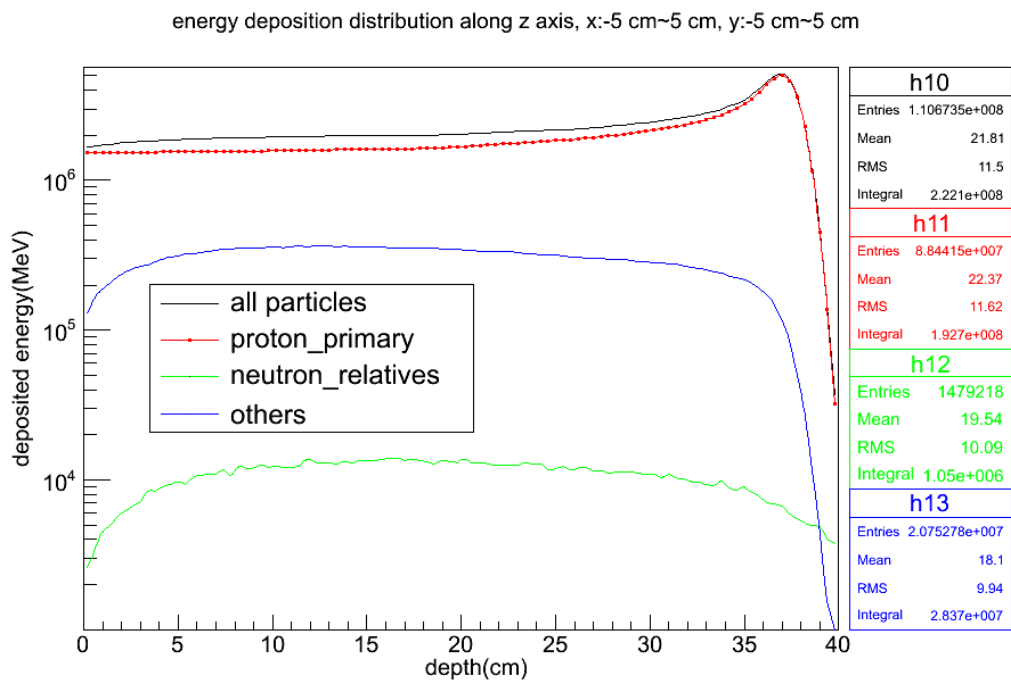


Figure 5-12. Energy Deposition along z-Axis on a Log-Scale

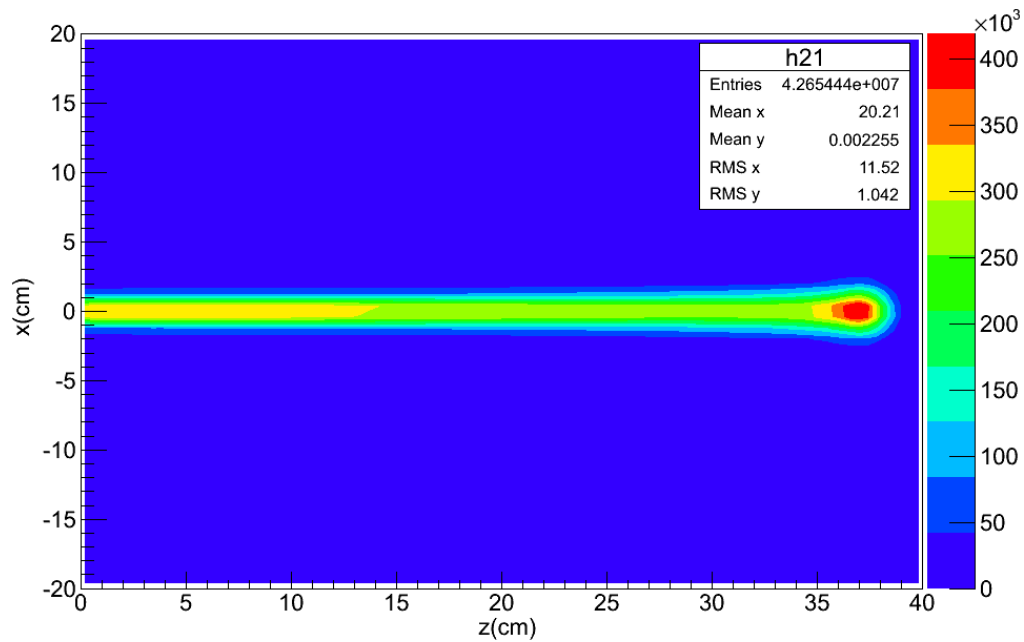


Figure 5-13. Energy Deposition Distribution on the Plane $y = 0$ cm

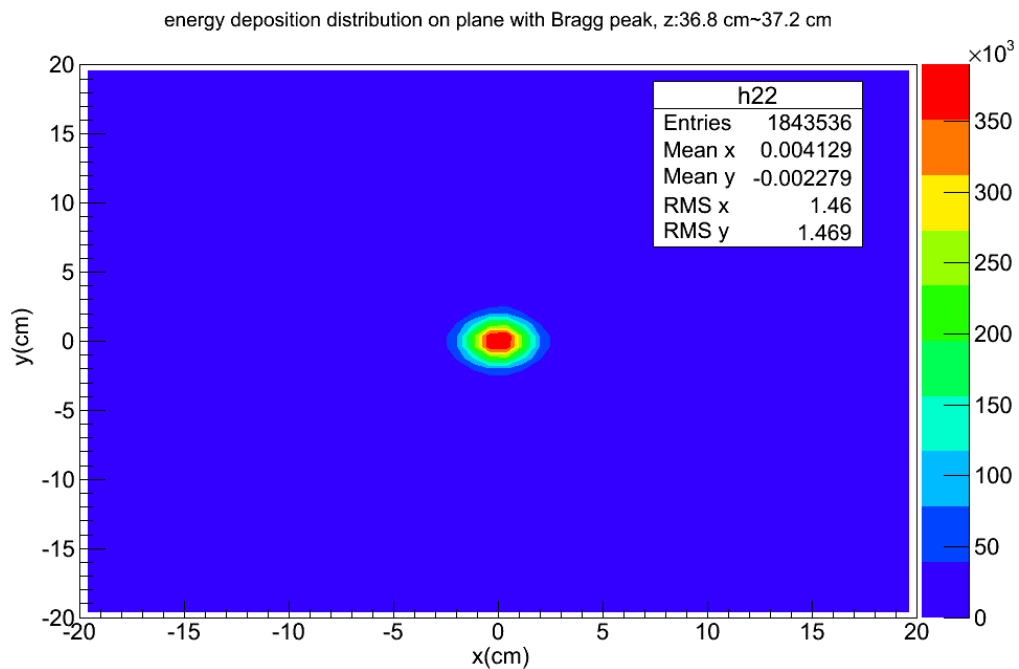


Figure 5-14. Energy Deposition Distribution on the z-Plane with the Bragg Peak

5.5 Results for Geometry Case No. 2

The purpose of Case No. 2 was to study the scattering effect of a single scatterer. Here we used a disc made of lead with a thickness of 0.883 cm and a radius of 10 cm. The scatterer center was at 0 cm, 0 cm, -290 cm. The geometry and all particle trajectories from ten primary protons are shown in Figure 5-15. Three plane-scorers were used to score particle information mainly the direction and position distribution (particle intensity). The first plane was used to score the beam attributes after the exit surface of the brass-disc scatterer. The second plane was 50 cm away from the first plane only to show a transition variation of the beam profile along the beam path. The third plane was close to the front surface of the water phantom and it was used to evaluate the beam attributes entering the water phantom.

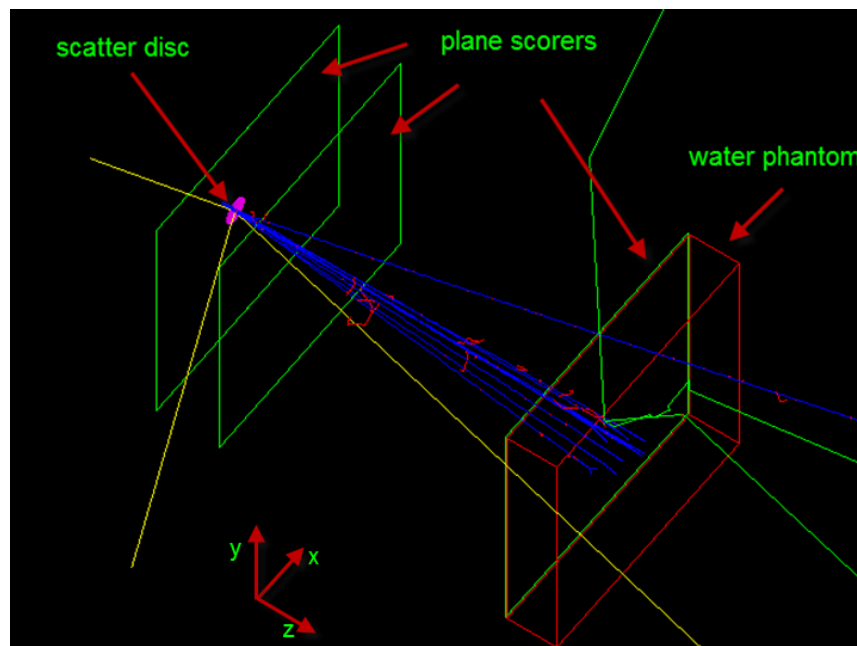


Figure 5-15. Geometry and Trajectories for Case No. 2

One million primary protons with the settings in section 4.3 were simulated in case No. 2. The primary proton information scored by the three plane scorers are plotted below. The kinetic energy distributions of primary protons on these three plane scorers are shown in Figure 5-16, Figure 5-17 and Figure 5-18. The mean kinetic energy of the beam is decreased to about 230 MeV mainly due to the energy loss in the brass-disc scatterer. Only the results of primary protons are provided, and results for neutrons and other particles are not provided because the purpose of this case was only to show the scattering effect of the brass-disc scatterer to the initial proton beam.

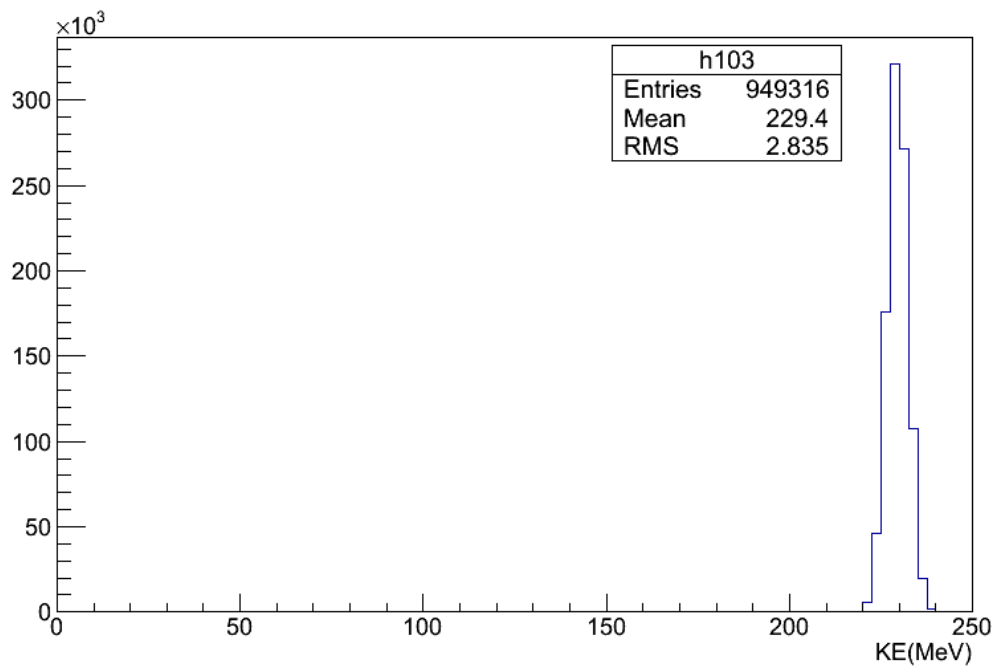


Figure 5-16. Kinetic Energy Distribution of the Primary Protons on the Plane $z = -280.05$ cm

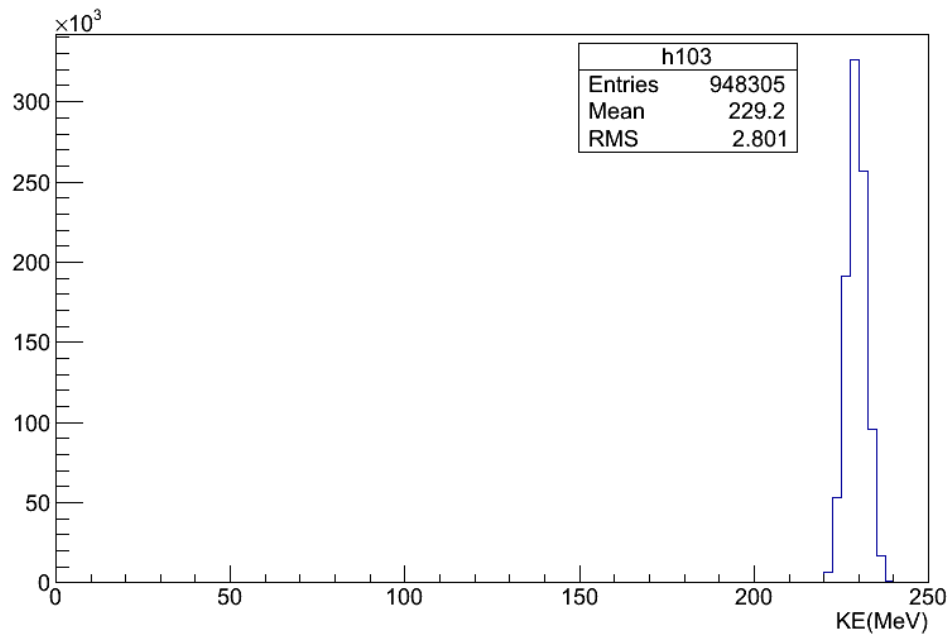


Figure 5-17. Kinetic Energy Distribution of the Primary Protons on the Plane $z = -230.05$ cm

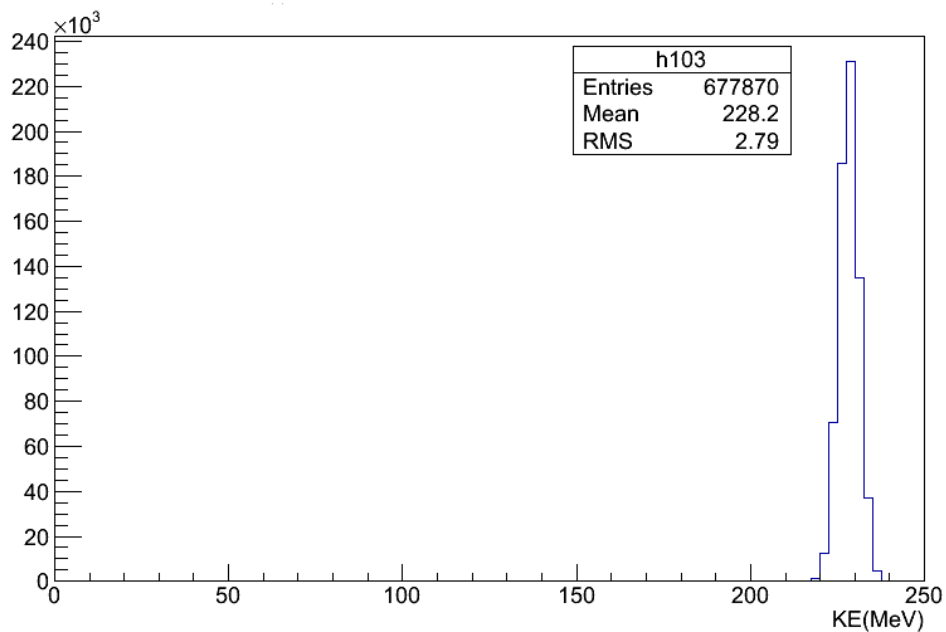


Figure 5-18. Kinetic Energy Distribution of the Primary Protons on the Plane $z = -1.05$ cm

The polar angle of momentum direction distributions of the primary protons are shown in Figure 5-19, Figure 5-20 and Figure 5-21. The polar angle can stand for the scattering angle of proton beam by the brass-disc scatterer. The mean scattering polar angle is about 3.5 degrees with the maximum angle of about 20 degrees.

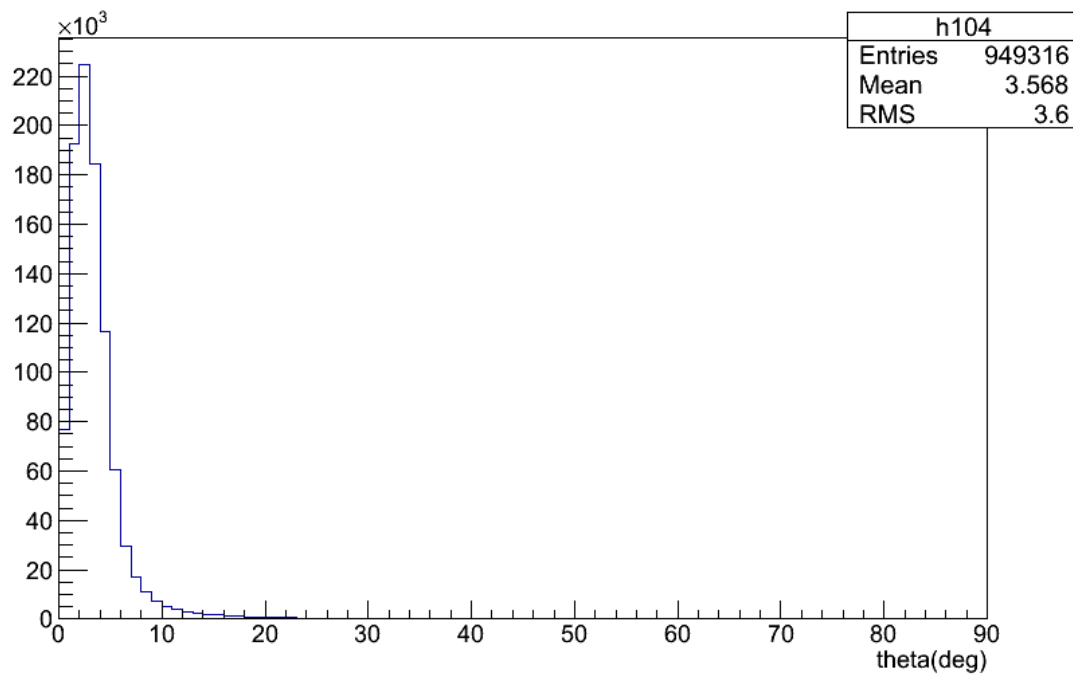


Figure 5-19. Polar Angle Distribution of the Primary Protons on the Plane $z = -280.05$ cm

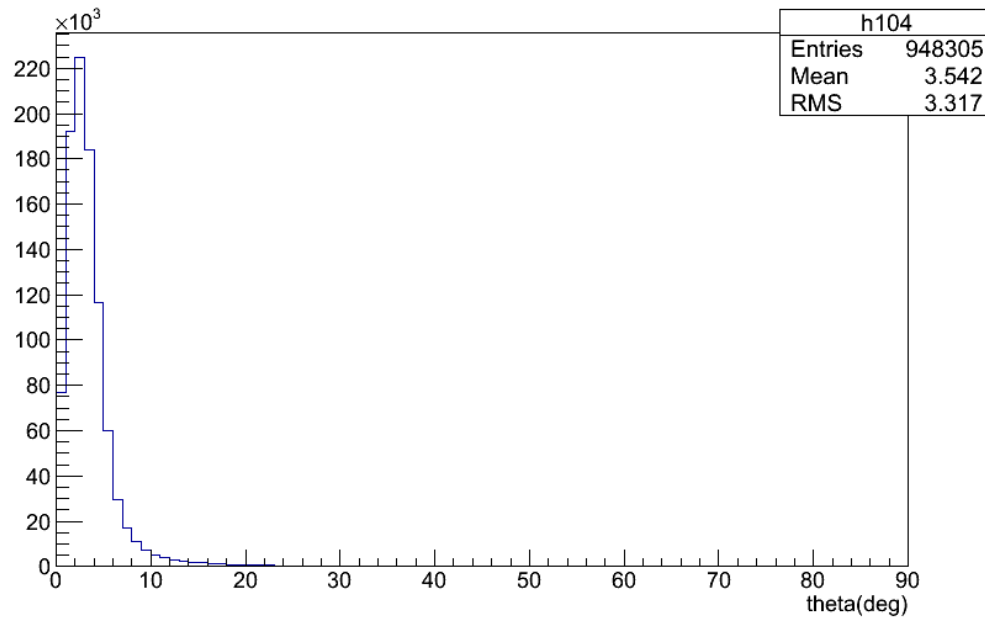


Figure 5-20. Polar Angle Distribution of the Primary Protons on the Plane $z = -230.05$ cm

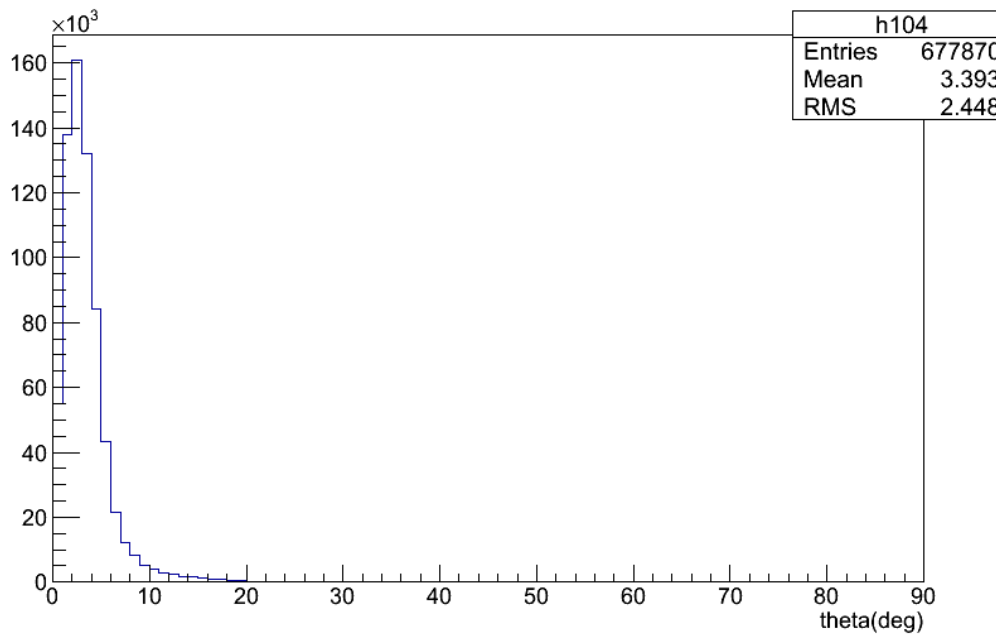


Figure 5-21. Polar Angle Distribution of the Primary Protons on the Plane $z = -1.05$ cm

The primary proton spatial position distributions on the three plane-scorers are shown in Figure 5-22, Figure 5-23 and Figure 5-24. The value in each bin of these three 2D histograms is the absolute number of primary protons in each small square on the plane. According to the definition of particle current, the value in each bin can be considered to be the primary proton current. These three scattering-point plots can only show the primary proton beam profiles roughly. Though the scattering angle is small (mean is about 3.5 degrees), the scattering effect is still very obvious after traveling a long distance (about 3 m). The proton beam radius can reach 40 cm on the final plane in Figure 5-24, but the current intensity is not uniform, which is revealed in Figure 5-25. The high-current beam radius is smaller than 10 cm and the standard deviation of x or y coordinates is about 15 cm.

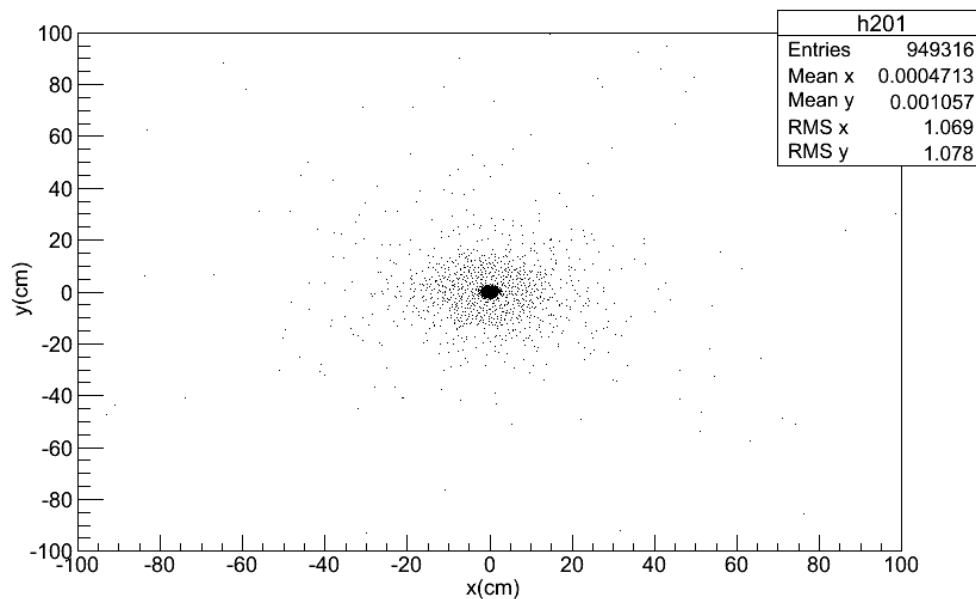


Figure 5-22. Particle Current Distribution of the Primary Protons on the Plane $z = -280.05$ cm

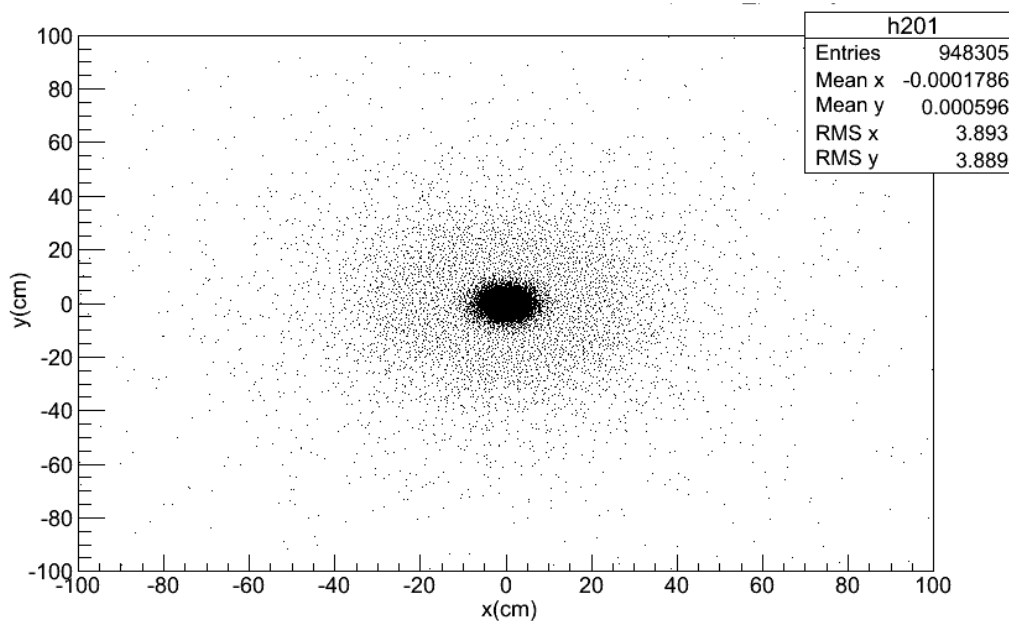


Figure 5-23. Particle Current Distribution of the Primary Protons on the Plane $z = -230.05$ cm

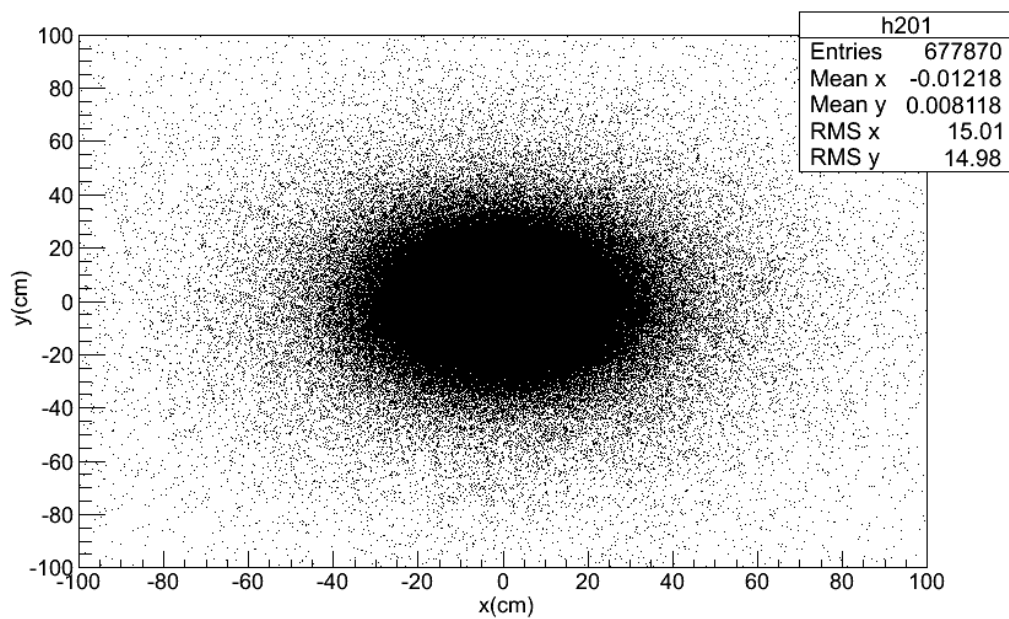


Figure 5-24. Particle Current Distribution of the Primary Protons on the Plane $z = -1.05$ cm

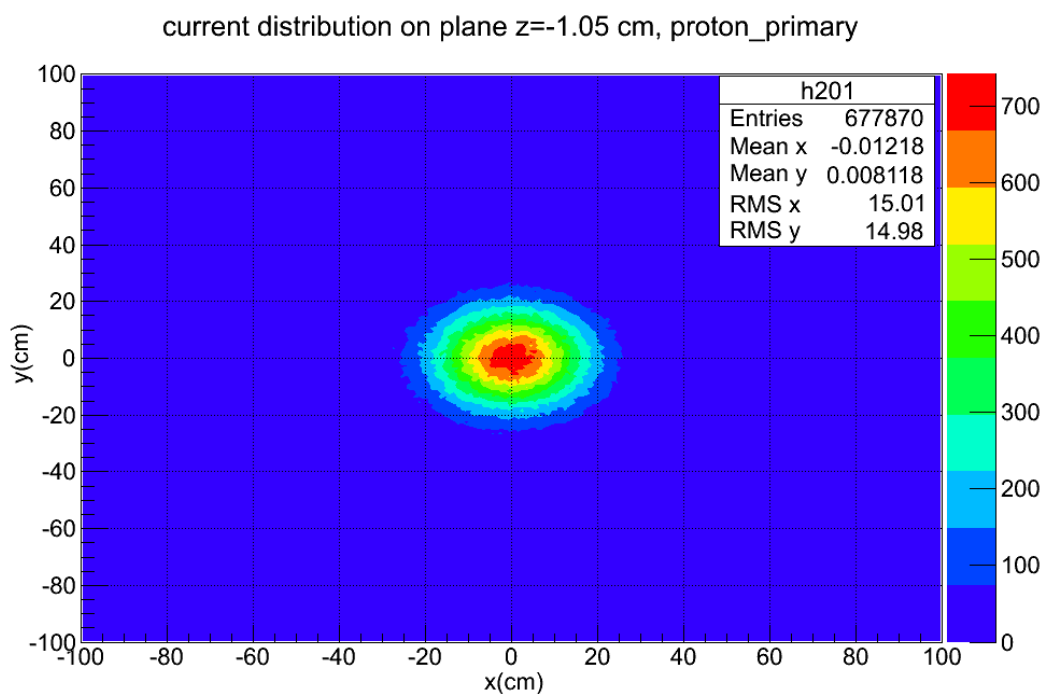


Figure 5-25. Particle Current Distribution of the Primary Protons on the Plane $z = -1.05$ cm in Color Contour

The depth-energy deposition curve is shown in Figure 5-26. The error bar option was chosen when plotting in root. But the standard error for each bin was too small to be seen. We enlarged this view, and the histogram between 36 cm to 40 cm is shown in Figure 5-27. The error was very small and the relative error was far less than 1%.

The x-y planar energy deposition distribution for all z-coordinates is shown in Figure 5-28. The z-x planar energy deposition distribution for all y-coordinates is shown in Figure 5-29. The x-y planar energy deposition distribution for the plane crossing the Bragg peak is shown in Figure 5-30. The z-x planar energy deposition distribution on the $y = 0$ cm plane is shown in Figure 5-31. The lateral radius of the energy deposition distributions is about 20 cm.

The results in this case show that a narrow proton beam can be broadened by a single plate scatterer but the high-dose (energy deposition) profile is not flat.

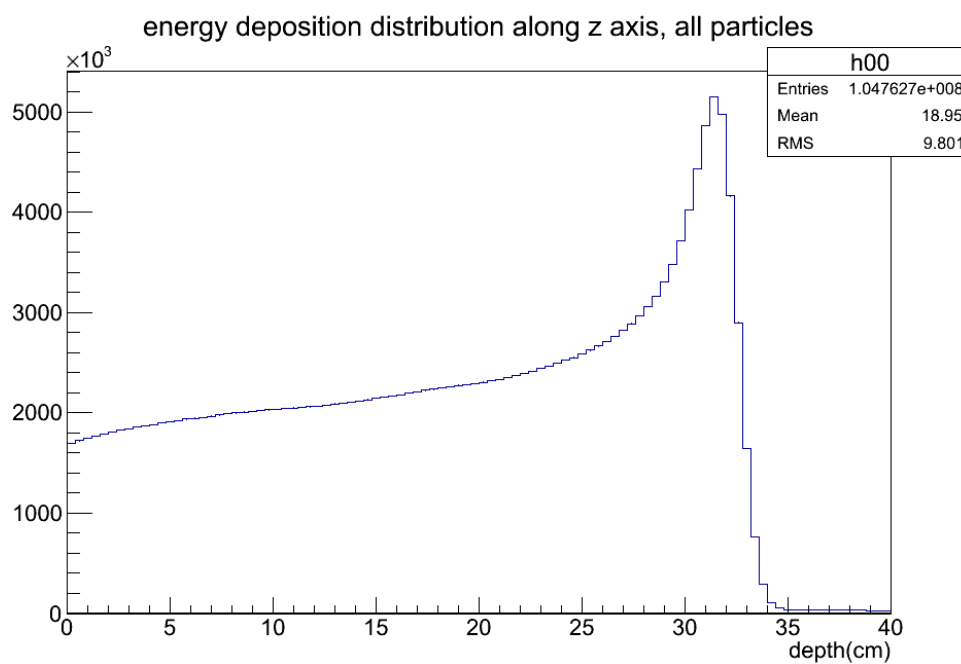


Figure 5-26. Energy Deposition along the z-Axis

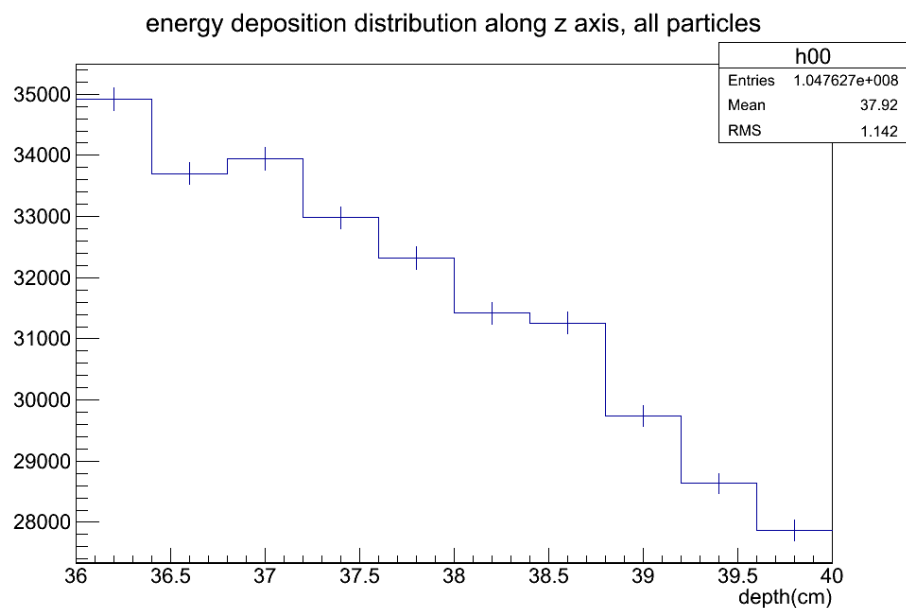


Figure 5-27. Depth Energy Deposition Distribution with Error Bar

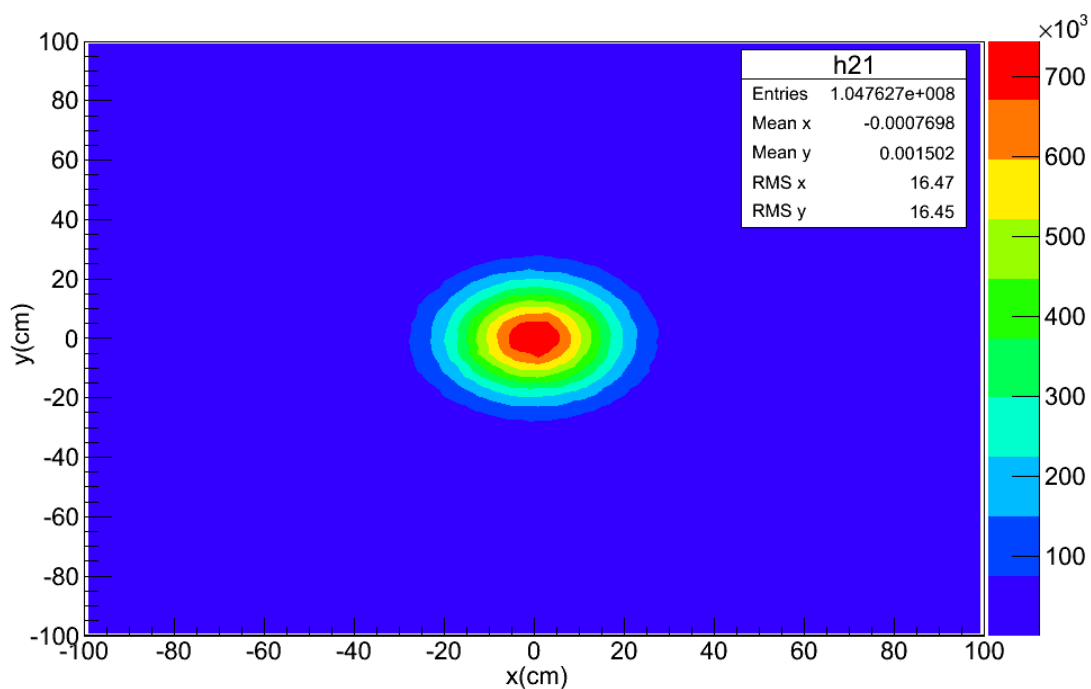


Figure 5-28. x-y Planar Energy Deposition Distribution, All z

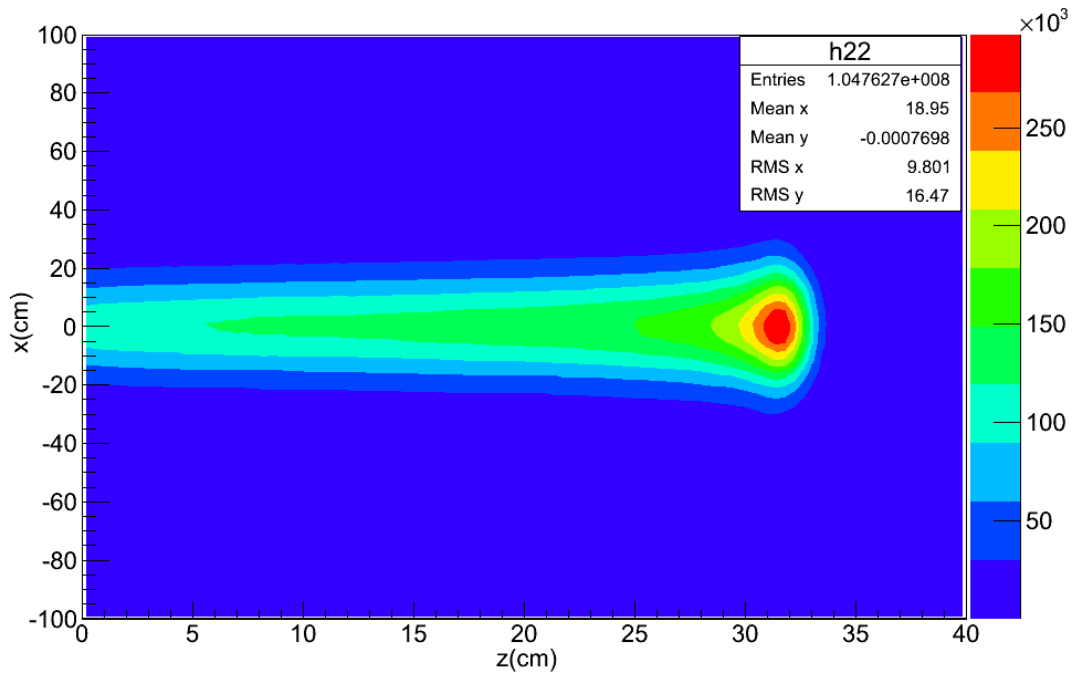


Figure 5-29. z-x Planar Energy Deposition Distribution, All y

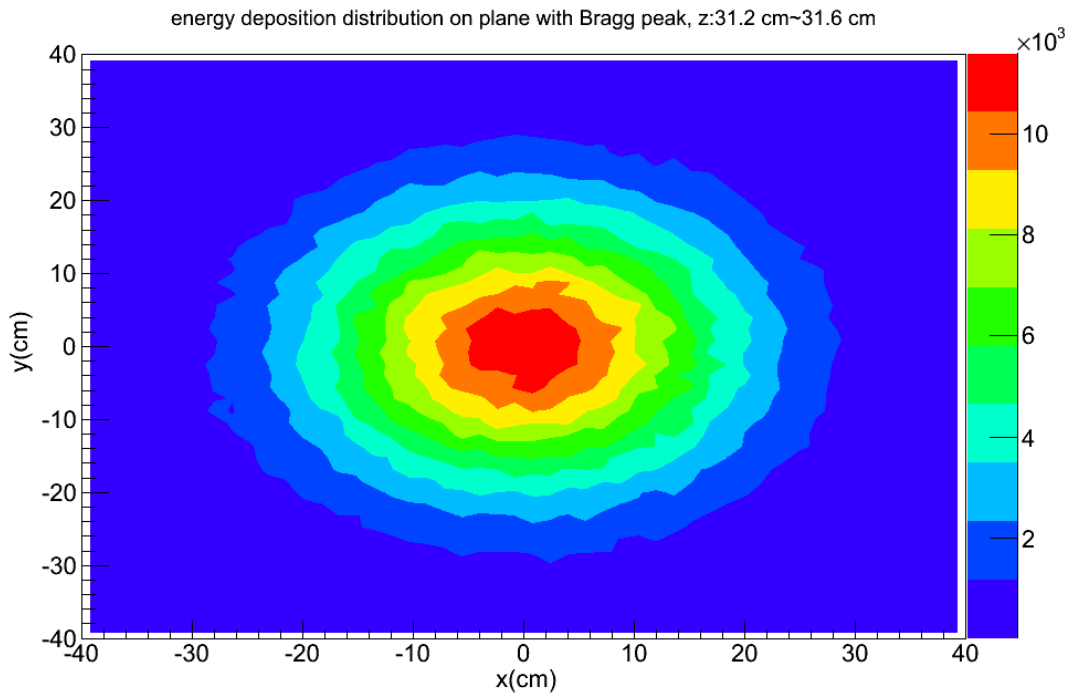


Figure 5-30. x-y Planar Energy Deposition Distribution, z:31.2~31.6 cm

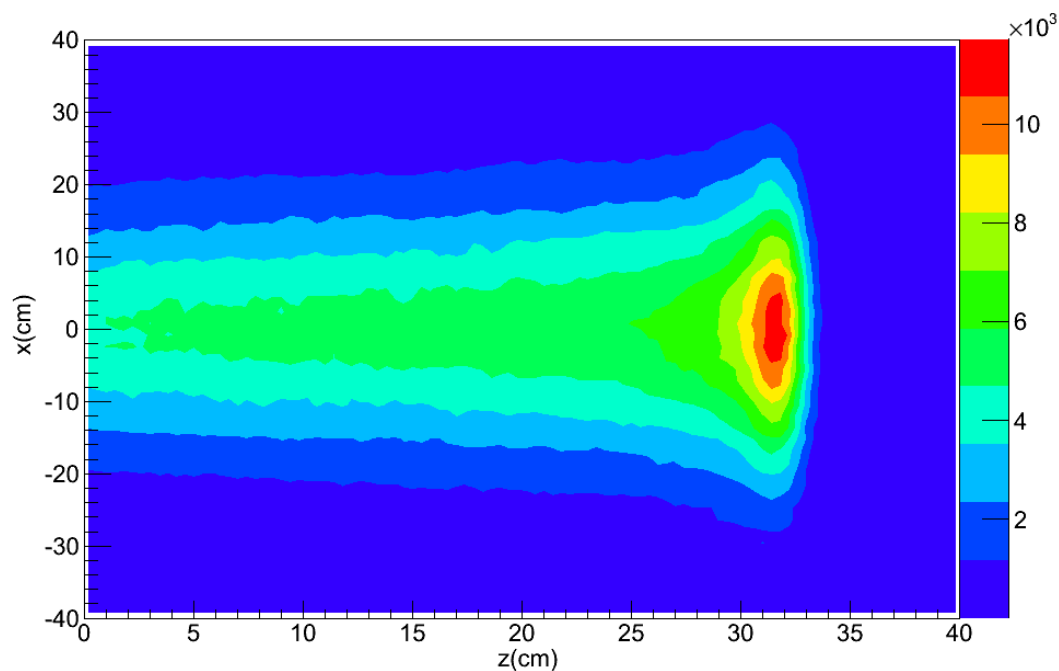


Figure 5-31. z-x Planar Energy Deposition Distribution, $y = 0$ cm

5.6 Results for Geometry Case No. 3

Based on case No. 2, the Gaussian shaped second scatterer (S2) was added downstream 50 cm away from the first disc scatterer. The purpose was to study the flattening function of S2 on the beam profile. The primary proton current distribution is shown in Figure 5-32, on which there is a near-uniform, high-current region at the center. This near-flat current region shows that S2 indeed can flatten the beam profile laterally. The polar angle of momentum direction distribution of primary protons incident on the front surface of the water phantom is shown in Figure 5-33. The mean scattering polar angle is about 4.4 degrees with the maximum angle of about 30 degrees. The kinetic energy distribution of primary protons is shown in Figure 5-34. Some protons have

energies between 50 and 100 MeV. These low-energy protons may have lost most of their energy in the brass-collimator part of S2.

The x-y planar energy deposition distribution for all z-coordinates is shown in Figure 5-35. The z-x planar energy deposition distribution for all y-coordinates is shown in Figure 5-36. The z-x planar energy deposition distribution on $y = 0$ cm plane is shown in Figure 5-37. The x-y planar energy deposition distribution on the plane crossing the Bragg peak is shown in Figure 5-38. These figures show that S2 can flatten the beam profile.

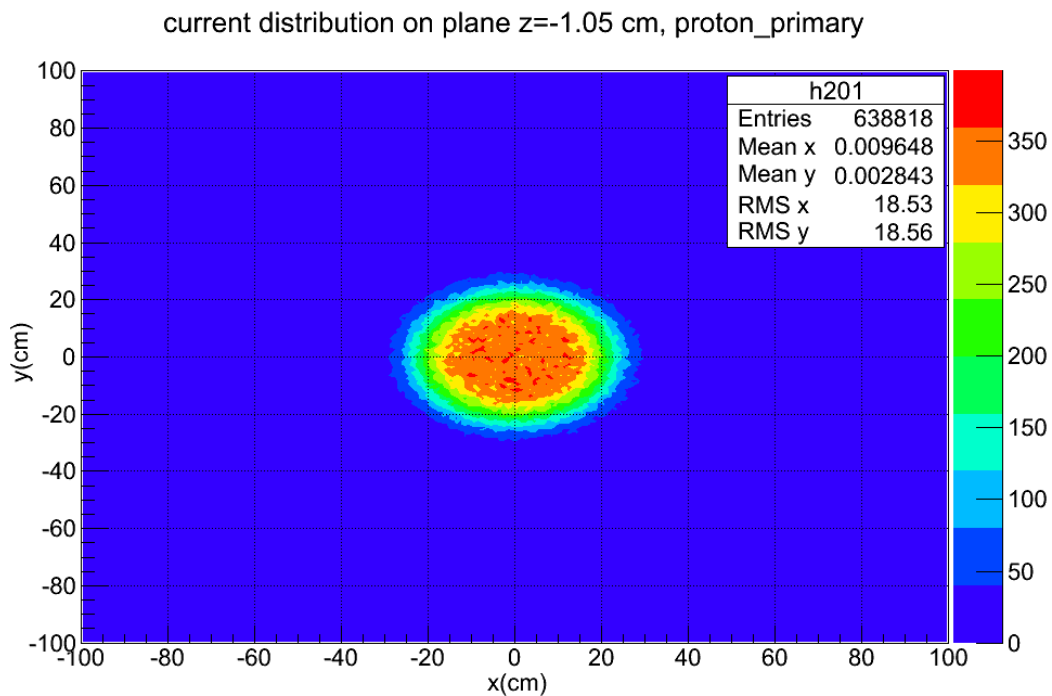


Figure 5-32. Particle Current Distribution of the Primary Protons on the Plane $z = -1.05$ cm

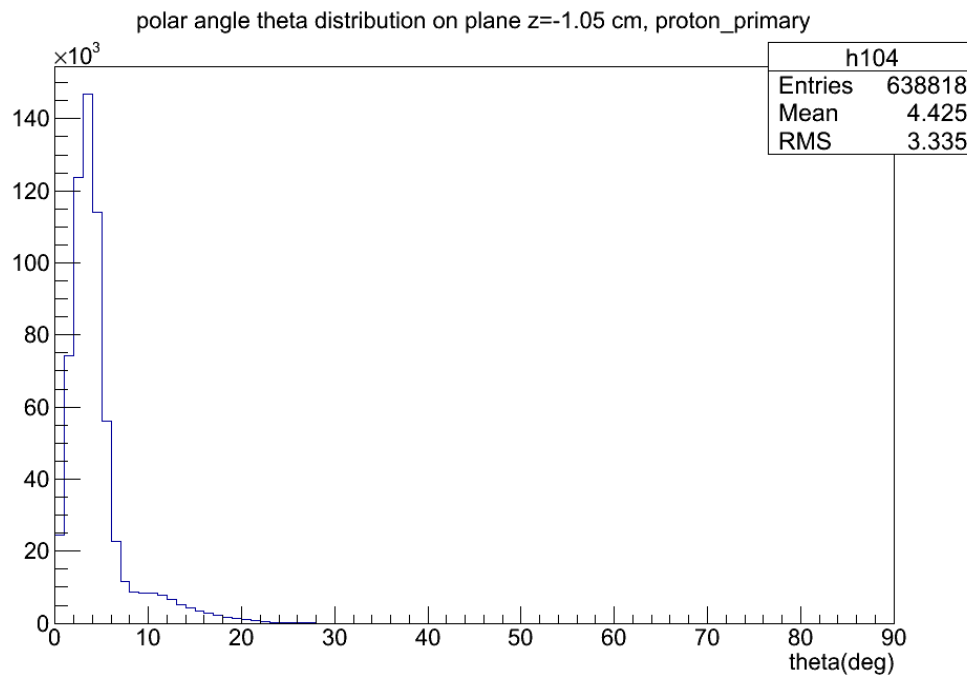


Figure 5-33. Polar Angle Distribution of the Primary Protons on the Plane $z = -1.05$ cm

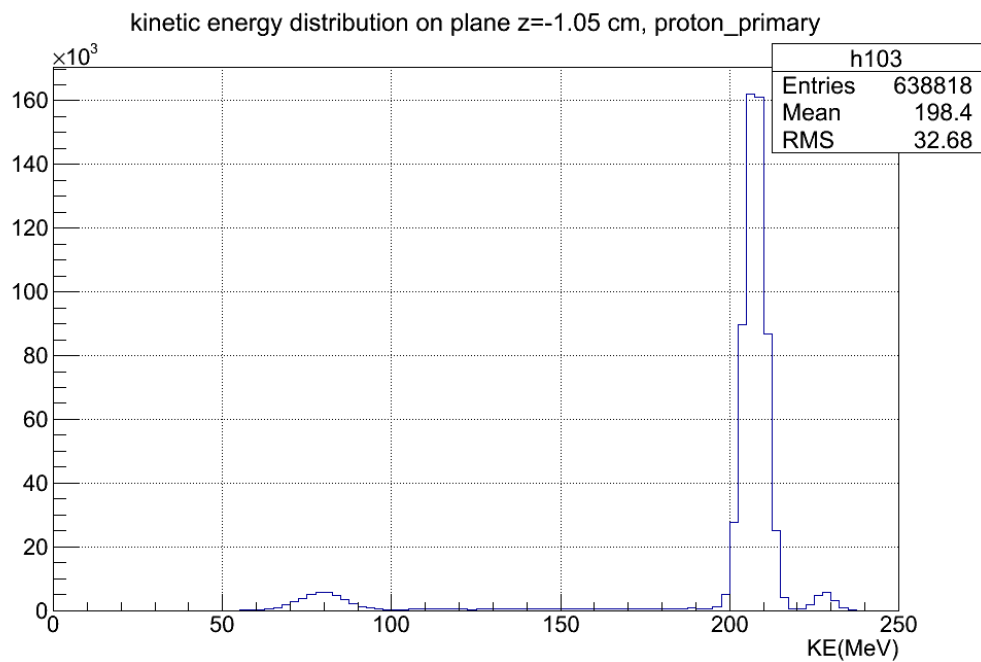


Figure 5-34. Kinetic Energy Distribution of the Primary Protons on the Plane $z = -1.05$ cm

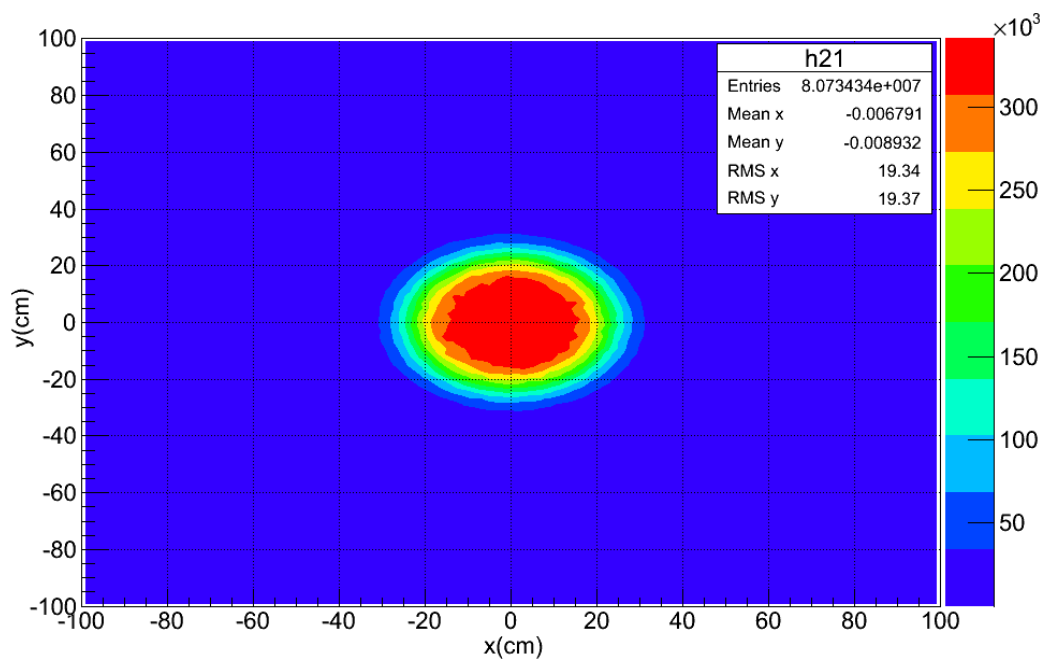


Figure 5-35. x-y Planar Energy Deposition Distribution, All z

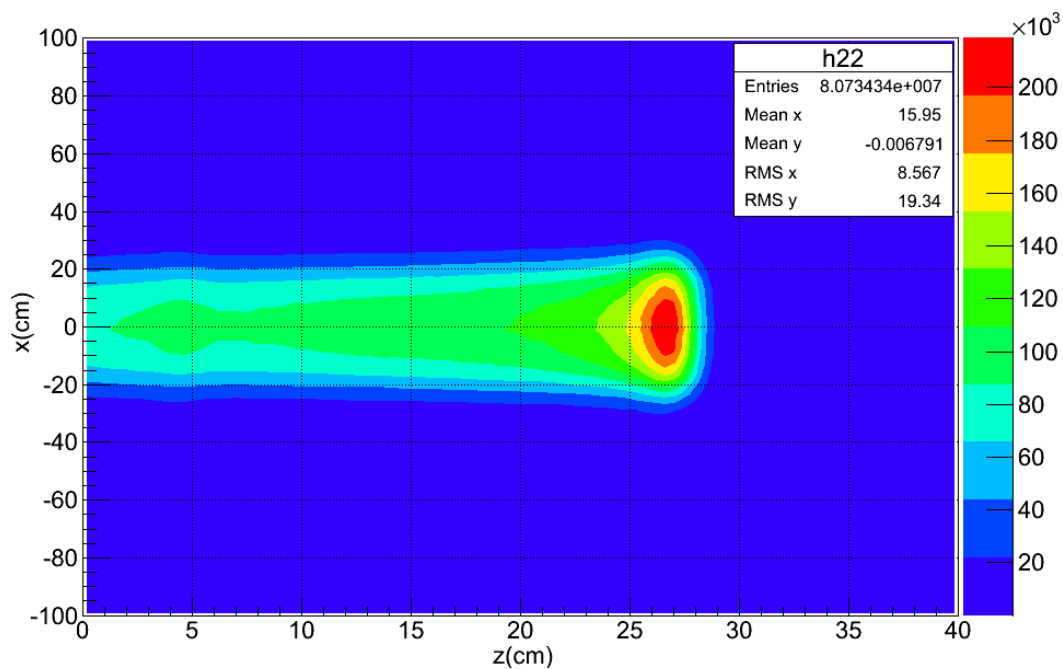


Figure 5-36. z-x Planar Energy Deposition Distribution, All y

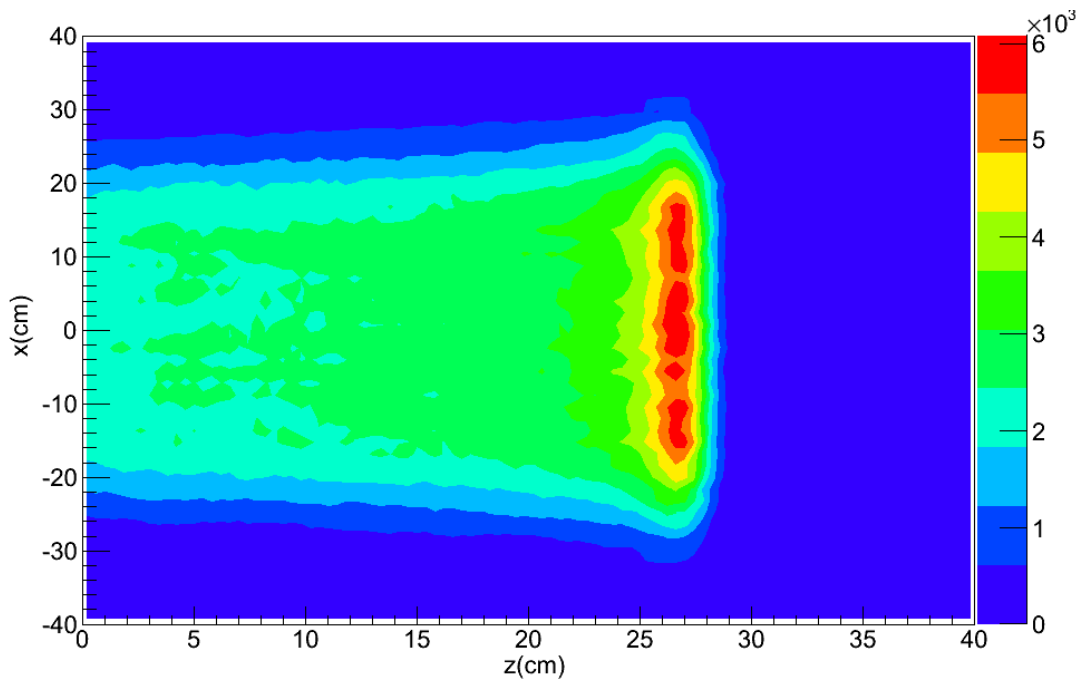


Figure 5-37. z-x Planar Energy Deposition Distribution, $y = 0$ cm

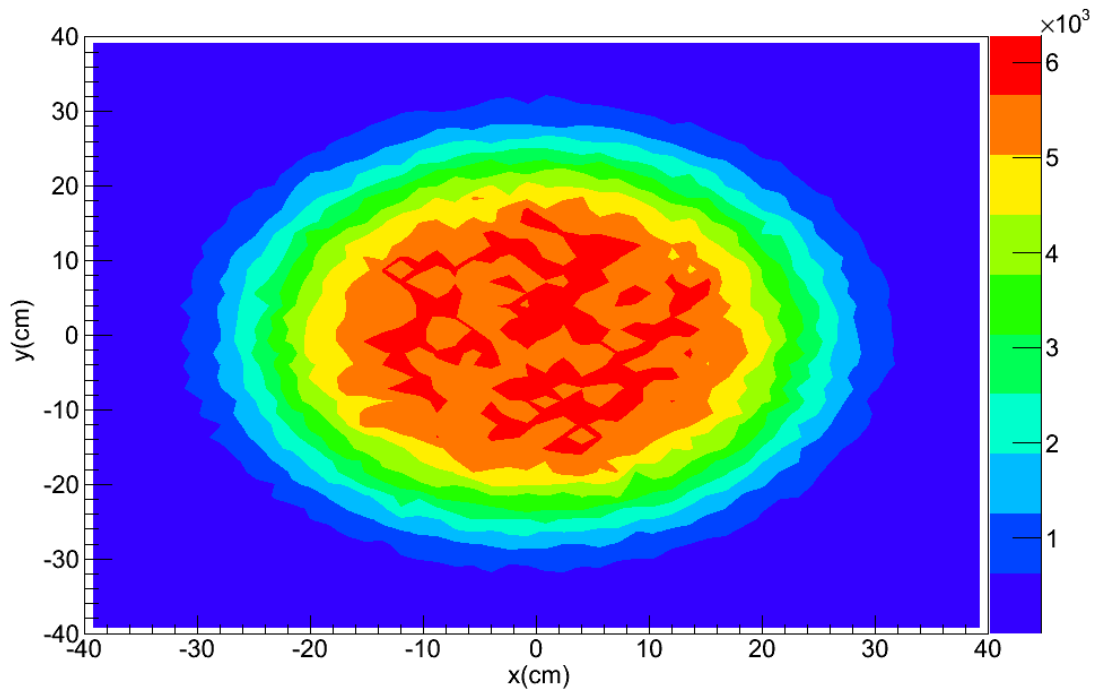


Figure 5-38. x-y Planar Energy Deposition Distribution, $z:26.4\sim 26.8$ cm

5.7 Results for Geometry Case No. 4

Based on the case No. 3, the range modulation wheel was used instead of a single scattering disc, and a long shielding shell was added in case No. 4. The purpose of combining S1 and S2 was to obtain the SOBP dose curve. The function of the long shielding shell was to eliminate the over-scattered useless beam. The inner radius of the long shielding shell was 15 cm.

The execution of this application included 1440 runs, in each of which the rotation angle of the range modulation wheel was increased by 0.25 degree to make the wheel rotate $(1440)(0.25) = 360$ degrees in the whole execution, so that all the steps in the wheel would make a contribution to the final energy deposition in the water phantom. The number of primary protons in each run was set to 1500, so the total number of primary protons in the whole execution was 2.16×10^6 .

The SOBP curve is shown in Figure 5-39. The SOBP extends from $z = 17$ cm to $z = 26.5$ cm, and the width is close to the expected width of 10 cm. The primary protons contribute most to the total energy deposition. The contribution of neutron relatives is too low to be seen on a linear-scale plot. The log-scale plot is shown in Figure 5-40. The contribution of neutron relatives to total energy deposition is $1.456 \times 10^5 / 1.66 \times 10^7$ equal to 0.88%.

The z-x planar energy deposition distribution for all y-coordinates is shown in Figure 5-41. The x-y planar energy deposition distribution for all z-coordinates is shown in Figure 5-42. The z-x planar energy deposition distribution for the $y = 0$ cm plane is shown in Figure 5-43. The x-y planar energy deposition distribution for the plane

crossing the Bragg peak is shown in Figure 5-44, in which the width of the scoring layer is 0.4 cm. The x-y planar energy deposition distribution for the center z-plane (z: 19.6~20.4 cm) is shown in Figure 5-45, in which the width of the scoring layer is 0.8 cm. The maximum value in Figure 5-45 is roughly double the maximum value in Figure 5-44 because of the double relation of the width of the scoring layer. These figures show that a high-dose region was produced from the geometry settings in this case.

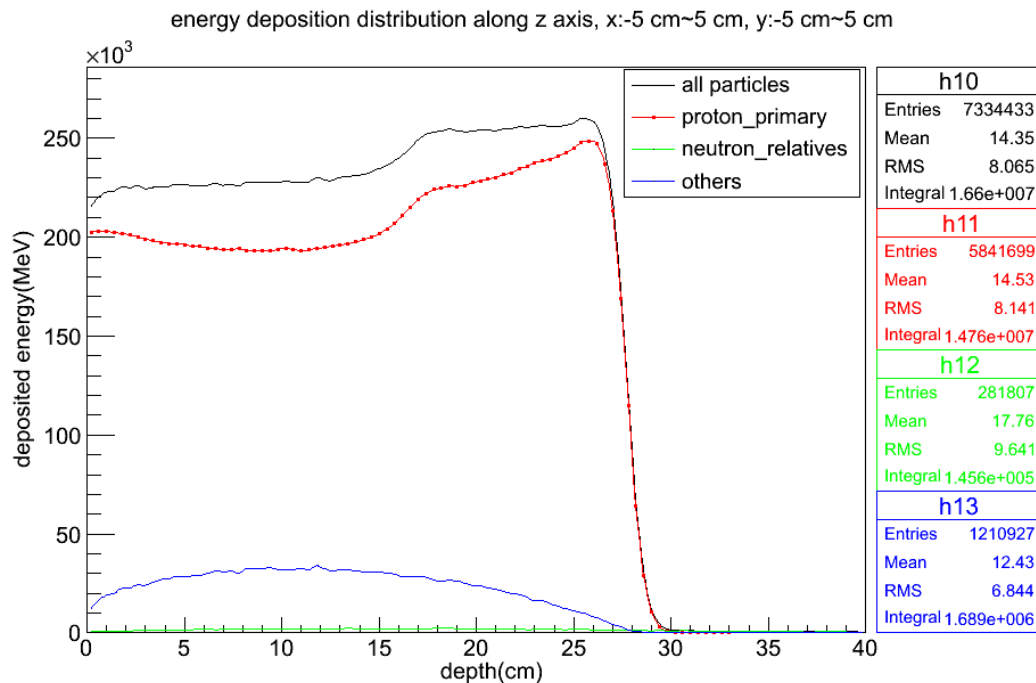


Figure 5-39. SOBP Curve along the z-Axis on a Linear-Scale

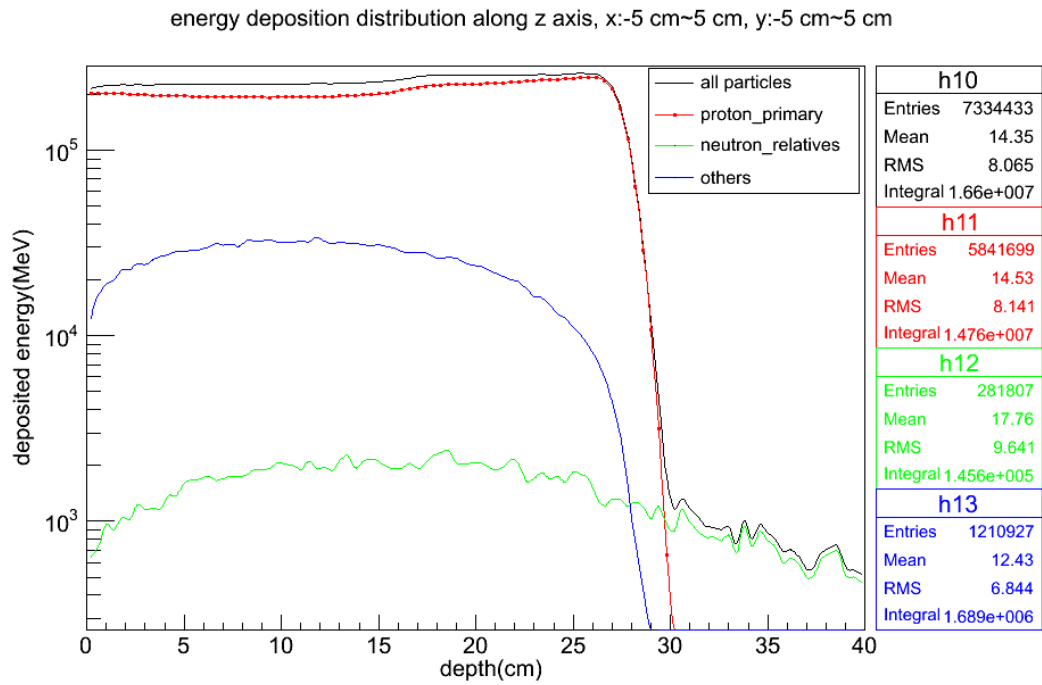


Figure 5-40. SOBP Curve along the z-Axis on a Log-Scale

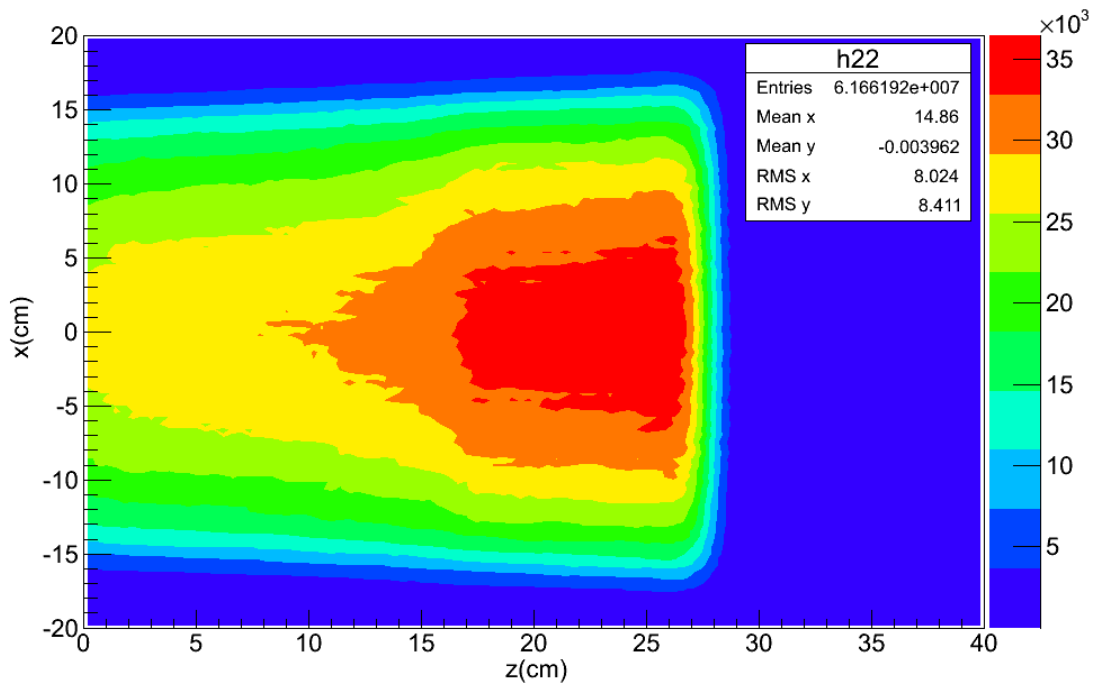


Figure 5-41. z-x Planar Energy Deposition Distribution, All y

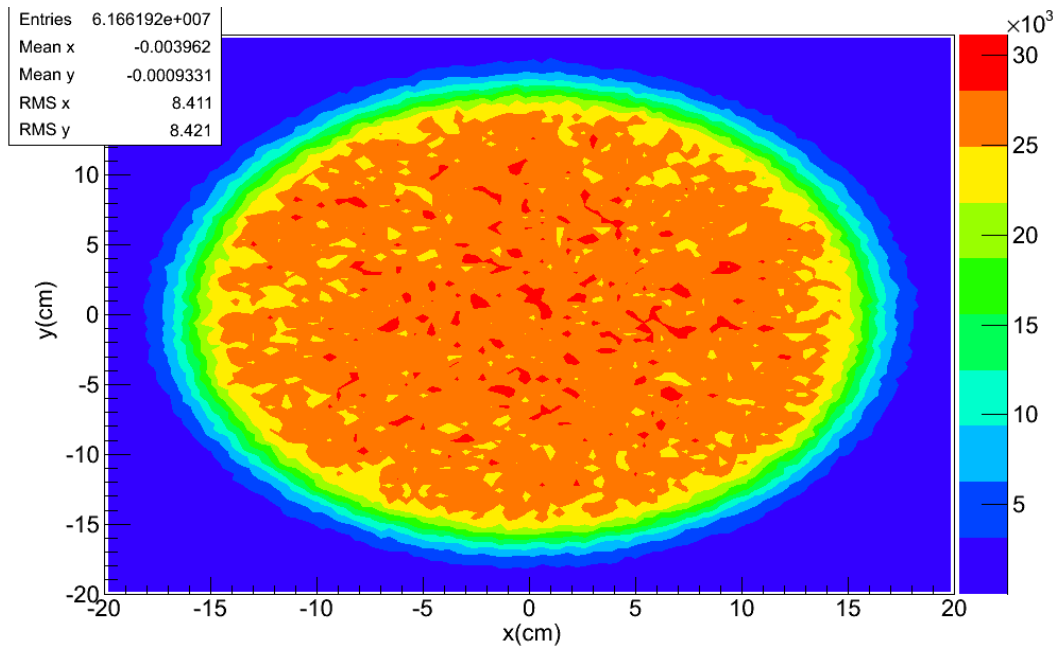


Figure 5-42. x-y Planar Energy Deposition Distribution, All z

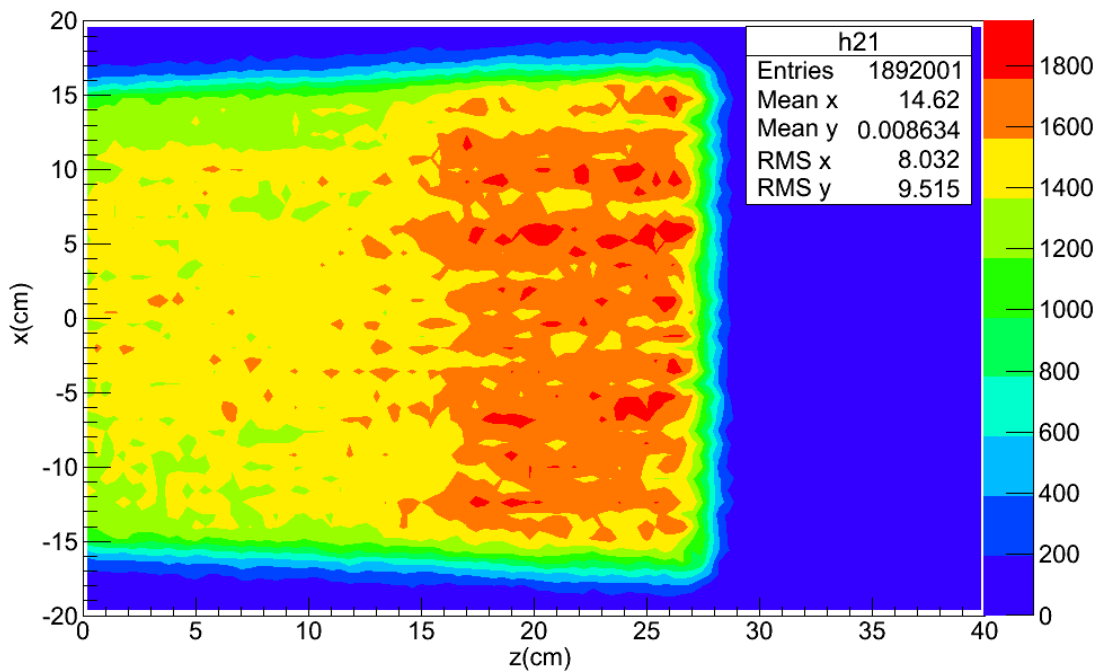


Figure 5-43. z-x Planar Energy Deposition Distribution on the Plane y = 0 cm

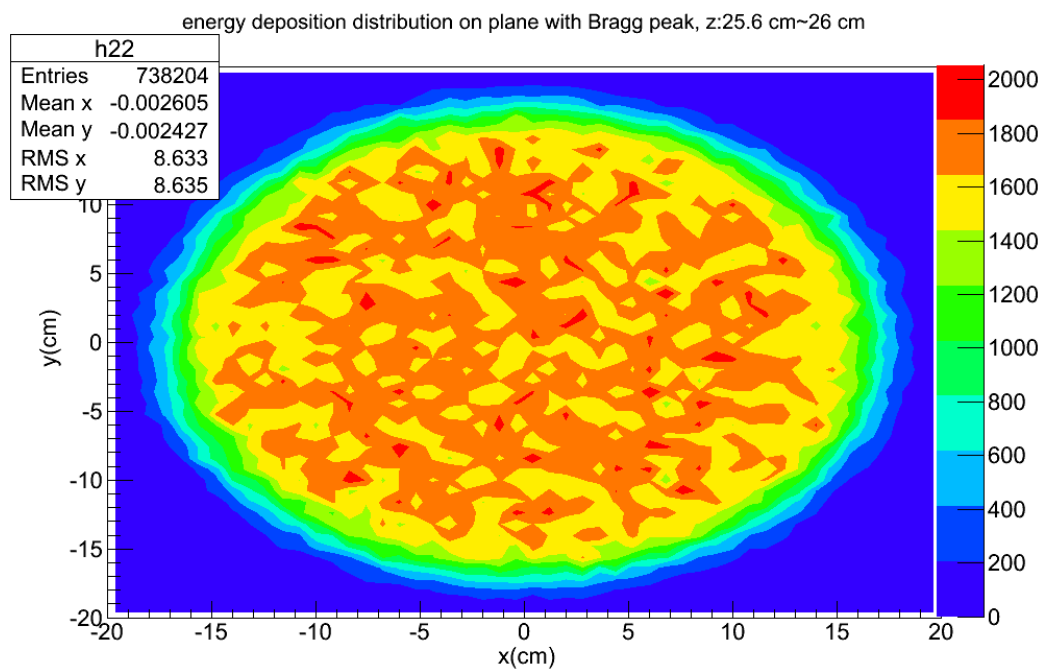


Figure 5-44. x-y Planar Energy Deposition Distribution on the Plane with Bragg Peak

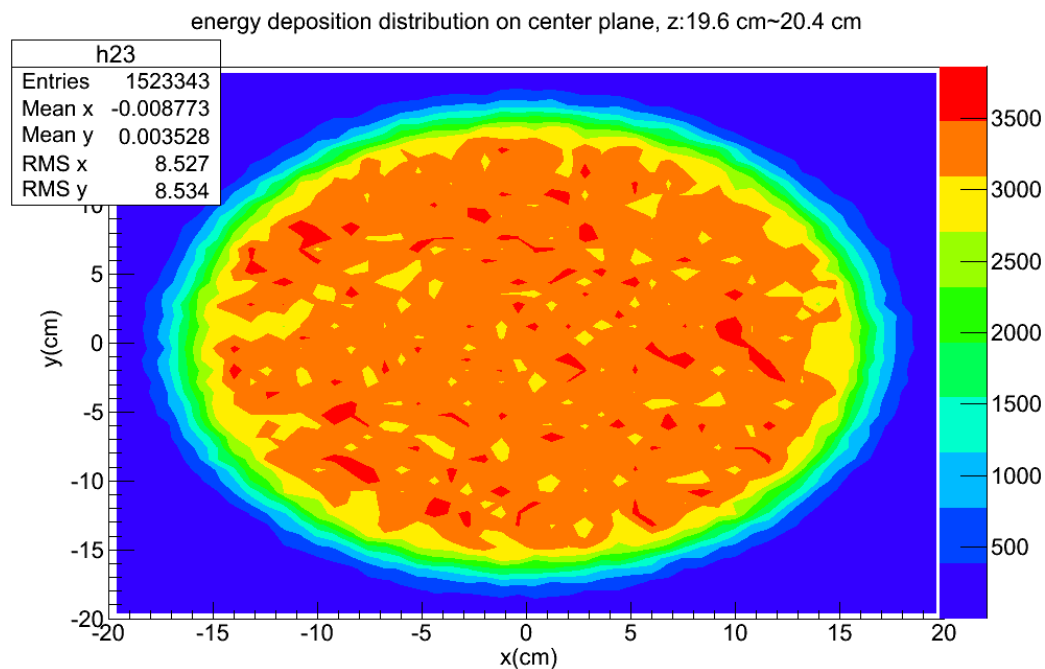


Figure 5-45. x-y Planar Energy Deposition Distribution, z: 19.6~20.4 cm

5.8 Results for Geometry Case No. 5

All the components of a nozzle were used in case No. 5. The high-dose edge is $z = 28$ cm in case No. 3 and No. 4. If we assumed there was a tumor with a radius of 5 cm locating at the center of the water phantom, the extension of the tumor was from 15 cm to 25 cm. To make the high-dose region cover the tumor fully, the SOBPs should shift 3 cm backward. The compensator material was ABS resin with a density of 1.04 g cm^{-3} , close to the density of water, so we can simply assume the thickness of range shifter part on compensator is also equal to 3 cm. Besides, to obtain conformal dose distribution in tumor, we need to set the inner radius of range compensator to 5 cm. We have defined two UI commands to adjust the radius of the range compensator and thickness of range shifter part on the compensator. It is convenient for users because these two UI commands can be invoked after the application has been compiled and linked.

The primary proton source setting was same as in case No. 4 and the total number of primary protons was 2.16×10^6 to make the range modulation wheel rotate 360 degrees in the whole execution.

The geometry and all particle trajectories from ten primary protons for case No. 5 are shown in Figure 5-46.

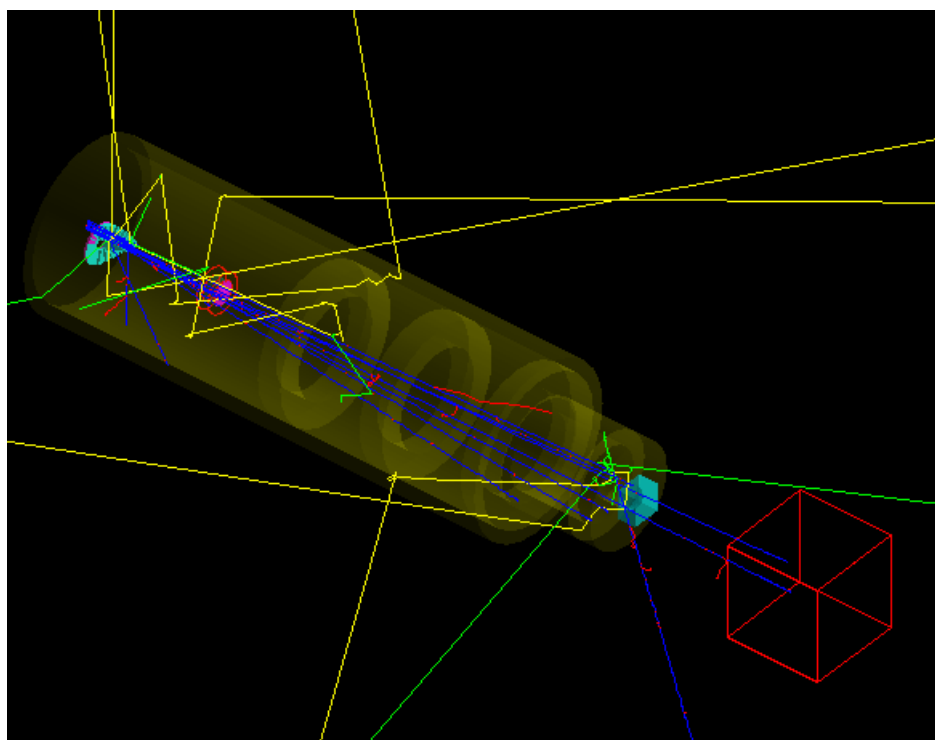


Figure 5-46 Geometry and Trajectories in Case No. 5

The z-x planar energy deposition distribution for all y-coordinates is shown in Figure 5-47. The x-y planar energy deposition distribution for all z-coordinates is shown in Figure 5-48. The z-x planar energy deposition distribution for the $y = 0$ cm plane is shown in Figure 5-49. The x-y planar energy deposition distribution for the plane crossing the Bragg peak is shown in Figure 5-50. These figures show that the expected energy deposition (dose) distribution can be obtained from the settings in this case. The distribution in high-dose region is not flat ideally because the number of particles reaching the water phantom is not large enough. If we increase the NPS for the simulation, better results would be obtained.

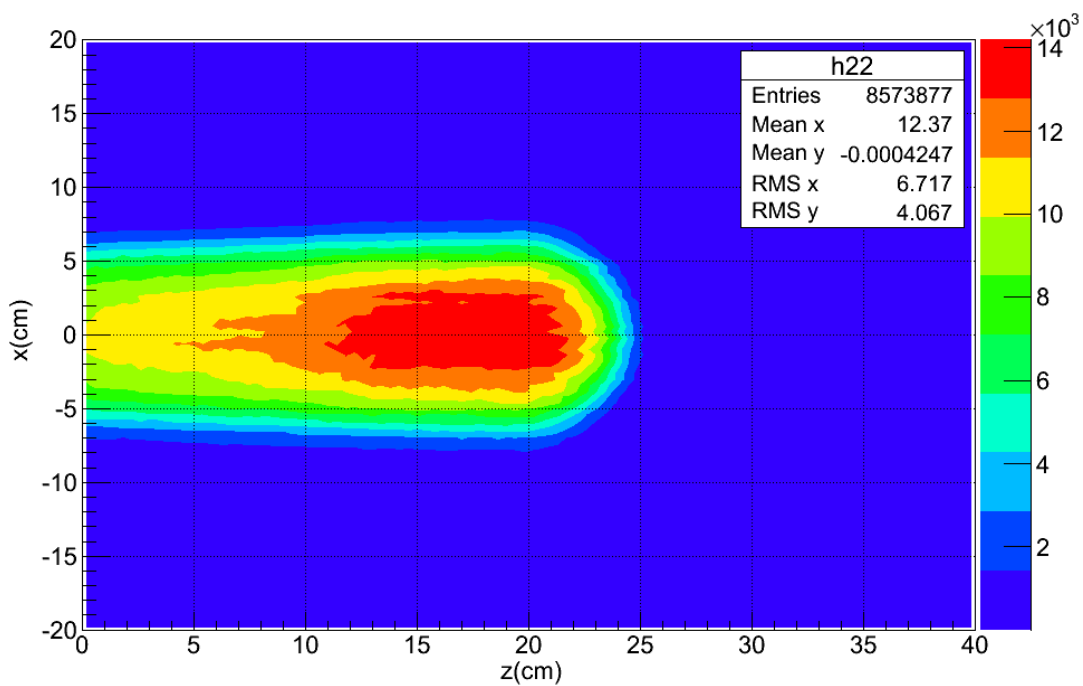


Figure 5-47. z-x Planar Energy Deposition Distribution, All y

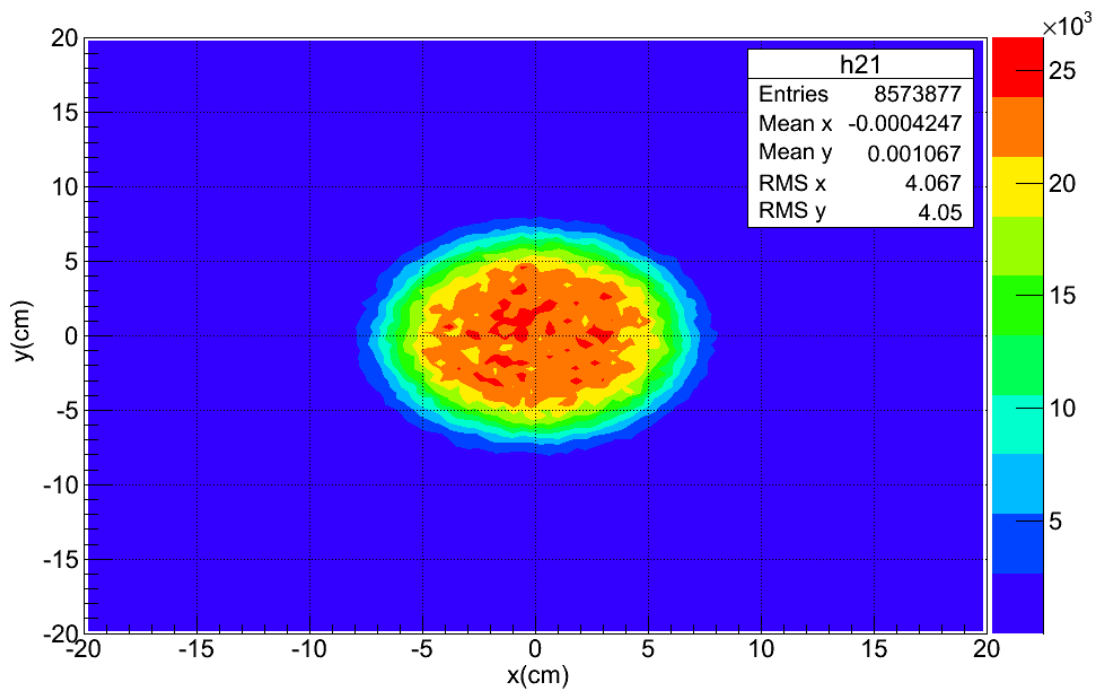


Figure 5-48. x-y Planar Energy Deposition Distribution, All z

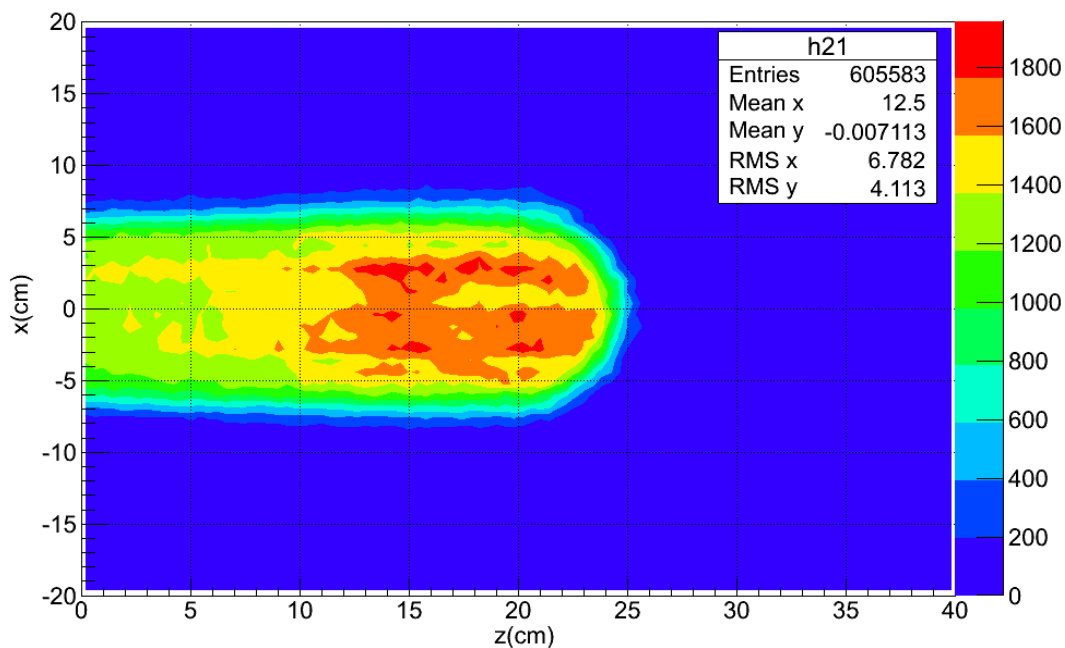
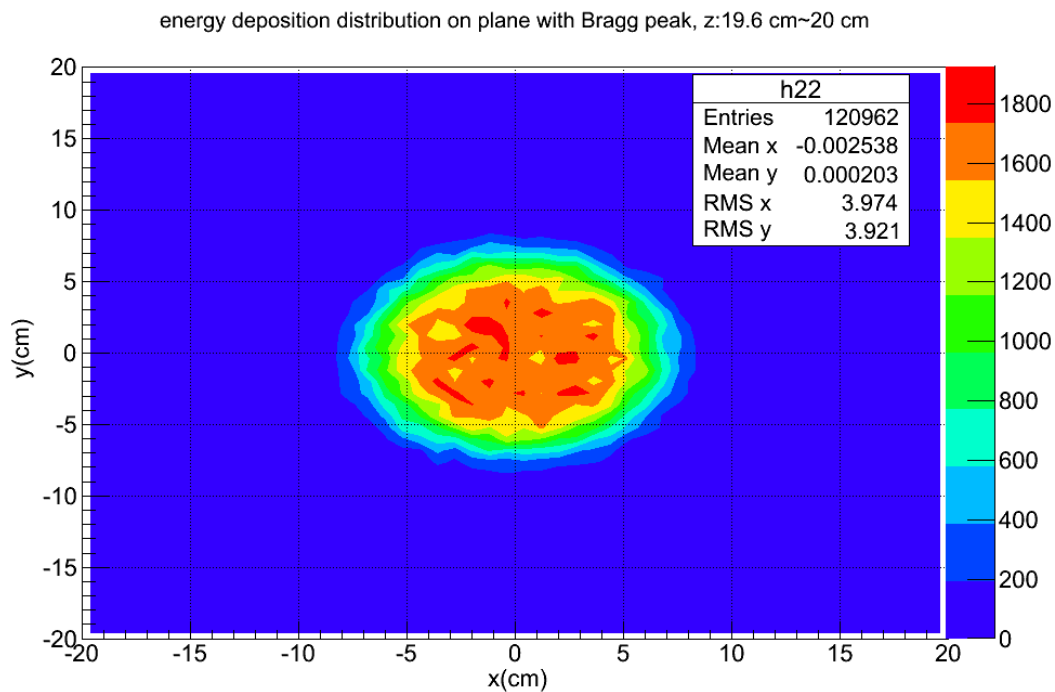
Figure 5-49. Energy Deposition Distribution on the Plane $y = 0$ cm

Figure 5-50. Energy Deposition Distribution on the Plane with the Bragg Peak

5.9 Results for Geometry Case No. 5 from Two Irradiations

In practice, the nozzle can rotate around the patient, so multiple irradiations from different nozzle directions can give a better dose distribution result. Under the condition of maintaining the same dose to the target tumor, the dose to surrounding healthy tissues could be lower but more tissues would be irradiated. This is similar to IMRT.

We defined a UI command to control the rotation angle of nozzle around the central dose scoring volume. A nozzle with rotation angle of 180 degrees is shown in Figure 5-51.

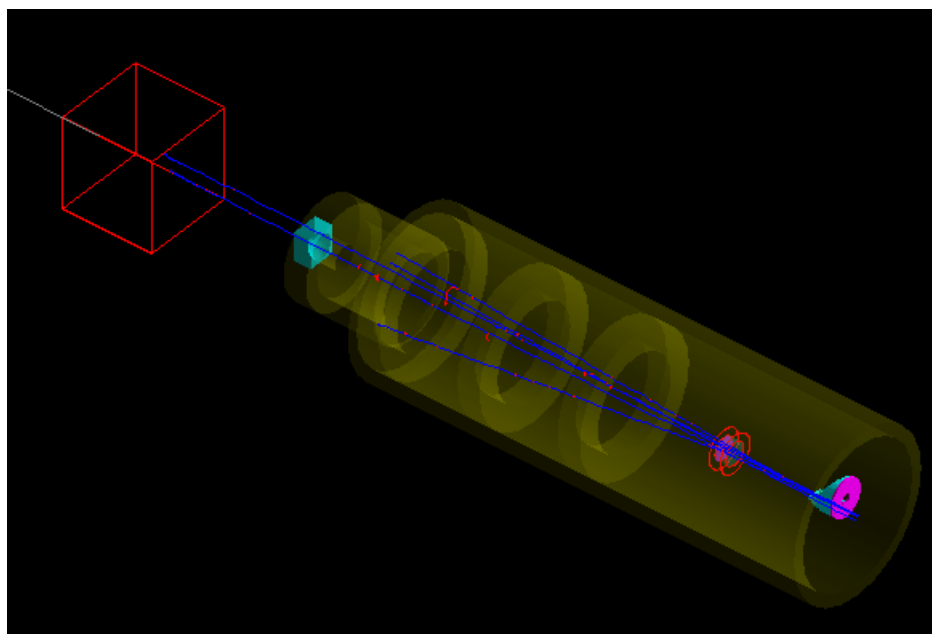


Figure 5-51. Nozzle with a 180-Degree Rotation Angle around the Water Phantom

This case had the exactly same settings as case No. 5 but two irradiations were used. We first executed 1440 runs with 0 degrees as the rotation angle of the nozzle. Then, we rotated the nozzle by 180 degrees, and meanwhile cleared the old primary source definition, and defined a new primary source on the plane $z = 340$ cm with initial momentum direction along negative z-axis. We also executed 1440 runs for the second irradiation. The number of primary protons was 2.16×10^6 for each nozzle angle, so the total number of primary protons was 4.32×10^6 for the two irradiations.

The summed results from two irradiations are shown in the following figures. The energy deposition curve along the z-axis is shown in Figure 5-52. The z-x planar energy deposition distribution for all y-coordinates is shown in Figure 5-53. The x-y planar energy deposition distribution for all z-coordinates is shown in Figure 5-54. The z-x planar energy deposition distribution for the $y = 0$ cm plane is shown in Figure 5-55. The x-y planar energy deposition distribution for the plane crossing the Bragg peak is shown in Figure 5-56. A 3D energy-deposition distribution plotted using SimpleGeo is shown in Figure 5-57. The 3D energy-deposition distribution plotted using root with a C++ file defined by us is shown in Figure 5-58. These figures show that the expected energy deposition (dose) distribution was obtained from the settings in this case. Under the conditions of the same dose to the target tumor, two irradiations from different directions can indeed decrease the relative dose to the tissues surrounding the tumor.

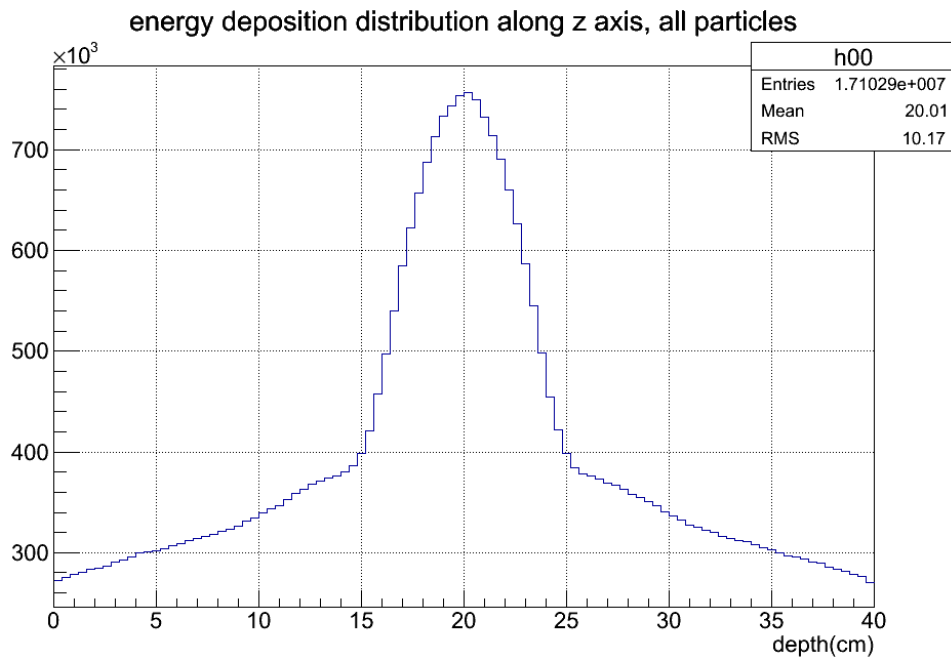


Figure 5-52. Energy Deposition Distribution along the z-Axis, All x and All y

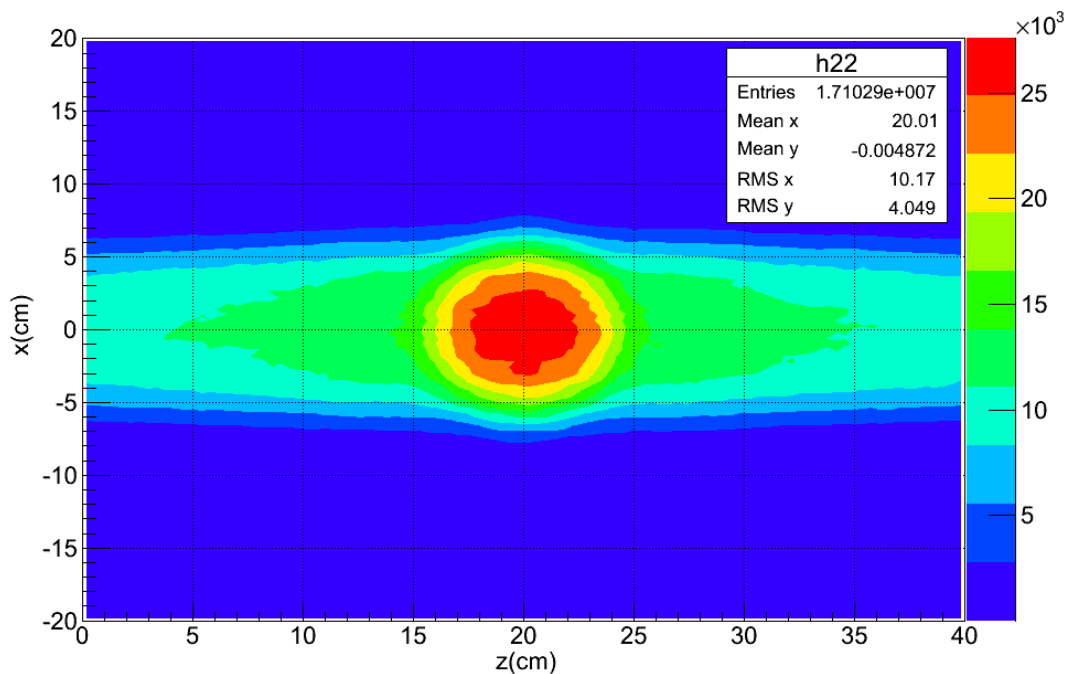


Figure 5-53. z-x Planar Energy Deposition Distribution, All y

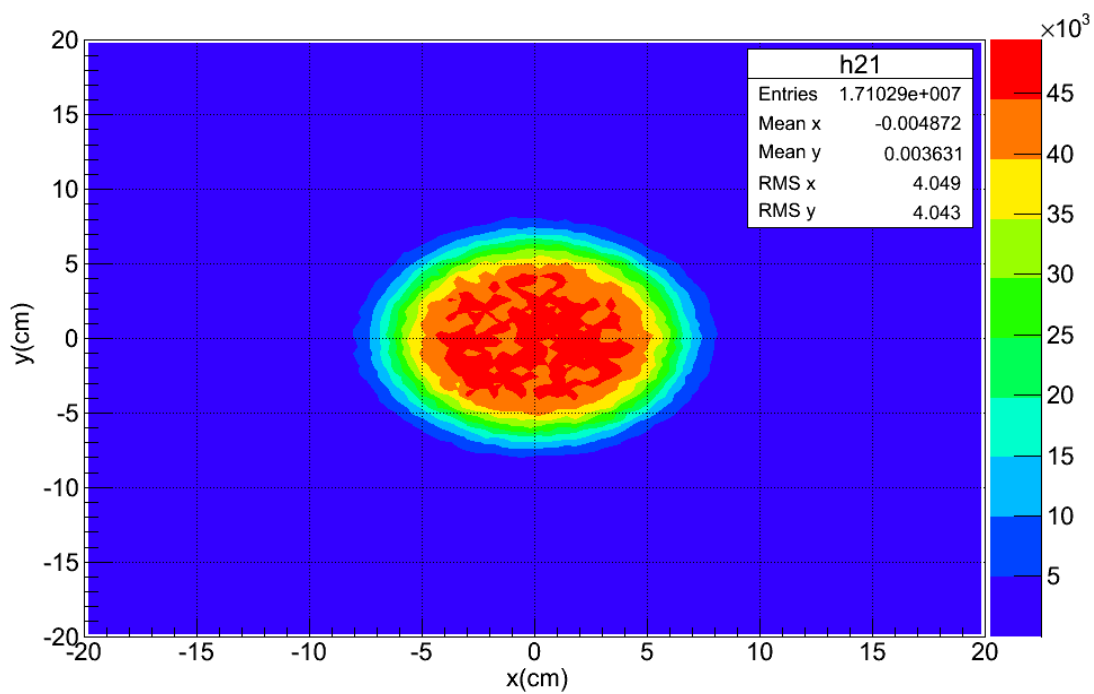
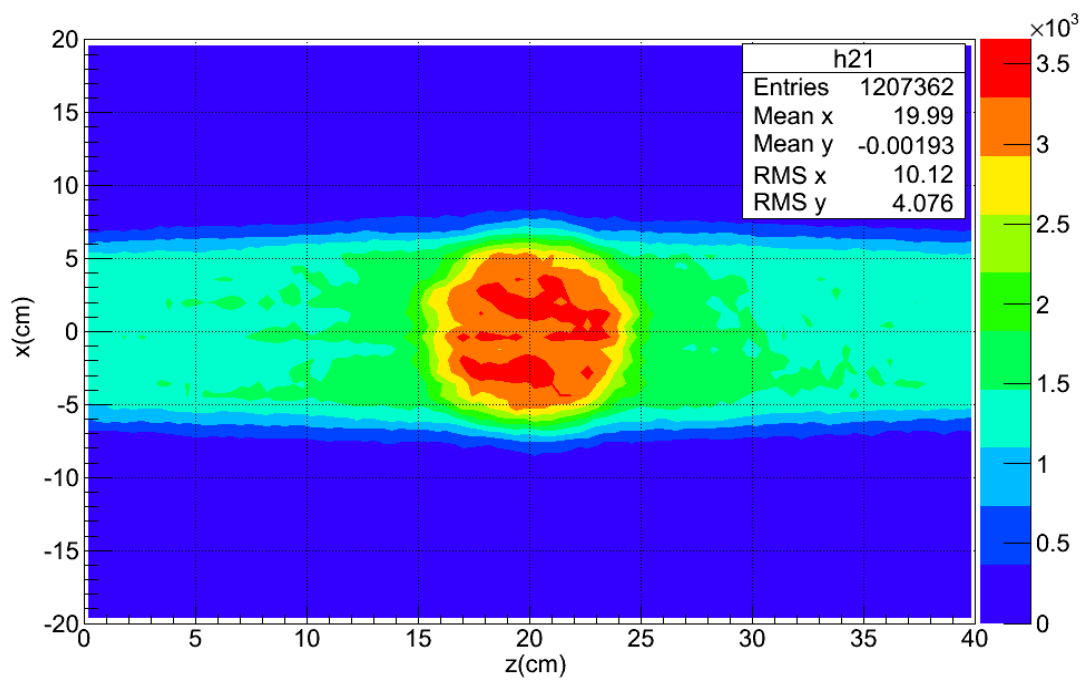


Figure 5-54. x-y Planar Energy Deposition Distribution, All z

Figure 5-55. Energy Deposition Distribution on the Plane $y = 0$ cm

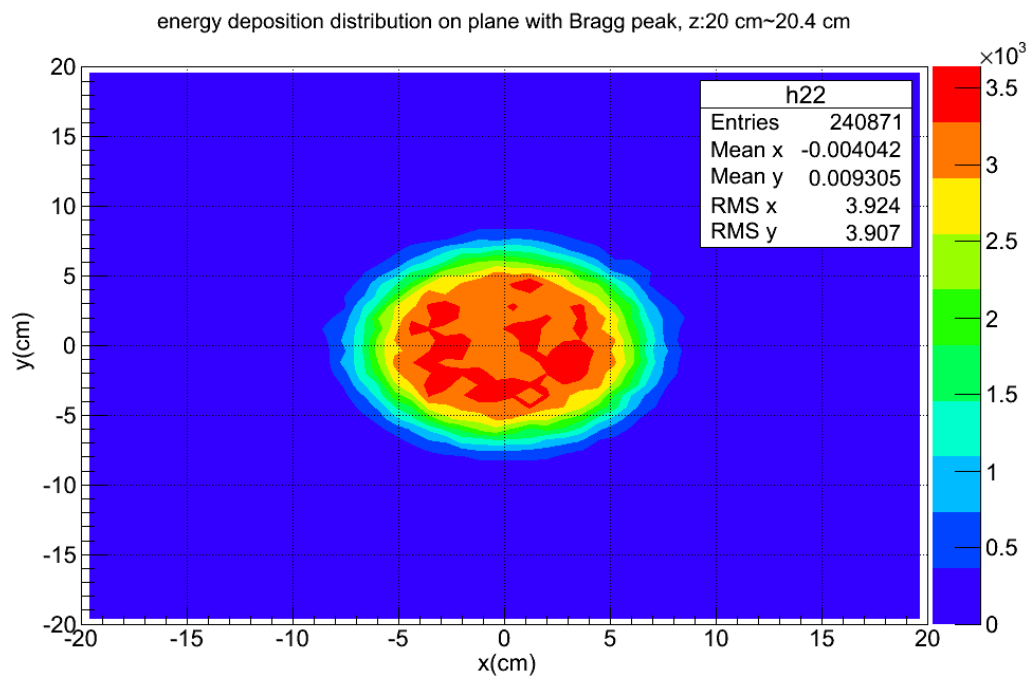


Figure 5-56. Energy Deposition Distribution on the Plane with the Bragg Peak

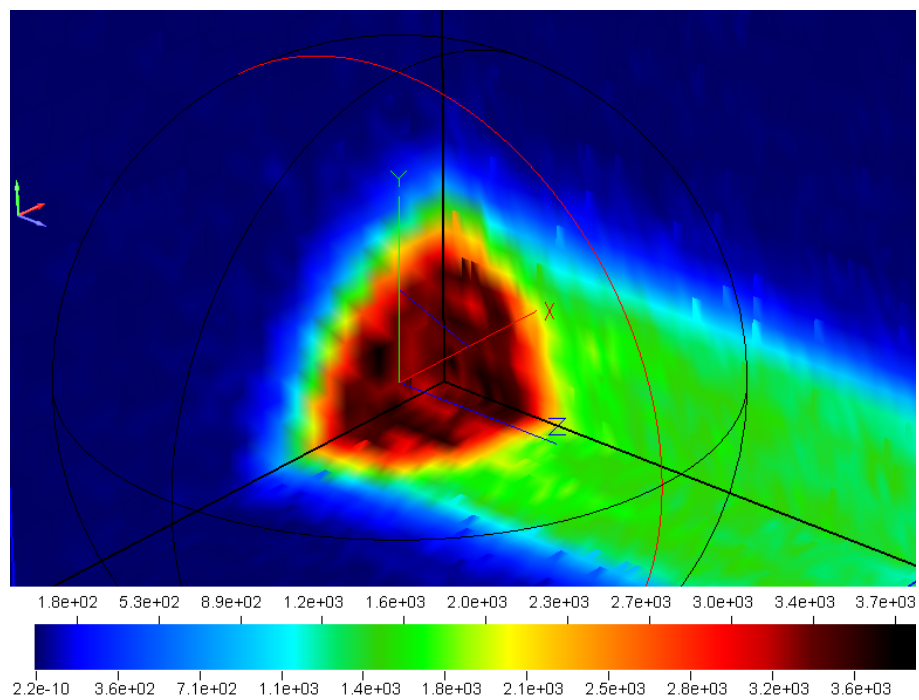


Figure 5-57. 3D Energy Deposition Distribution Plotted Using SimpleGeo

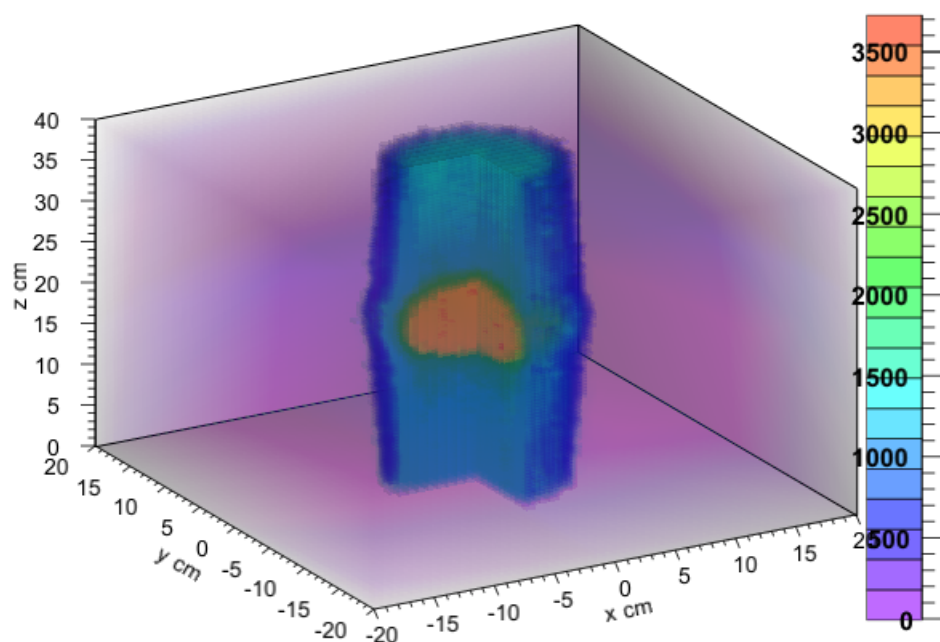


Figure 5-58. Cut-View of 3D Energy Deposition Distribution Plotted Using Root

5.10 Results for Geometry Case No. 6 in Treating Prostate Cancer

As described in section 4.2.5, the whole prostate gland and base of the bladder were selected as the GTV based on the PET images. The assumed CTV was a sphere with a radius of 3 cm to cover the whole GTV.

For this prostate cancer therapy case, a new S1 and S2 combination was designed using NEU. The SOBP in this case was 6 cm and the field size could be up to 15 cm from this S1 and S2 combination. The parameters are listed in Appendix C.

Not all the CT slices for this patient were used to build the voxel geometry in this case, and only 120 slices containing the bladder and prostate cancer were used. Each slice has a dimension of 50 cm \times 50 cm (512 \times 512 pixels), and a thickness of 1.5 mm. Each slice is compressed to 64 \times 64 pixels by a factor of 8 and four consecutive slices are

merged into one layer. The final number of voxels was $64 \times 64 \times 30$ and each voxel has a size of $7.8125 \text{ mm} \times 7.8125 \text{ mm} \times 6 \text{ mm}$. The voxel geometry is shown in Figure 5-59.

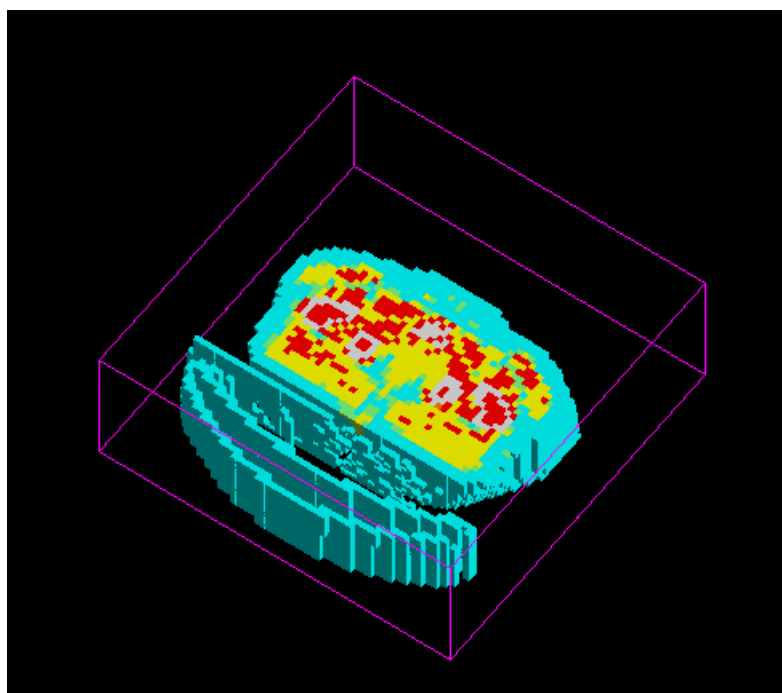


Figure 5-59. The Voxel Geometry of the Patient with Prostate Cancer

Although the CTV is assumed to be a sphere, we did not use a half-sphere range compensator for this case. We assumed the planning target volume (PTV) to be a cylinder with a radius of 3 cm and a length of 6 cm to cover the spherical CTV. The bone structure in this voxel geometry will influence the spatial dose distribution. The profile of the patient skin can also influence the dose distribution. The 3D reconstruction geometry of the patient and the bone structure are shown in Figure 5-60 and Figure 5-61, produced using InVesalius. Finally, a plate range shifter and a wedge range shifter (both

made of ABS resin) shown in Figure 5-62, were used in this case after several trials to make high-dose region roughly cover the CTV. The wedge shifter was used to offset the profile of the skin and the plate shifter was used to shift the final dose profile to the proper location.

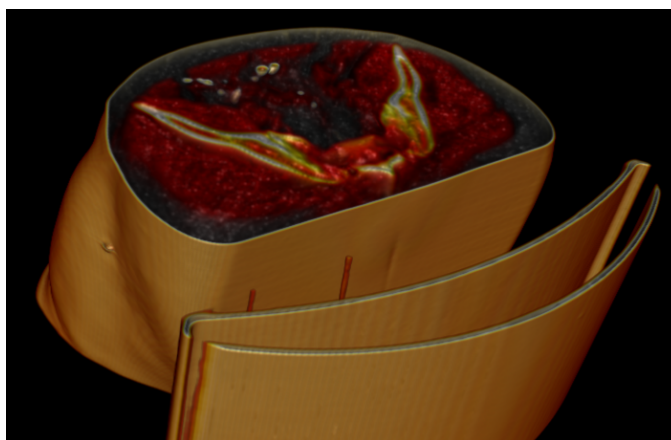


Figure 5-60. 3D Reconstruction of the Patient Geometry

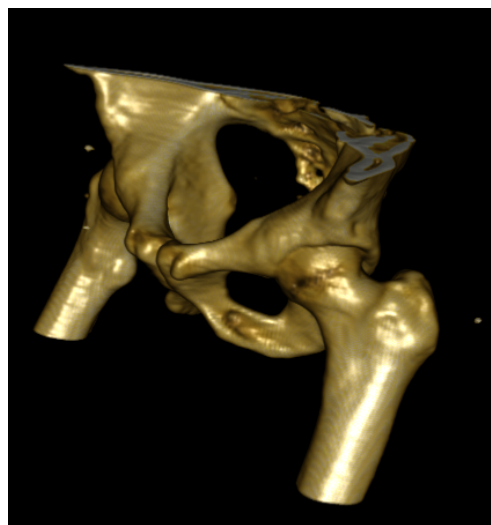


Figure 5-61. The Bone Structure of the Patient

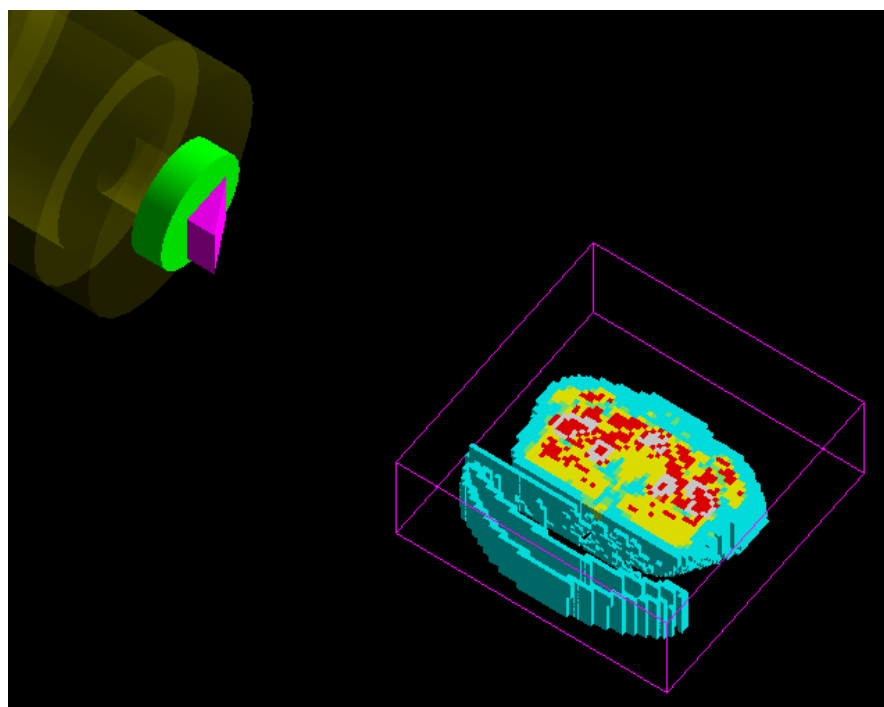


Figure 5-62. Plate Shifter, Wedge Shifter and the Patient Voxel Geometry

The treatment strategy for this patient included two irradiations, one which was from left to right and the other which was from right to left. When the nozzle irradiated from right, the wedge shifter was adjusted to offset the influence of the patient's right skin profile.

After several trials, the final aperture radius was set to 4 cm; the plate shifter thickness was set to 4.6875 cm; the long side of the wedge was set to 5 cm.

The number of events for each run was increased from 1500 to 3000, so the total number of events in this execution was 8.64×10^6 for two irradiations. The source codes of the main function for Geometry Case No.6 using Geant4 are listed in Appendix D.

The relative dose distributions (normalized by the maximum dose in the patient geometry) are plotted in the form of contour lines superimposed on the CT images. The axial, sagittal and coronal views of CT images with isodose lines are shown in Figure 5-63, Figure 5-64 and Figure 5-65. The high dose region (relative dose more than 0.8) can cover the CTV fully. The 3D absolute dose distribution plotted using SimpleGeo is shown in Figure 5-66.

All these figures show that in this case the target tumor and part of its surrounding tissues were covered by the high-dose fully.

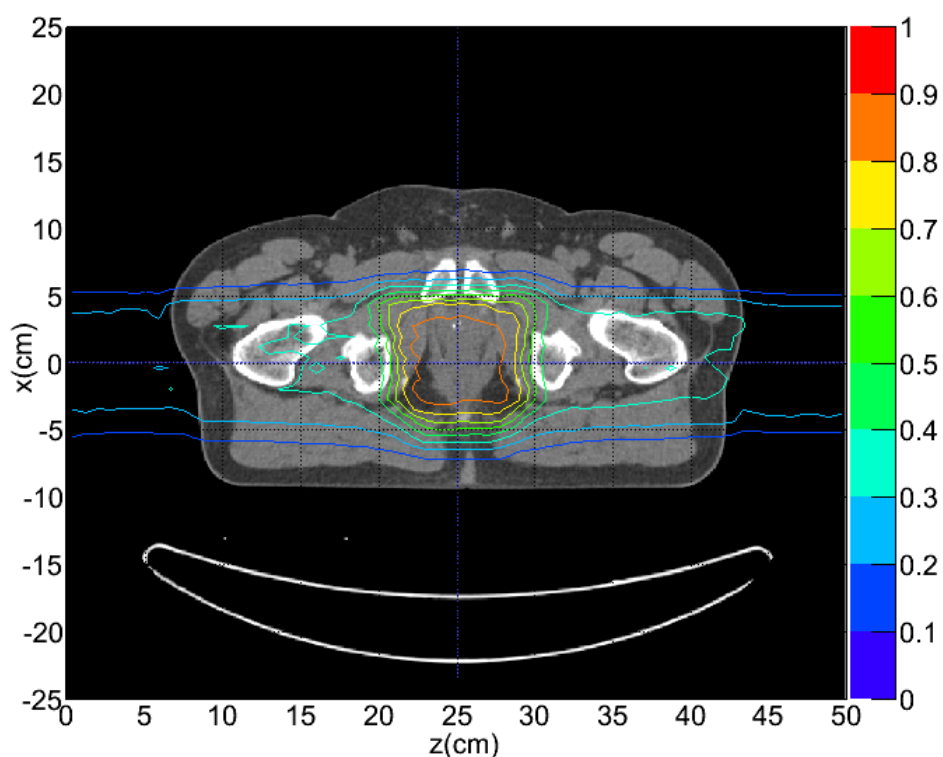


Figure 5-63. Isodose Lines Superimposed on Axial CT Image

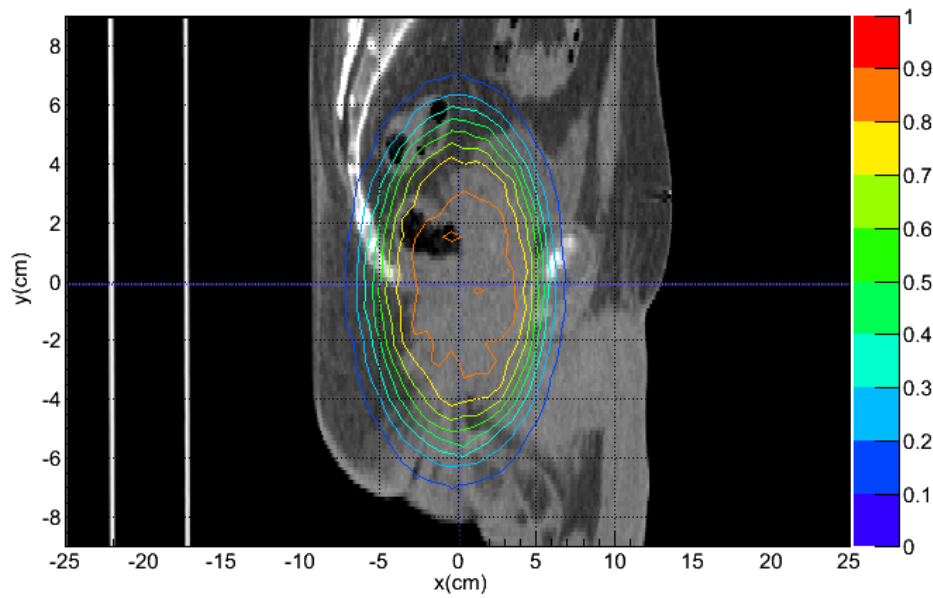


Figure 5-64. Isodose Lines Superimposed on Sagittal CT Image

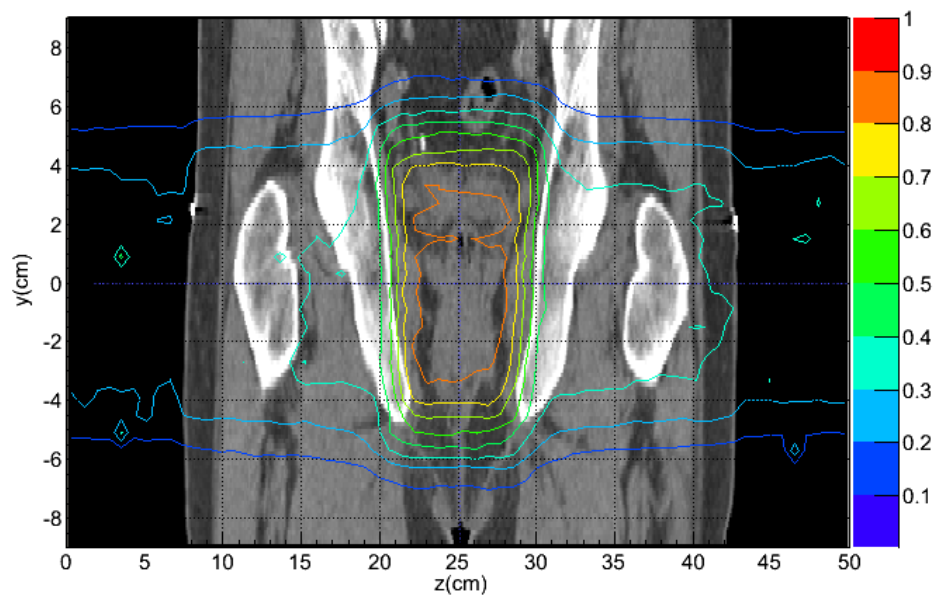


Figure 5-65. Isodose Lines Superimposed on Coronal CT Image

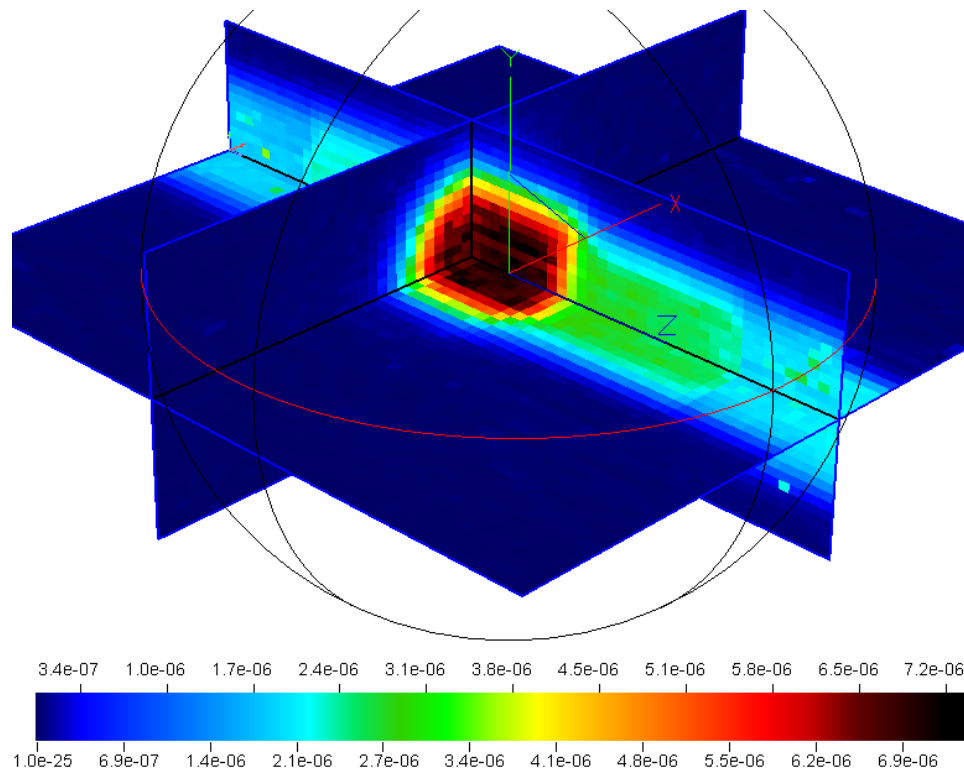


Figure 5-66. 3D Absolute Dose Distribution in Patient Voxel Geometry

6. SUMMARY AND EXTENSION OF CURRENT RESEARCH

6.1 Summary

Proton therapy is a dynamic cancer treatment technique for both dynamic scanning and passive scattering. This research provided a method to perform a dynamic simulation of proton therapy using the Monte Carlo simulation toolkit Geant4. This research provided a Geant4 application template for modeling a passive-scattering treatment nozzle.

This research provided a method to convert the CT images of a patient to a 3D patient voxel geometry for Geant4 Monte Carlo simulation. Finally, the accurate spatial dose distribution in the patient body with prostate cancer was obtained successfully.

This research provided a more flexible and applicable data-storing and data-analysis method using root interface in the Geant4 application. The results from multiple simulations could be stored in one root file and the data in it could be analyzed in the root environment after the Geant4 simulation.

This research also provided a method in obtaining the correct neutron dose contribution in proton therapy. The simulation results showed that the dose contribution from neutrons and neutron secondary particles was small but could not be neglected if considering the biological effects of neutrons.

In this research, some bugs in Geant4 source codes and examples were found, so this research also made a contribution for the development of the Geant4 toolkit.

6.2 Extension of Current Research

Only a passive-scattering nozzle was modeled in the current research. The dynamic scanning technique can be also modeled using Geant4 if the design parameters are available in future.

The speed for visualizing the patient voxel geometry is very slow in Geant4 if the number of voxels is relative large. It is necessary to develop a new method to speed up the visualization of the voxel geometry in Geant4 by allocating the memory properly.

REFERENCES

- Abramoff MD, Magalhaes PJ, Ram SJ. Image Processing with ImageJ. *Biophotonics International*, 11(7):36–42; 2004.
- Agostinelli S, et al. GEANT4—A Simulation Toolkit. *Nucl. Instr. Meth. Phys. Res., A506*[3], 250–303; 2003.
- Archambault L, Beaulieu L, Hubert-Tremblay V, Arce P, Chauvie S and Armando A. *Geant4.9.5/examples/extended/medical/DICOM*. Geant4 collaboration; 2011.
- Attix FH. *Introduction to Radiological Physics and Radiation Dosimetry*. New York: John Wiley and Sons; 2004.
- Bayle P and Levin B. *World Cancer Report 2008*. International Agency for Research on Cancer IARC, Lyon, France, World Health Organization; 2008.
- Berger MJ, Coursey JS, Zucker MA, and Chang J. ESTAR, PSTAR, and ASTAR: Computer Programs for Calculating Stopping-Power and Range Tables for Electrons, Protons, and Helium Ions (version 1.2.3). [Online] Available: <http://physics.nist.gov/Star> [2009, July 1]. Gaithersburg, MD, National Institute of Standards and Technology; 2005.
- Carrier JF, Archambault L, Beaulieu L and Roy R. Validation of GEANT4, an object-oriented Monte Carlo toolkit, for simulations in medical physics. *Med. Phys.* 31(3): 484–492; 2004.
- Chu WT, Ludewigt BA, and Renner TR. Instrumentation for treatment of cancer using proton and light-ion beams. *Rev. Sci. Instrum.* 64 (8); 1993.
- Chu WT. Overview of Light-Ion Beam Therapy. In ICRU-IAEA meeting, Columbus, Ohio. 2006.
- Cirrone G., et al. Hadrontherapy: a Geant4-Based Tool for Proton/Ion-Therapy Studies. *Progress in Nuclear Science and Technology* 2:207–212; 2011.
- Coen JJ and Zietman AL. Proton Radiation for Localized Prostate Cancer. *Nat. Rev. Urol.* 6:324–330; 2009.
- DICOM Introduction and Free Software. Available at <http://www.cabiatl.com/micro/dicom/index.html>. Accessed 5 February 2012.

Dougherty G. Digital Image Processing for Medical Applications. Cambridge UK: Cambridge University Press; 2009.

Geant4 Collaboration. Geant4 User's Guide for Application Developers. Version: geant4 9.5.0. Publication date: 2nd Dec, 2011.

Geant4 Collaboration. Physics Reference Manual. Version: geant4 9.5.0. Publication date: 2nd Dec, 2011.

Gonzalez RC and Woods RE. Digital Image Processing, Third Edition. Upper Saddle River, NJ: Prentice Hall; 2008.

Gottschalk B. NEU User Guide. Cambridge, MA, Harvard University; 2006.

Guan F. Design and Simulation of a Passive-scattering Nozzle in Proton Beam Radiotherapy. M.S. thesis, Texas A&M University, College Station; 2009.

Guan F, Poston J and Braby L. Joint Application of Perl Scripts and MCNPX in Solving the Dynamic-Geometry Related Problems in Proton Beam Radiotherapy. Progress in Nuclear Science and Technology 2:176–180; 2011.

Hara T. F18-Fluorocholine: A New Oncologic PET Tracer. J. Nucl. Med. 42:1815–1817; 2001.

Hsing AW and Chokkalingam AP. Prostate cancer epidemiology. Frontiers in Bioscience 11:1388–1413; 2006.

International Commission on Radiation Units and Measurements ICRU. Photon, Electron, Proton and Neutron Interaction Data for Body Tissues. ICRU REPORT No. 46. 1992.

International Commission on Radiation Units and Measurements ICRU. Prescribing, Recording, and Reporting Proton-beam Therapy. ICRU REPORT No. 78. Journal of the ICRU Volume 7 No 2; 2007.

International Commission on Radiation Units and Measurements ICRU. Fundamental Quantities and Units for Ionizing Radiation. ICRU REPORT No. 85. Journal of the ICRU Volume 11 No 1; 2011.

International Commission on Radiological Protection. Relative Biological Effectiveness, Radiation Weighting and Quality Factor. ICRP Publication 92. Ann. ICRP 33(4); 2003.

InVesalius. Available at <http://svn.softwarepublico.gov.br/trac/invesalius>. Accessed 8 January 2012.

Jarlskog CZ and Paganetti H. Physics Settings for Using the Geant4 Toolkit in Proton Therapy. *IEEE Transaction on Nuclear Science*, Vol. 55, No. 3, 2008

Kalos M, Whitelock P. Monte Carlo Methods. Second Edition. WILEY-VCH Verlag GmbH & Co. KGaA, Weinheim; 2008.

Kirsch DG and Tarbell NJ. Conformal Radiation Therapy for Childhood CNS Tumors. *Oncologist* 9:442–450; 2004.

Lodge M, Pijls-Johannesma M, Stirk L, Munro AJ, De Ruyscher D and Jefferson T. A Systematic Literature Review of the Clinical and Cost-effectiveness of Hadron Therapy in Cancer. *Radiother. Oncol.* 83:110–122; 2007.

Mohan R and Nahum AE. Why Monte Carlo? Proc. Int. Conf. On the use of computing in radiation therapy, Madison Wi: Medical Physics Publishing; 1997.

Noel G, Habrand JL, Helfre S, Mammar H, Kalifa C, Ferrand R, Beaudre A, Gaboriaud G and Mazon JJ. Proton Beam Therapy in The Management of Central Nervous System Tumors in Childhood: the Preliminary Experience of the Centre de Protontherapie d'Orsay. *Med. Pediatr. Oncol.* 40:309–315; 2003.

Olsen DR, Bruland ØS, Frykholm G and Norderhaug IN. Proton therapy – A systematic review of clinical effectiveness. *Radiotherapy and Oncology* 83:123–132; 2007.

Paganetti H. Four-dimensional Monte Carlo Simulation of Time-dependent Geometries. *Phys. Med. Biol.* 49: N75–N81; 2004.

Paganetti H, Jiang H, Lee SY, and Kooy HM. Accurate Monte Carlo Simulations for Nozzle Design, Commissioning and Quality Assurance for a Proton Radiation Therapy Facility. *Med. Phys.* 31(7):2107–2118; 2004.

Paganetti H and Bortfeld T. Proton Beam Radiotherapy—The State of the Art; New Technologies in Radiation Oncology. Heidelberg, Germany, Springer Verlag, ISBN 3-540-00321–5; 2005.

Parker RP, Hobday PA and Cassell KJ. The Direct Use of CT Numbers in Radiotherapy Dosage Calculations for Inhomogeneous Media. *Phys. Med. Biol.* 24(4):802-809; 1979.

Roivainen A, Forsback S, Gronroos T, Lehikoinen P, Kahkonen M, Sutinen E and Minn H. Blood Metabolism of [methyl-C11] Choline; Implications for in vivo Imaging with Positron Emission Tomography; *Eur. J. Nucl. Med.* 27:25-32; 2000.

Schoder H and Larson SM. Positron Emission Tomography for Prostate, Bladder, and Renal Cancer. *Semin. Nucl. Med.* 34:274–292; 2004.

Shukla MK and Leszczynski J, Editors. *Radiation Induced Molecular Phenomena in Nucleic Acids*. Jackson, MS, Springer Science+Business Media B.V., ISBN 978-1-4020-8183-5; 2008.

The ROOT team. *The ROOT Users Guide 5.26*. 2009.

Theis C, Buchegger KH, Brugger M, Forkel-Wirth D and Roesler S, Vincke H. Interactive Three Dimensional Visualization and Creation of Geometries for Monte Carlo Calculations. *Nuclear Instruments and Methods in Physics Research A(562)*:827–829; 2006.

Varian Medical Systems Newsroom. Available at <http://varian.mediaroom.com/index.php?s=13&cat=22&mode=gallery>. Accessed 5 February 2012.

Weber DC. Proton Beam Radiation therapy—From Physics to Clinical Indications. *European Oncological Disease* 2006. Issue II: 93–97; 2006.

Wilson R. Radiological Use of Fast Protons. *Radiology* 47:487–491; 1946.

Wouters BG, Lam GKY, Oelfke U, Gardey K, Durand RE and Skarsgard LD. Measurements of Relative Biological Effectiveness of the 70 MeV Proton Beam at TRIUMF Using Chinese Hamster V79 Cells and the High-Precision Cell Sorter Assay. *Radiation Research* 146:159–170; 1996.

Yushkevich PA, Piven J, Hazlett HC, Smith RG, Ho S, Gee JC, and Gerig G. User-guided 3D Active Contour Segmentation of Anatomical Structures: Significantly Improved Efficiency and Reliability. *Neuroimage*. 31(3):1116–1128; 2006.

Zhang G's Blog. Available at <http://cnsconfig.blog.163.com/blog/static/64045702009823190283>. Accessed 12 July 2010.

Zheng Y, Fontenot J, Taddei P, Mirkovic D and Newhauser W. Monte Carlo Simulations of Neutron Spectral Fluence, Radiation Weighting Factor and Ambient Dose Equivalent for a Passively Scattered Proton Therapy Unit. *Phys. Med. Biol.* 53:187–201; 2008.

Zhou J. Dosimetry of ⁹⁰Y Liquid Brachytherapy in a Dog with Osteosarcoma Using PET/CT. M.S. thesis, Texas A&M University, College Station; 2011.

APPENDIX A

MACRO FILES FOR A GEANT4 APPLICATION

A.1 runNozzleRotation.mac File for Geometry Case No. 6

```

#2012-02-14
#nozzle on the left first for 1440 run
#then nozzle rotates around water center y-axis 180 deg
#use another gps source for 1440 run
#/control/verbose 2
#/run/verbose 2

/geometry/setCaseNb 6
/geometry/buildPatientPhantom true

/modulator/NbOfSections 1
/modulator/mirrorHalfSection true

/compensator/tumorRadius 4 cm
/compensator/shifterThickness 4.6875
#5 cm 5.46875 cm
/wedge/thickness 5 cm

/run/initialize

/control/execute macro/source/2_gauss.mac

/control/alias initialValue 1
/control/alias finalValue 1440
/control/alias stepSize 1
#phi will be the variable name for below loop process
#its value increases from {initialValue} to {finalValue} in angle.loop
/control/loop macro/run/runModulatorAngle.loop phi {initialValue} {finalValue}
{stepSize}

#rotate the nozzle around y-axis
/nozzle/angle 180 deg
/wedge/deltaAngle 180 deg
#clear the old source
/gps/source/clear
/control/execute macro/source/3_gauss_rotate.mac

```

```

/control/alias initialValue 1
/control/alias finalValue 1440
/control/alias stepSize 1
#phi will be the variable name for below loop process
#its value increases from {initialValue} to {finalValue} in angle.loop
/control/loop macro/run/runModulatorAngle.loop phi {initialValue} {finalValue}
{stepSize}

```

A.2 2_gauss.mac File for Defining the Primary Particle Source

```

/control/verbose 2
/run/verbose 2

# Specify particle source
/gps/particle proton

#Beam
/gps/pos/type Beam
/gps/pos/shape Circle
#for geometry case 1, ssd = 10 cm
#/gps/pos/centre 0. 0. -10. cm
/gps/pos/centre 0. 0. -300 cm
/gps/pos/radius 0.0 cm
#beam1d sigma conversion is not correct
#we should use 2d instead
#/gps/pos/sigma_r 0.65 cm
/gps/pos/sigma_x 0.65 cm
/gps/pos/sigma_y 0.65 cm

#the default direction of beam is -z' axis
#by rotation matrices, beam can fly along z-axis
/gps/ang/rot1 0 1 0
/gps/ang/rot2 1 0 0
/gps/ang/type beam1d
#0.0032 rad
#1 rad = 57.3 deg
/gps/ang/sigma_r 0.183 deg

#Gaussian energy
#/gps/ene/type Mono
/gps/ene/type Gauss
/gps/ene/mono 250 MeV
/gps/ene/sigma 2.5 MeV

```

A.3 runModulatorAngle.loop File for Each Run with a Fixed Modulator Angle

```
#2012-01-15  
#set the delta rotation angle of wheel around z-axis  
#phi>0 means clockwise  
/modulator/deltaAngle 0.25 deg  
/run/beamOn 3000
```

APPENDIX B

Source Codes to Convert CT Images to Material Density and ID Matrices

```

%ProcessMultipleDicom.m
%Author: Fada Guan
%Creation Date: 2012-01-20
%read in a series of dicom files
%1) obtain CT number distribution map for each CT slice
%2) convert the CT number distribution map into material density
%distributionmap for each CT slice
%3) convert the material density distribution map into material ID
%distribution map for each CT slice
%4) rebin the original material density table, and create a new table
%containing <new material density, new material ID> pairs
%5) transfer the original material density into a new material density for
%each pixel, and create new material density distribution map for each
%slice
%6) transfer the original materialID into a new materialID for each pixel,
%and create new material ID distribution map for each slice
%7) compress the density map and create new compressed material ID map
%if compression factor k is used, the compressed map of each slice will
%have size m/k * n/k, the density in a new large voxel will be equal to average
%density of k*k voxels in original density map. new compressed materialID
%map will also be created

%1) clear old variables first
clear;% clear x means only clear variable x

%2) set compression factor k for each slice to reduce the number of pixels
k=8;
kz = 4;%compression factor in z order of slice,%2012-02-23
%3) process a series of CT slices and create useful maps
zIndexMin=621;%the minimum serial number of dicom files
zDelta=1; %serial number interval of two consecutive dicom files
zIndexMax=660;%the maximum serial number of dicom files

if ( mod(zIndexMax-zIndexMin+zDelta,zDelta*kz)~=0 )%2012-02-23
    fprintf('z indices are not in a regular order.\n');
    return;
end

```

```

for zIndex=zIndexMin:zDelta:zIndexMax
%3.1) read in a dicom format image, obtain CTNbMap of this slice
  dirName_dcm=sprintf('prostate');
  if ~exist(dirName_dcm,'dir')
    fprintf('dir: %s does not exist\n',dirName_dcm);
    return;
  end

  dcmFileName=sprintf('%s\\IM-0001-0%d.dcm',dirName_dcm,zIndex);%IM-0001-0
is added only for prostate example, fada,2012-02-23
  CTNbMap=ProcessOneDicom(dcmFileName, zIndex, k);%without ;, the content in
CTNbMap will show in screen

%3.2) obtain four maps converted from the CT number map of this slice

[DensityMap,MaterialIDMap,NewDensityMap,NewMaterialIDMap]=CTNb2DensityAn
dMaterialID(CTNbMap, zIndex);

end

for zIndexBegin = zIndexMin: zDelta*kz: zIndexMax-zDelta*(kz-1)
  DensityMap = MergeDensityMapInZ (zIndexBegin,zDelta,kz);

[CompressedDensityMap,CompressedMaterialIDMap,NewCompressedDensityMap,Ne
wCompressedMaterialIDMap]=CreateCompressedMap(DensityMap, k, zIndexBegin);
end
%4) merge the information for all compressed slices
MergeCompressedInfo(zIndexMin,zDelta*kz,zIndexMax-zDelta*(kz-1) );

```

APPENDIX C

Geometry Parameter of Double-Scattering System for Geometry Case No. 6

Table C-1. Parameters of S1 from NEU for Case No. 6

Step No.	Weight	Thickness (cm)	
		Lead	Lexan
1	0.4603	0.6451	0.0001
2	0.1571	0.6316	0.9198
3	0.1106	0.6168	1.8464
4	0.0843	0.6012	2.7768
5	0.0705	0.5850	3.7106
6	0.0554	0.5681	4.6475
7	0.0618	0.5507	5.5877

Table C-2. Parameters of S2 from NEU for Case No. 6

Radius (cm)	Thickness (cm)	
	Lexan	Lead
0.0000	0.0999	0.6656
0.4442	0.3338	0.6194
0.8885	0.9420	0.4990
1.3327	1.7482	0.3394
1.7769	2.5463	0.1812
2.2212	3.1254	0.0664
2.6654	3.4338	0.0052
3.1096	3.4600	0.0000
3.5539	3.4600	0.0000
3.9981	3.4600	0.0000

APPENDIX D

Main Function in the Geant4 Application

```

//promise008.cc
//Author: Fada Guan
#include "PromiseDetectorConstruction.hh"
#include "PromisePhysicsList.hh"
#include "PromisePrimaryGeneratorAction.hh"
#include "PromiseRun.hh"
#include "PromiseRunAction.hh"
#include "PromiseEventAction.hh"

#include "QGSP_BERT.hh"//prepackaged physicsList

#include "G4RunManager.hh"
#include "G4EventManager.hh"
#include "G4UImanager.hh"
#include "Randomize.hh"
#include "time.h"//fada 2011-12-01

#ifdef G4UI_USE
#include "G4UIExecutive.hh"
#endif

#ifdef G4VIS_USE
#include "G4VisExecutive.hh"
#endif

#ifdef G4ANALYSIS_USE_ROOT
#include "PromiseRootManager.hh"
#include "TROOT.h"
#include "TApplication.h"

#include "G4SDManager.hh"

#include "G4MultiFunctionalDetector.hh"
#include "PromisePSEnergyDeposit.hh"
#include "PromisePSPlaneScorer.hh"
#endif
//add G4StepLimiter process for proton,fada,2011-09-03

```



```

#include "G4Proton.hh"
#include "G4ProcessManager.hh"
#include "G4StepLimiter.hh"
#include "PromiseProtonStepLimiter.hh"
//fada,2011-12-20
#include "PromiseTrackingAction.hh"

void SetJobRandomEngine();
#ifdef G4ANALYSIS_USE_ROOT
void WriteDetectionRootFiles(PromiseDetectorConstruction* detectorConstruction);
void WriteGPSRootFile();
#endif

int main(int argc,char** argv) {
//2011-08-08,fada, directed by Rene Brun
#ifdef G4ANALYSIS_USE_ROOT
  TApplication myApp("myapp", &argc, argv);
//without this line, TCanvas cannot pop up
#endif

//set job random engine, user-defined function below,2012-01-15
  SetJobRandomEngine();

// Run manager
  G4RunManager * runManager = new G4RunManager;

// Mandatory initialization classes
  PromiseDetectorConstruction* detectorConstruction = new
PromiseDetectorConstruction();
  runManager->SetUserInitialization(detectorConstruction);
// runManager->SetUserInitialization(new PromisePhysicsList); //for normal energy

//add a steplimiter for proton and register it to QGSP_BERT
  G4VModularPhysicsList* qgsp_bert_fada = new QGSP_BERT(1);//set verbose
level=1
  qgsp_bert_fada->RegisterPhysics(new PromiseProtonStepLimiter(2));//set verbose
level=2 to see message
  runManager->SetUserInitialization(qgsp_bert_fada); //EMstandard_option0, hadronic
physics included

// User action classes
  runManager->SetUserAction(new PromisePrimaryGeneratorAction());
  runManager->SetUserAction(new PromiseEventAction());//2012-01-08

```

```

// runManager->SetUserAction(new PromiseRunAction());
//fada,2011-12-20,trackingAction
runManager->SetUserAction(new PromiseTrackingAction());

// Initialize G4 kernel
// runManager->Initialize();
// runManager->BeamOn(100);

//////////
#ifdef G4VIS_USE
G4VisManager* visManager = new G4VisExecutive;
visManager->Initialize();
#endif

// Get the pointer to the User Interface manager
//
G4UImanager * UImanager = G4UImanager::GetUIpointer();

if(argc!=1) // batch mode
{
G4String command = "/control/execute ";
G4String fileName = argv[1];
UImanager->ApplyCommand(command+fileName);
}
else // interactive mode : define UI session
{
#ifdef G4UI_USE
G4UIExecutive * UIExecutive = new G4UIExecutive(argc,argv);
/*
#ifdef G4VIS_USE
UImanager->ApplyCommand("/control/execute vis.mac");
#endif
*/
if(UIExecutive->IsGUI())
UImanager->ApplyCommand("/control/execute macro/gui.mac");//2011-08-31

UIExecutive->SessionStart();

delete UIExecutive;
#endif
}

//////////
// Job termination

```

```

#ifdef G4ANALYSIS_USE_ROOT
  if(!runManager->GetUserRunAction())//do not repeat writing root files
    WriteDetectionRootFiles(detectorConstruction);

  G4EventManager* eventManager = G4EventManager::GetEventManager();
  if(eventManager->GetUserEventAction())
    WriteGPSRootFile();
#endif

#ifdef G4VIS_USE
  delete visManager;
#endif

  delete runManager;

  return 0;
}

void SetJobRandomEngine()
{
  //choose the Random engine
  CLHEP::HepRandom::setTheEngine(new CLHEP::RanecuEngine());//fada,2011-09-03
  //set random seed with system time
  G4long seed = time(NULL);
  CLHEP::HepRandom::setTheSeed(seed);
  //fada 2011-12-01
  time_t rawtime;
  struct tm * timeinfo;

  time ( &rawtime );
  timeinfo = localtime ( &rawtime );
  printf ( "Current local time and date: %s", asctime (timeinfo) );
  //output local time
}
#ifdef G4ANALYSIS_USE_ROOT
void WriteDetectionRootFiles(PromiseDetectorConstruction* detectorConstruction)
{
  // Get the sensitive detector manager
  G4SDManager* manager = G4SDManager::GetSDMpointer();

  std::vector<G4String> aDetectorNameVector = detectorConstruction-
  >GetDetectorNameVector();
  size_t NbOfDetectors = aDetectorNameVector.size();

```

```

G4cout<<"number of sensitive detectors: "<<NbOfDetectors<<G4endl;

G4String detectorName;
for(size_t i=0; i!=NbOfDetectors; ++i)
{
    detectorName = aDetectorNameVector[i];
    // Get the sensitive detector
    G4MultiFunctionalDetector* detector =
        dynamic_cast<G4MultiFunctionalDetector*>(manager-
>FindSensitiveDetector(detectorName));

    G4int NbOfPrimitives = detector->GetNumberOfPrimitives();

    G4cout<<"number of primitives for detector ["<<detectorName<<"]:
"<<NbOfPrimitives<<G4endl;
    for(int j= 0; j!= NbOfPrimitives; j++)
    {
        if(detectorName.find("BoxDetector") != G4String::npos)
        {
            PromisePSEnergyDeposit* prim =
                dynamic_cast<PromisePSEnergyDeposit*>(detector->GetPrimitive(j));

            TFile* aRootFile = prim->GetFile();
            aRootFile->Write();
        }
        else if(detectorName.find("PlateDetector") != G4String::npos)
        {
            PromisePSPlaneScorer* prim =
                dynamic_cast<PromisePSPlaneScorer*>(detector->GetPrimitive(j));
            TFile* aRootFile = prim->GetFile();
            aRootFile->Write();
        }
        else if(detectorName.find("VoxelDetector") != G4String::npos)//2012-02-15
        {
            PromisePSEnergyDeposit* prim =
                dynamic_cast<PromisePSEnergyDeposit*>(detector->GetPrimitive(j));

            TFile* aRootFile = prim->GetFile();
            aRootFile->Write();
        }
        else
        {
            G4cout<<"cannot find interested detectors"<<G4endl;

```

```
        return;
    }
}
G4cout<<"detection results for detector ["<<detectorName<<"] have been stored in
root files" <<G4endl;
// G4cout <<"detection results have been stored in root files" <<G4endl;
}
}

void WriteGPSRootFile()
{
    TFile* aGPSRootFile = PromiseEventAction::GetFile();
    aGPSRootFile->Write();
    G4cout <<"primary particles' information have been stored in a root file" <<G4endl;
}

#endif
```

VITA

Name: Fada Guan

Address: 3133 TAMU, Department of Nuclear Engineering,
College Station, TX, USA, 77843-3133

Email address: guanfada@tamu.edu, guanfada@gmail.com

Education: B.E., Nuclear Engineering and Nuclear Technology,
Tsinghua University, China, 2005

M.S., Health Physics, Texas A&M University, USA, 2009

Ph.D., Nuclear Engineering, Texas A&M University, USA, 2012